



HAL
open science

Behaviour of a bubble in a horizontal high-speed solid-body rotating flow

Majid Rodgar

► **To cite this version:**

Majid Rodgar. Behaviour of a bubble in a horizontal high-speed solid-body rotating flow. Other. Université de Lyon, 2022. English. NNT : 2022LYSEC025 . tel-03768940

HAL Id: tel-03768940

<https://theses.hal.science/tel-03768940>

Submitted on 5 Sep 2022

HAL is a multi-disciplinary open access archive for the deposit and dissemination of scientific research documents, whether they are published or not. The documents may come from teaching and research institutions in France or abroad, or from public or private research centers.

L'archive ouverte pluridisciplinaire **HAL**, est destinée au dépôt et à la diffusion de documents scientifiques de niveau recherche, publiés ou non, émanant des établissements d'enseignement et de recherche français ou étrangers, des laboratoires publics ou privés.



ÉCOLE
CENTRALE LYON

THÈSE de DOCTORAT DE L'UNIVERSITÉ DE LYON

Opérée au sein de :
l'École Centrale de Lyon

École Doctorale 162: Mécanique, Énergétique, Génie Civil et Acoustique

Spécialité de doctorat : Mécanique des fluides et Énergétique

N° d'ordre NNT : 2022LYSEC025

Soutenance publique soutenue le mercredi 1 juin 2022, par :

Majid RODGAR

Behaviour of a bubble in a horizontal high-speed solid-body rotating flow

Devant le jury composé de :

Christophe CORRE

Professeur des Universités, Ecole Centrale de Lyon, LMFA

Véronique ROIG

Professeur des Universités, INP Toulouse, IMFT

Adrien TOUTANT

Maître de conférences, Université de Perpignan, PROMES

Anne-Laure BIANCE

Directrice de Recherche CNRS, ILM, Lyon

Jean-Philippe MATAS

Professeur des Universités, Université Claude Bernard Lyon 1, LMFA

Jean-Louis MARIÉ

Chargé de recherche CNRS, LMFA

Hélène SCOLAN

Maître de conférences, Université Claude Bernard Lyon 1, LMFA

Delphine DOPPLER

Maître de conférences, Université Claude Bernard Lyon 1, LMFA

Examineur

Rapporteur

Rapporteur

Présidente

Directeur de Thèse

Invité

Invitée

Invitée

Acknowledgements

Throughout the writing of this dissertation I have received a great deal of support and assistance.

I would first like to thank my supervisor, Professor Jean-Philippe MATAS, whose expertise was invaluable in formulating the research questions and methodology. Your insightful feedback pushed me to sharpen my thinking and brought my work to a higher level.

I would like to offer special thanks to my co-supervisor Professor Peter SPELT, who, although no longer with us. May he rest in peace.

I would like to acknowledge Dr. Jean-Louis Marié for his invaluable assistance during my PhD. He shared all of his knowledge and experience in this field with me, and helped me understand our objectives more clearly.

I would also like to thank my tutors, Dr. Hélène SCOLAN and Dr. Delphine DOPPLER, for their valuable guidance throughout my studies.

In addition, I would like to thank my parents for their wise counsel and sympathetic ear. You are always there for me. Finally, I could not have completed this dissertation without the support of my friends at the laboratory of LMFA, who provided stimulating discussions as well as happy distractions to rest my mind outside of my research.

Résumé

Mots clés : dynamique de la bulle, brisure, déformation de la bulle, écoulement en rotation, coefficients de portance et de traînée, tensioactifs solubles.

Ce travail a pour but de décrire le comportement d'une bulle placée dans un écoulement de rotation solide d'axe horizontal. Cette situation est intéressante car elle peut nous aider à comprendre comment les bulles se comportent lorsqu'elles rencontrent des régions d'écoulement avec une vorticité localement élevée. Ces régions de tourbillon élevé peuvent être trouvées dans une large gamme de situations d'écoulement.

Afin d'extraire des informations sur la dynamique des bulles dans un écoulement de rotation solide, nous avons utilisé un dispositif expérimental constitué d'une cuve cylindrique en plexiglas tournant autour de son axe horizontal. Pour cette expérience, la plage de vitesse de rotation étudiée est [600-900] rpm, c'est-à-dire de 63 rad s^{-1} à 94 rad s^{-1} . Deux caméras ont été utilisées pour déterminer la forme, et le mouvement de la bulle à l'intérieur du réservoir.

Lorsque la vitesse de rotation du réservoir augmente, la bulle se rapproche de l'axe de la cellule et s'étire le long de l'axe horizontal. Nous étudions d'abord cet étirement de la bulle en fonction de la taille de la bulle et de la vitesse de rotation de la cellule. Nous montrons que le rapport d'aspect de la bulle peut être prédit en fonction du nombre de Weber de la bulle par le modèle de Rosenthal 1962, pourvu qu'une correction due au décentrage de la bulle soit prise en compte. Cette correction tient compte de la plus grande différence de pression entre la périphérie et l'axe de la bulle, lorsque la bulle s'écarte de l'axe en raison de sa flottabilité. Ensuite, nous avons observé que la bulle peut s'étirer jusqu'à des rapports d'aspect de deux, et même se briser à certaines vitesses de rotation pour les grandes tailles de bulles. Nous montrons que cette rupture se produit par un mécanisme de résonance lorsque la fréquence de rotation du réservoir devient

de l'ordre de la fréquence propre de la bulle.

Nous déduisons ensuite les coefficients de traînée et de portance à partir de la position moyenne de la bulle. Pour les grosses bulles chevauchant l'axe de rotation, nous montrons que le coefficient de traînée C_D dépend uniquement du nombre de Rossby Ro , avec $C_D \sim 1.5/Ro$. Dans la même limite, nous avons proposé une estimation du coefficient de portance pour le faible nombre de Rossby Ro . En effet, nous montrons que le coefficient de portance C_L est contrôlé par le nombre de Reynolds de cisaillement $Re_{shear} = Re/Ro$ à l'échelle de la bulle.

Finalement, afin de modifier la tension superficielle du liquide et d'explorer les effets des tensioactifs sur la bulle, nous avons introduit un composé chimique tensioactif dans le liquide (*TTAB*). Nous avons examiné deux solutions de tensioactifs alternatives : une de concentration inférieure à la concentration micellaire critique CMC (0.33 CMC) et une supérieure à la CMC (2 CMC), dans laquelle l'interface de la bulle est a priori saturée de tensioactifs. Nous avons effectué la même analyse de déformation et de force qui a été effectuée avec de l'eau déminéralisée avec les solutions de tensioactifs. Les résultats montrent que comme attendu la déformation de la bulle est plus importante dans les deux solutions de tensioactifs que dans l'eau, et peut toujours être modélisée par le modèle de Rosenthal 1962 dans le cas de la solution 2 CMC. Cependant, dans le cas de la solution 0.33 CMC la bulle se comporte comme si elle voyait une tension superficielle effective égale à celle de la solution à la CMC. Concernant la brisure, nous observons que comme pour l'eau la brisure se produit lorsque la fréquence de rotation du réservoir est de l'ordre de la fréquence propre de la bulle. Enfin, les coefficients de portance et de traînée ont été mesurés en présence de surfactant : les valeurs obtenues sont similaires à celles obtenues avec l'eau déminéralisée.

Summary

Keywords: bubble dynamics, break-up, deformation of the bubble, rotating flow, lift and drag coefficients, surfactant effects.

This research study focuses on bubbles released inside a horizontal high-speed solid-body rotating flow. This flow situation is interesting because it can help us to understand how bubbles behave when they meet flow regions with locally high vorticity. These high vorticity regions can be found in a variety of flow situations.

In order to extract information about bubble dynamics in solid-body rotating flow, we have used an experimental apparatus containing a cylindrical Plexiglas tank of diameter 11 cm and length 10 cm which is rotated around its horizontal axis z . The bubble can be injected into the cell at the rest. For this experiment, the range of rotational velocity investigated is [600-900] rpm, i.e. from 63 rad s^{-1} to 94 rad s^{-1} . Two high-speed cameras were used to determine the physical features of the bubble motion inside the tank.

When the rotational velocity of the tank increases, the bubble moves close to the axis of the cell, and stretches along the horizontal axis. We first study this stretching of the bubble as a function of bubble size and of the rotation rate of the cell. We show that the bubble aspect ratio can be predicted as a function of the bubble Weber number by the model of Rosenthal 1962 provided an appropriate correction due to the impact of buoyancy is included. This correction accounts for the larger pressure difference between periphery and axis of the bubble, when the bubble is displaced away from the axis because of buoyancy. Then we discovered that the bubble can experience the large aspect ratio up to 2 and breaks up at certain rotational speeds for large bubble sizes. We show this break-up occurs through a resonance mechanism when the rotational velocity of the tank becomes of the order of the eigenfrequency of the bubble.

We next deduce the drag and lift coefficients from the mean bubble position.

For large bubbles straddling the axis of rotation we show that the drag coefficient C_D is solely dependent on the Rossby number Ro , with $C_D \sim 1.5/Ro$. In the same limit of large bubbles, we have proposed an estimate of the lift coefficient for the low Rossby number Ro . Indeed, we show that the lift coefficient C_L is controlled by the shear Reynolds number $Re_{shear} = Re/Ro$ at the scale of the bubble.

Eventually, in order to change surface tension of the bulk liquid and explore the effects of surfactants on the bubble we have used a chemical compounds called TetradecylTrimethylAmmoniumBromide (TTAB) in the liquid. We have studied two alternative surfactant solutions: one that is lower than the CMC (0.33 CMC) and one that is higher than the CMC (2 CMC), in which the bubble interface is expected to be entirely saturated by surfactants. We have carried out the same deformation and force analysis that were carried out with demineralised water with the surfactant solutions. The results reveal that as expected the deformation of the bubble is larger in both surfactant solutions than in water, and is still modelled by the model of Rosenthal 1962 in the case of the 2 CMC solution. In the case of the 0.33 CMC solution, the bubble behaves as if it was seeing an effective surface tension equal to that in the CMC solution. Regarding break-up, we observe that as for water, break-up occurs when the tank frequency is of the order of the bubble eigenfrequency. Furthermore, the lift and drag coefficients were measured in the presence of surfactant, and the values measured were similar to those obtained with demineralised water.

Contents

Acknowledgements	iii
Résumé	v
Summary	vii
Contents	ix
1 Introduction	1
1.1 General context	1
1.1.1 Bubble Dynamics	1
1.1.2 Effect of Surfactant on the Bubble Dynamics	4
1.2 Context of present study	5
1.3 Objectives	7
2 Experiments	9
2.1 Experimental Set-up	9
2.1.1 Flow characteristics	10
2.1.2 Bubble injection, surface tension measurements and other physical parameters	13
2.2 Image Processing	14
2.2.1 Particle detection	15
2.2.2 Camera synchronization and Calibration	17
2.2.3 Volume measurement and experimental data	27
2.3 Bubble equilibrium position	35
2.4 Dimensionless Parameters	37
3 Deformation of the bubble	41
3.1 Bubble Position	41
3.2 Bubble deformation	44
3.2.1 Experimental results	44
3.2.2 Discussion of ellipsoidal shape assumption	45

3.2.3	Model of Rosenthal 1962	47
3.3	Break-up	54
4	Forces acting on the bubble	63
4.1	Modeling of the forces	64
4.2	Drag coefficient	67
4.3	Lift	71
4.3.1	Variations of the added mass coefficient (C_A)	74
4.3.2	Measuring the value of the lift coefficient (C_L)	80
4.3.3	Spinning	83
5	Effect of surfactants on bubble deformation and dynamics	87
5.1	Solution with lower and higher concentration of TTAB in comparison with CMC	88
5.2	Bubble deformation in presence of surfactants	92
5.2.1	Position of the bubble	92
5.2.2	Bubble interface configuration	95
5.3	Forces	100
5.3.1	Drag	100
5.3.2	Lift	107
5.4	Break-up	111
6	Conclusion and perspectives	121
6.1	Conclusion	121
6.2	Perspectives	124
6.2.1	Investigating the behavior of bubbles over a wider range of rotation speeds	125
6.2.2	Using another type of surfactant	125
6.2.3	Numerical simulation	125
6.2.4	Investigating the bubble dynamics in presence of other surrounding bubbles	126
	Bibliography	127
	List of Publications	131

1.1 General context

1.1.1 Bubble Dynamics

Understanding the behavior of gas bubbles in liquid flows is relevant for many industrial and environmental processes, and has been studied for a long time. Bubbles exhibit various dynamical behaviors which have been investigated by experts in physics, fluid dynamics and multi phase flows during past decades. For instance, in environmental phenomena bubbles are present in heat and mass transfer in lakes and rivers, aerosol transfer from the sea, oxygen dissolution in the sea due to rain and electrification of atmosphere by the sea bubbles, river aeration, etc. Moreover, bubbles are of great importance in a wide range of industrial applications such as chemical reactors, thermohydraulics, modeling and prediction of their behavior around the propellers of ships and submerged turbines, etc. Therefore, initial modeling and prediction of bubble dynamics requires deep knowledge of bubble physics. Among these topics it is essential to investigate the dynamics of rising bubbles. Clift et al. 1978 carried out theoretical studies around rising bubble shape in unlimited surrounding flow. They discovered that when the ratio of a dispersed rising bubble to the surrounding flow is low, the bubble tends to form ellipsoidal and spherical caps. Wang et al. 2016, performed an experimental and numerical study on the dynamics of a soaring bubble with high Reynolds number in a vertical Hele-shaw. The bubbles have been confined between cell-walls, and forming various shape from spherical, ellipsoidal and complex interface configurations in function of space between the cell-wall. Their studies showed that the bubble shape can be altered depending on the gap between the cell walls, from oblate ellipsoid and spherical to more complex shapes. Furthermore, a dependency of the drag coefficient on the gap thickness of the cell has been derived. Chen et al. 1999 accomplished a numerical study with Volume-of-fluid method to recognize gas bubble deformation, rising and break-up in closed vertical cylinder with a gravitational field. They discovered that depending on the Reynolds and Bond numbers, bubbles can evolve

on a variety of shapes, including toroidal, spherical, and elliptical. The density ratio causes certain bubble configurations, which affect the rising velocity of the bubble.

The other fundamental question is to understand the spatial heterogeneity in the distribution of bubbles. By the way of example, Serizawa et al. 1975 have performed experimentally an appealing work on bubbly flow ascending in a vertical pipe to characterize interactions between bubbles and the upward flow. The experimental study found that the turbulence intensity decreased first with growing gas flow rate for constant water velocity, then increased again with subsequent gas flow rate increases. Bentley and Leal 1986 have done an experimental study investigating the drop deformation and rupturing in two-dimensional linear flows. They proved that drop shape depends on viscosity ratio of surrounding flow and droplet, along with characteristics of the continuous flow around the droplet.

Takemura et al. 2002 experimentally studied forces and the shape of a rising bubble near a vertical wall in a viscous fluid. They have been able to determine the drag and lift force components along with bubble interface configuration using a portable optical instrument. They have shown that the wall inevitably causes a drop of rising velocity inducing a repulsive lift force upon the migrating bubble. Legendre and Magnaudet 1998 have examined other limits with a numerical study, that of linear viscous shear flow, and found the lift force upon the bubble. There have also been some other interesting studies on both aspects of deformation and forces. Perrard et al. 2021 performed a direct numerical simulation for a dispersed spherical bubble in a homogeneous and isotropic turbulent flow. The results have shown that there is a coupling between deduced harmonic equation of different modes of bubble configuration and turbulent velocity variations.

Bubble in a rotating flow

In the case of a bubble in a rotating flow, Bush et al. 1995 presented an analytical anticipation of the shape along with rising velocity of a drop translating in a vertical axisymmetric rigid body rotating fluid with a low viscosity. They displayed that as the bubble is in an equilibrium position between centrifugal and interfacial forces, it begins to deform into a prolate ellipsoid. At the end, a set of complementary experiments were performed and experimental results have

been qualitatively compatible with a proposed analytical solution. In the similar surrounding flow conditions in the vicinity of droplets (rotating flow around the vertical axis under an accelerating field), numerical study of Maneshian et al. 2018 proved that depending on the Morton number of the bubble along with various value of a dimensionless number which is ratio of centrifugal and buoyancy force, the bubble is subjected to a variety of motions, including spinning, rotation, and translation, as well as various interface shapes.

Auton 1987 analytically discussed the forces (focused more on the lift) acting on the small spherical bubbles in a rotational flow which shall be quite similar to the case of shear flow (Saffman 1965 proposed an analytical solution for lift upon the sphere in a viscous shear flow). Kariyasaki 1987 conducted research on bubbles in a vertical channel with two walls. They calculated the lift force of a deformed bubble and compared it to that of a solid sphere in a uniform shear flow using theoretical contributions. The results confirmed that the lift upon the deformed bubble is opposite to that of a non-deformed one. In the same situation of vertical shear flow, the numerical analysis of Ervin and Tryggvason 1997 is another fascinating study of the forces acting on the bubble. The effects and variations of the forces on the deformed air bubble were discovered by numerical simulation (finite difference method of full Navier-Stokes equations).

Leslie 1985 captured the interface reaction of a rotating bubble inside a closed container boundaries in its equilibrium position in conditions of low gravity. They showed the interface shape depends on size, contact angle with the container, and the ratio of the centrifugal force to the surface tension in a way that when this force ratio rises, the bubble tends to be cylindrical and initiate adequate pressure drop for hydro-static contribution.

All these aspects of bubble behaviour influence the transfers (momentum, heat and mass) at the gas-liquid interface (Risso 2000) and in doing so, are worthwhile to be investigated. One important factor for bubbles is the degree of "cleanliness" of the interface. Indeed, besides the heat and mass transfers with the bulk, the presence of surfactant or impurities at the surface can modify the forces acting on the bubble in a spectacular way Clift et al. 1978, Takagi and Matsumoto 2011. It can for instance increase the drag force, hence reducing the bubble rising velocity, and modify the lift force that bubbles experience in shear flows, which influences their lateral motion in such flows.

1.1.2 Effect of Surfactant on the Bubble Dynamics

An essential factor for bubble dynamics is the degree of cleanliness of the interface. In other words, impurities mixing in the carrier flow. In bubbly flows, a small quantity of surfactant can provoke extreme variations in the flow structures through the multi-scale effects of the flow. For instance, surfactant effects can be observed for the rising bubbles when a bubble in an aqueous surfactant solution rises slower than in a clean purified water. This phenomena occurs due to nonuniform distribution of surfactant on the bubble surface. This non-uniform concentration distribution can also influence bubble motion, dynamics, bubble-bubble interactions, diminishing the coalescence, minimizing the mass transfer, etc. There have been some research works concentrated on bubbly flows to study the impact on the whole system when surfactant is added and concentration is varied, with the aim to monitor the impact on bubbles and drops.

Majority of studies on bubble dynamics with presence of the surfactant have been focused on rising bubbles. In the case of rising micro bubbles released in a vertical wall bounded flows, Takagi and Matsumoto 2011 accomplished a series of experimental studies to show the configurations of the released bubbles in a vertical tunnel. This experiment has been a complementary study of Takagi et al. 2008 and explained bubble motion in presence of surfactant. The results confirm the effects of aqueous surfactant solution on the vertical bubble motion and its lateral migration. On the other hand, the drag force upon the bubble in this case is similar to the case of solid sphere. These conclusions for the rising bubble started assigning new physical features for the bubble and surrounding flow via surfactant. Another fascinating experiment for rising bubble with soluble surfactant was Clift et al. 1978. Their study outcomes proved that the terminal velocity of a rising bubble with soluble surfactant is two times lower than purified water. Apart from forces and concentration of surfactant on the interface of the inclusion, trajectories of the bubbles in a vertical bubble column ($0 < Re < 400$) have been characterized in the case of various solutions of soluble surface active agent by Tagawa et al. 2010. First, they have distinguished the rising bubble path difference in diverse surfactant substances. Their experimental studies show that not only does surfactant reduce rising velocity, but also the trajectory of the rising bubble changes from zigzag to spiral depending on the type of employed impurities. Moreover, their experimental results evidenced a decreasing of the lift and drag coefficient of the soaring bubble in the condition of higher concentration.

The other outstanding work related to the effects of surfactant on a rising bubble has been done by Pesci et al. 2018. They conducted a direct numerical simulation (DNS) to better understand the local quantities of the surfactant on the interface of the rising bubble, and a comparison between the instantaneous rising velocity between direct numerical simulation and experimental data has been done. The authors infer that results of numerical simulation collapse with experimental data. Furthermore, their simulation visualized the surfactant distribution on the interface during the rise (local surface coverage). In the case of linear shear flow, numerical simulation of Fukuta et al. 2008 validate of lift force value variation upon the gas bubble by modifying the ratio of adsorption to desorption. In other words, by decreasing the desorption factor, large gradients of surface concentration occur and the lift coefficient on a bubble placed in a shear flow becomes much smaller than for a clean bubble.

1.2 Context of present study

This PhD project focuses on fairly large bubbles (in terms of volume and Reynolds number compared to previous studies) released into a high-speed solid body rotating flow around a horizontal axis. This flow situation is interesting because it can help us understand the behavior of bubbles when they pass through flow regions with locally high vorticity. These high vorticity regions are particularly interesting because of their existence in several flow situations such as Green 2012 mixing layers, turbulence, recirculating flows and body wakes. They are characterized by low pressure minima at their center. In various cases, a review of the literature shows that bubbles approaching these high vorticity regions are deflected toward the vortex core and trapped inside the minimum pressure region. This habitual bubble tendency has already been investigated by numerous researchers. For instance, measuring the forces on microscopic bubbles entrained by a vortex is done by Sridhar and Katz 1995 with implementing the particle image velocimetry algorithms to find velocity and acceleration of the bubble and liquid. Their results shows that for the tiny bubbles with diameter range $55\mu m < d < 800\mu m$ and rather low Reynolds number of $20 < Re < 80$, the drag coefficient is similar to that of a solid sphere. These drag results confirm the independency of the drag and vorticity for these microscopic gas bubbles. In addition, the lift only depends on fourth root of local vorticity. Jha and Govardhan 2015 investigated the interaction between single bubble and vortex ring.

In other words, the effects of bubble on vortex dynamics and vice versa has been experimentally explored. Other instances include: Cavitating bubbles in the tip vortices of propellers (see chapter XVIII by Chahine in Green 2012, Choi and Chahine n.d.), and still very recently by Cabut et al. 2021 with air bubbles trapped in counter rotating vortex inside tire grooves of a rolling car. Perhaps one of the most amazing examples of bubbles trapped by vortices is that given by videos of captive dolphins at play Marten et al. 1996. In all these situations the question is to know why and how the bubbles move towards the center of the vortex and are trapped. Answering this question requires to identify the forces acting on the bubbles in these situations. The seminal experiment of Naciri 1992 showed that the horizontal solid-body rotating flow, is rather representative of vortex regions and was adapted to measure some of these forces. He found that bubbles released in this type of flow experience, like in shear flows (Legendre and Magnaudet 1998, Tomiyama et al. 2002, Takemura et al. 2002, Hayashi et al. 2020), a lift force that, adding to the other radial forces (pressure and added mass), make them spiral towards an equilibrium position located more or less close to the rotation axis, according to the rotation speed. The coordinates of this equilibrium position were used to measure the drag and lift coefficients. Since that experiment, the behavior of bubbles or solid particles in a horizontal solid-body rotation flow has been the object of several studies. Most of these studies address the determination of the drag and lift coefficients, either numerically or experimentally from the equilibrium position. For instance, Van Nierop et al. 2007 performed experiments on spherical bubbles with Reynolds number up to 500. In accordance with their investigation, when the bubble is set in its equilibrium position, all the forces shall be modeled to be computed. Their results demonstrate that for the bubbles with Reynolds lower than 5, lift force has robust dependency on viscous effect and is negative. Bluemink et al. 2010, Bluemink et al. 2008 experimentally and numerically investigated the drag and lift forces on freely rotating sphere in this flow situation. In addition, the wake behind spherical drop has been recorded when is positioned close to the axis of rotation. With a similar experimental apparatus Rastello et al. 2009 examined the dynamics of a contaminated bubble in equilibrium position, in a surrounding solid rotating flow. The force balance and measurements depend on the position of the bubble. The authors took care to only study bubbles at a distance larger than six times the radius, in order to avoid interaction of the bubble with its wake. Consequently, the essential condition is being far enough from the axis

of rotation. They expanded their experimental results in Rastello et al. 2011 to determine acting forces along with bubble behavior in a situation in which the interface is clean. Silicon was chosen as surrounding liquid to prevent slipping interface. The equilibrium position, lift, drag and ellipsoidal bubble shape have been determined. Eventually, Rastello et al. 2017 enlarged their results with a series of new experiments to present comparisons of the dynamics of clean and contaminated bubbles in a solid-rotating flow. They tested both spherical and deformed bubbles in a series of experiments. They found that when the interface is contaminated, the bubble experiences an extra lift force, whereas when the interface is clean it does not. Furthermore, in the same Reynolds number range (up to 700), the deformation of a bubble with a clean interface (ultra-purified water) is greater than the deformation of a bubble with a contaminated interface. All the mentioned research work for solid body rotating flow has been limited to moderate rotation speeds, which prevents the bubble coming too close to the axis of rotation and thus disturb the solid-body rotating flow. Different situations were investigated, the case where the interface is clean (silicone oils, Rastello et al. 2011) and the case where the interface is partially or fully covered by impurities (water, Rastello et al. 2009, Rastello et al. 2017). When the surface is contaminated and only in that case, the bubble was shown to rotate with characteristics that are very similar to those of solid spheres immersed in that kind of flow Bluemink et al. 2008; Bluemink et al. 2010. This results in an extra "Magnus-like" lift force and a separated wake behind the bubble, whose separation angle (the angle from the bubble rear at which the wake detaches from the bubble) is higher than that observed at the same Reynolds number on a solid non-rotating sphere in a uniform flow Johnson and Patel 1999. Details on this separated wake were recently reported in Rastello and Marié 2020.

1.3 Objectives

The novelty of this study compared to previous ones lies in the high rotation speeds which are explored. In that case the bubble stabilizes close to the rotation axis, thus mimicking the bubbles trapped in a vortex core. The problem was analytically formulated by Rosenthal 1962, the effect of gravity being neglected. The bubble that is assumed spherical at zero rotating velocity is shown to stretch with its length increasing along the rotation axis as the rotation speed increases. The author derives a mathematical expression providing the bubble elongation

as a function of the rotation speed, for a given bubble volume (the corresponding model is detailed in chapter 3). He also performs a stability analysis of these bubbles subjected to small sinusoidal disturbances, and shows that within the axisymmetric assumption considered, increasing the rotation speed stabilizes the bubble. Our objectives for the present research work can be listed as below:

- I To investigate the interface deformation of an air bubble close to the axis of rotation. To check experimentally if bubbles still behave in a comparable way as predicted by Rosenthal 1962 when buoyancy breaks the symmetry of the problem. Practically, we inject bubbles of various given volumes in a cell rotating along a horizontal axis, and study their shape and aspect ratio as a function of the rotation speed (discussed in chapter 3). Furthermore, our objective is to investigate the stability of these bubbles, and determine if they can break-up.

- II In chapter 4, we will show that we can use bubble position to determine the forces acting on the bubble. The main goal of this chapter will be to measure the mean drag and lift forces, for conditions of relatively high Reynolds number.

- III In chapter 5 we will add surfactant to the rotating tank to analyze dynamics changes of the bubble such as deformation, resulting consequences on the acting forces (lift, drag, etc.) and rupturing. Bibliography demonstrated that contaminant on the interface can modify the effective forces and deformation in several flow configurations. As it has been mentioned in the previous part, Rastello et al. 2017 modified the liquid in their experiments to visualize the air bubble in silicon, but the impact of introducing surfactant and the consequences on particle dynamics and break-up is still an open question.

2.1 Experimental Set-up

To investigate the behavior of a gas bubble in a highly rotating flow, we use the experimental apparatus shown in figure 2.1. A cylindrical Plexiglas tank of inner

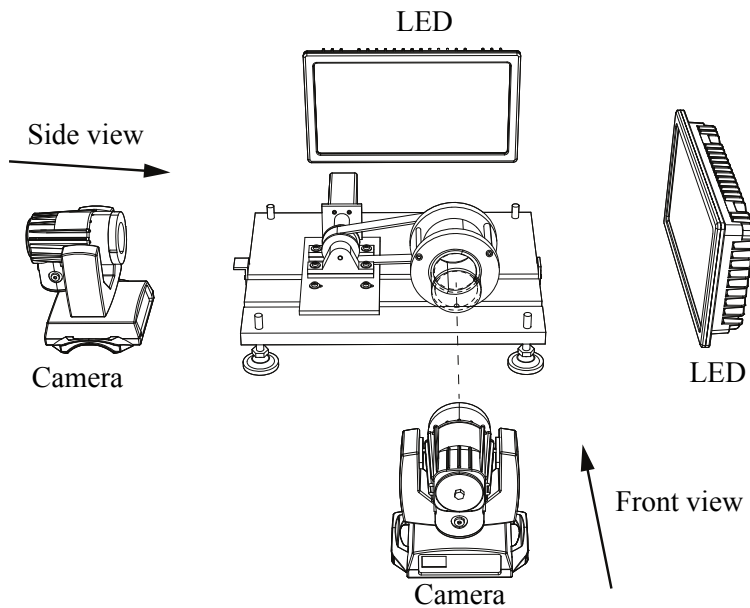


Figure 2.1: Sketch of the experimental set-up showing the positioning of the cameras relative to the rotating tank

diameter 11 cm and length 10 cm is rotated around its horizontal axis z . The tank is fixed in a cylindrical counter bore and the contact is made using ball bearings. The tank is entrained by a motor, via a tooth belt. For this experiment, the range of comparatively high rotational velocity (compared to previous research studies) ω investigated is [600-900] rpm, i.e. from 63 rad s^{-1} to 94 rad s^{-1} . Three holes on the side of the tank are used to fill the tank with water, or to inject an air bubble

illustrated in figure 2.2. The water used here is demineralised water similar to the one previously used in Rastello et al. 2009. It is characterized by a resistivity of $0.3\text{M}\Omega\text{cm}$. This resistivity is in between the one of ultra purified water of Duineveld 1995 ($18\text{M}\Omega\text{cm}$) and the one of tap water ($3\text{k}\Omega\text{cm}$). Because of operating constraints (bubble injection, temperature measurements, etc.), it was difficult to keep this water clean, which means it *a priori* contains contaminants. These few contaminants are mainly solid impurities and/or traces of tensio-actives entering the tank and scattered in the liquid.

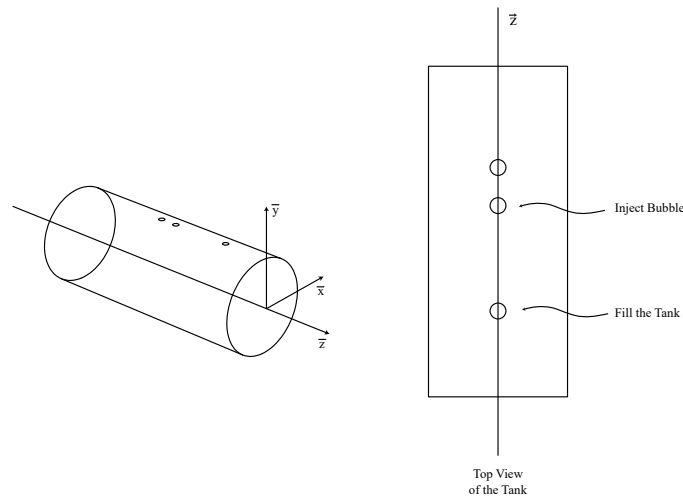


Figure 2.2: Position of the holes upon the tank used to fill demineralised water and to inject gas bubble.

2.1.1 Flow characteristics

For the general form of the flow inside the tank, and by calling continuity equation with a velocity field of $V = (u_r, u_\theta, u_z)$ in cylindrical coordinates we have:

$$\frac{\partial \rho}{\partial t} + \frac{1}{r} \frac{\partial(\rho r u_r)}{\partial r} + \frac{1}{r} \frac{\partial(\rho u_\theta)}{\partial \theta} + \frac{\partial(\rho u_z)}{\partial z} = 0$$

As the rotating flow is steady ($\frac{\partial}{\partial t} = 0$) for a fixed ω , and because the velocity field can be assumed axisymmetric ($\frac{\partial}{\partial \theta} = 0$), then we will have

$$u_r = \frac{A}{r}$$

because of the boundary condition at the wall $u_r = 0$, we have constant $A = 0$. Therefore, $u_r = 0$. Then, we write θ -component of Navier Stokes equation in cylindrical coordinates:

$$\rho \left(\frac{\partial u_\theta}{\partial t} + u_r \frac{\partial u_\theta}{\partial r} + \frac{u_\theta}{r} \frac{\partial u_\theta}{\partial \theta} + \frac{u_\theta u_r}{r} + u_z \frac{\partial u_\theta}{\partial z} \right) = -\frac{1}{r} \frac{\partial P^*}{\partial \theta} + \mu \left[\frac{1}{r} \frac{\partial}{\partial r} \left(r \frac{\partial u_\theta}{\partial r} \right) - \frac{u_\theta}{r^2} + \frac{1}{r^2} \frac{\partial^2 u_\theta}{\partial z^2} + \frac{2}{r^2} \frac{\partial u_r}{\partial \theta} + \frac{\partial^2 u_\theta}{\partial z^2} \right]$$

where $P^* = P + \rho g y$. Under the same assumptions of steady and axisymmetric velocity field, and injecting $u_r = 0$, it can be shown that the solution is of the form:

$$u_\theta = Ar + \frac{B}{r}$$

where A and B are constants. We know necessarily $B = 0$, because, otherwise velocity diverges at $r = 0$. By using the boundary condition at the outer cylinder at $r = R$ (R is radius of the cylinder) where the velocity is fixed at ω , we find $A = \omega$. Therefore, u_θ can be deduced as $u_\theta = \omega r$. Then by contribution of the r -component of Navier Stokes equation in cylindrical coordinate (incompressible, isothermal Newtonian flow), we write:

$$\rho \left(\frac{\partial u_r}{\partial t} + u_r \frac{\partial u_r}{\partial r} + \frac{u_\theta}{r} \frac{\partial u_r}{\partial \theta} - \frac{u_\theta^2}{r} + u_z \frac{\partial u_r}{\partial z} \right) = -\frac{\partial P^*}{\partial r} + \mu \left[\frac{1}{r} \frac{\partial}{\partial r} \left(r \frac{\partial u_r}{\partial r} \right) - \frac{u_r}{r^2} + \frac{1}{r^2} \frac{\partial^2 u_r}{\partial \theta^2} - \frac{2}{r^2} \frac{\partial u_\theta}{\partial \theta} + \frac{\partial^2 u_r}{\partial z^2} \right]$$

Under the same assumptions as precedingly, we obtain:

$$\frac{\partial P^*}{\partial r} = \rho \frac{u_\theta^2}{r}$$

Therefore, by replacing $u_\theta = r\omega$, the pressure profile will be parabolic:

$$P^* = \frac{1}{2} \rho r^2 \omega^2 + P_0$$

There is a constant P_0 which is the pressure at the center of the tank.

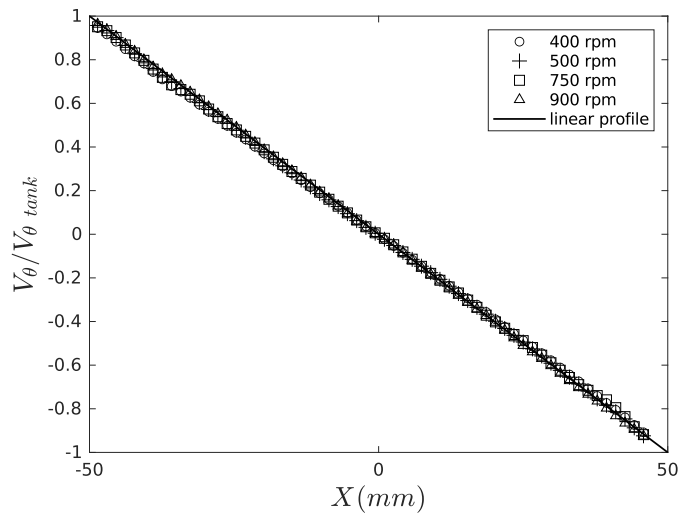


Figure 2.3: Mean flow profiles scales by the rotation speed of the tank (X is radial axis of front view). Extracted from Rastello et al. 2009

In addition, with the experimental set-up exhibited in figure 2.1, the rotating flow without bubble was characterized by particle image velocimetry (PIV) measurements in Rastello et al. 2009 on the present experimental set-up. Averages of 100 flow fields show that the mean flow profiles were linear over the whole section of the tank. Results clearly showed that the mean velocity profile was linear as expected for a solid body rotation and matched the velocity of the tank at the wall. As an evidence, we join a PIV mean velocity map for 900 rpm (figure

2.3) and the mean velocity profiles for 400, 500, 750 and 900 rpm scaled by the tangential velocity of the tank (figure 2.4). This map was obtained by averaging 100 instantaneous maps. It shows that all the profiles remained linear.

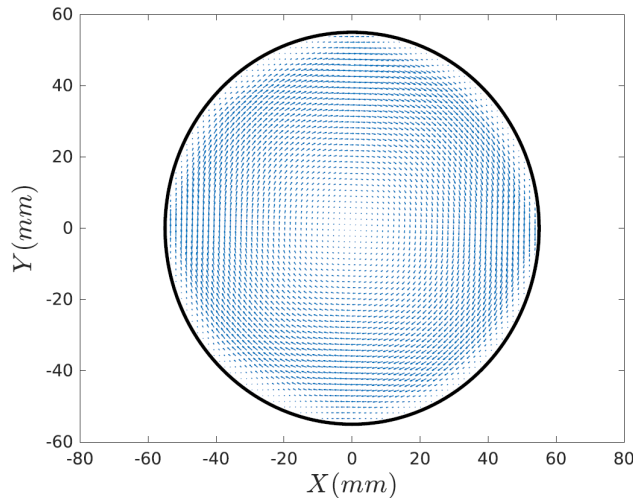


Figure 2.4: PIV Flow map for 900 rpm ($\omega = 94 \text{ rad s}^{-1}$)

2.1.2 Bubble injection, surface tension measurements and other physical parameters

Bubbles can be injected when the cell is at rest. Because the volume of the injected bubble is an important parameter for our calculations, we have used three different fixed needle Hamilton syringes allowing volumes of injected bubble in the range of $[5-1000] \mu\text{l}$. When the rotating motor is launched at indicated rotational velocity ω ($[600-900]$ rpm) the observed deformation of the bubble is qualitatively similar to an ellipsoid, and the bubble stretches along the axis of rotation z (form of the stretched bubble illustrated in figure 2.5). In addition, the volume V at a given ω can be measured via image processing. This measurement will be explained in details in section 2.2, by assuming that the bubble is an ellipsoid and by measuring its axes on the front and side view projections. This measurement of volume has been implemented to increase the accuracy of the volume taken into account for our calculations.

Surface tension was measured with a pendant drop tensiometer (*Attension Theta*

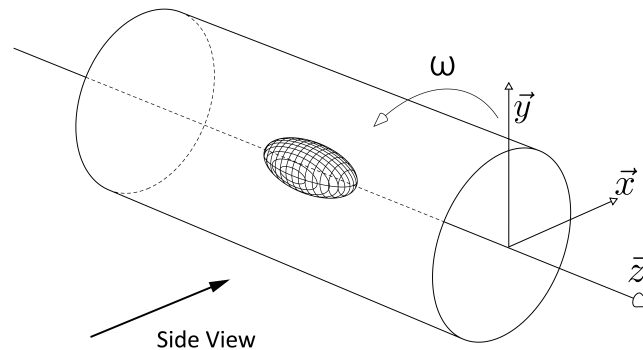


Figure 2.5: Configuration of the present problem, showing an approximately axisymmetric bubble lying close to the axis of rotation z .

Flex, Biolin Scientific AB) shown in 2.6. This device involves a needle located in front of a high-resolution camera. The software algorithm automatically detects the contour of the drop at the tip of the needle. It retrieves the shape profile and using Young Laplace model provides the corresponding surface tension value. To maintain the stability of the drop, we make sure not to touch the apparatus or the bench to avoid parasitic vibrations. The surface tension for the demineralised water was close to 71.8 ± 1.0 mN/m in average for all experiments. We averaged over decades of seconds, enough to have a converged value and not too long to avoid evaporation effects.

The liquid temperature was measured before each series of experiments, with a digital Testo 106 thermometer. This temperature was comprised between 20°C and 21°C for each experiment. A small short term increase of temperature, of at most one degree, was observed in the course of measurements. The corresponding uncertainty on viscosity is expected to be below 5%.

2.2 Image Processing

In order to understand the dynamics of our targeted bubble at the center of rotation, we detect and extract its physical features along with its behavior by implementing some image analysis algorithms. To do this, the first principal step is to detect the shape of the bubble to have an overview about the general



Figure 2.6: Left: Tensiometer used to measure precise surface tension of used liquid. Right: droplet released from Gauge needle in front of high resolution camera to measure instantaneous surface tension .

configuration of the bubble. This step requires high accuracy particle detection algorithms and proper back light imaging. Additionally, in order to have a clean series of images to detect the shape of the bubble, we require a deliberate bubble injection without other small bubbles or extra particles disrupting the images. As it has been displayed in figure 2.1, two cameras are used to record the bubble shape and position: a *Phantom 4.3 V360* is used to record images normal to the axis of rotation (*side view*, and in particular the stretching of the bubble along this axis of rotation). A second camera, *Basler acA800* is positioned perpendicular to the first, along the axis of rotation (*front view* in figure 2.1). Lighting is achieved with two LED panels, one for each camera. The cameras are synchronized to record simultaneously the bubble at a frame rate of $F = 200$ Hz. The resolution is fixed at 600×800 pixels for both cameras. For each injected bubble volume and given ω , a set of 255 synchronized images is recorded.

Several images of the deformed bubble for rotational velocity in the range [600-900] rpm, i.e. from 63 rad s^{-1} to 94 rad s^{-1} . The images captured from *front view* and *side view* are shown in figure 2.7. The bubble configuration exhibits approximately an ellipsoidal shape.

2.2.1 Particle detection

In order to improve our image analysis techniques, we can zoom in on the region where the bubble fluctuates, and crop the image around the bubble. As an example, the zoomed image recorded by *Phantom 4.3 V360* for a bubble of

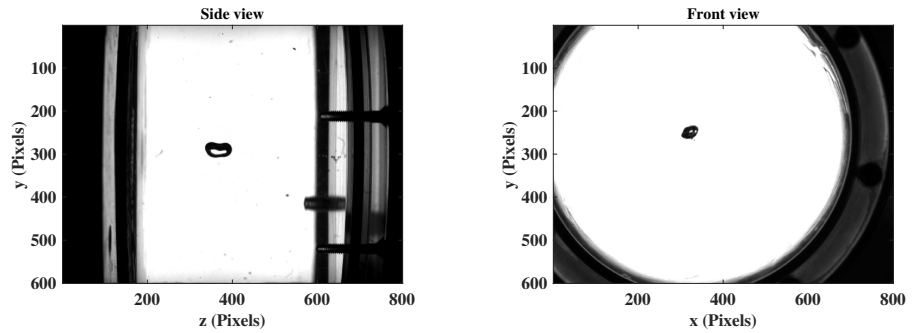


Figure 2.7: **Left:** Example of image recorded by *Phantom camera (side view)*. **Right:** Example of image recorded by *Basler camera (front view)*.

volume $V = 0.27\text{cm}^3$ is illustrated in figure 2.8. Afterwards the process of particle detection can be initialized.

The initial part of the bubble detection is the conversion of our images to gray-

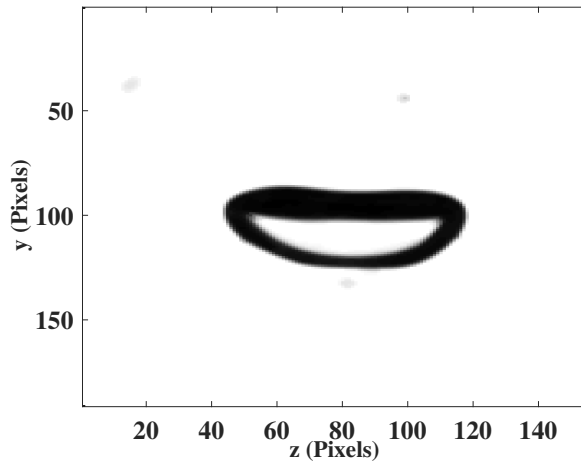


Figure 2.8: Zoomed frame in the crop box of bubble displacement *Phantom (side view)*

scale. Then, we implement a median filtering of the image in two dimensions. This step is an effective method to reduce noises to preserve the edges. In addition, since the bubble is large and properly detectable at the plane, we imbinarize the image to convert pixel values above a determined threshold to ones and setting

all other values to zeros. Then, by using the complement image, we will optimize the clearance of the bubble (figure 2.9, left). Afterwards, we fill entirely the remained object with the *strel*, *imclose* and *imfill* Matlab functions (figure 2.9, right). Eventually the outer boundaries of the holes inside the biggest detected object are traced. In this step, the function *regionprops* has been used. As it has already been remarked, the configuration of the bubble can be considered approximately ellipsoidal. Thus, we extract all the principal components (major axis, surface area, minor axis, orientation, perimeter, center of the mass, etc.) of the detected ellipse with this *regionprops* function (figure 2.10).

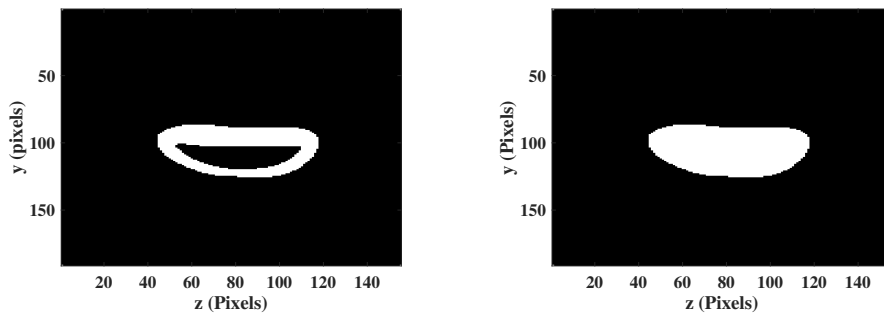


Figure 2.9: **Left:** Binary image + complementing of figure 2.8, after implementing of the noise removing algorithms (*mat2gray*, *medfilt* Matlab functions). **Right:** After imposing *strel*, *imclose* and *imfill* Matlab functions to keep the biggest object.

First results from the shape of the bubble as an ellipse confirm that the bubble in such high rotating velocities tends to stretch along the horizontal axis. In addition, it oscillates around z . As it oscillates, there is not a distinct equilibrium position and the interface fluctuates. This physical phenomena is observed from the oscillations of L and D shown in figure figure 2.11. Accordingly, with this evidence from the behavior of the bubble and its deformation, we can characterize the shape of the bubble with these length scales (L and D) in figure 2.12.

2.2.2 Camera synchronization and Calibration

Calibration

In order to deduce real length scales for our bubble measurements, calibration for each camera is an essential step. For instance, for the *side view* the surface

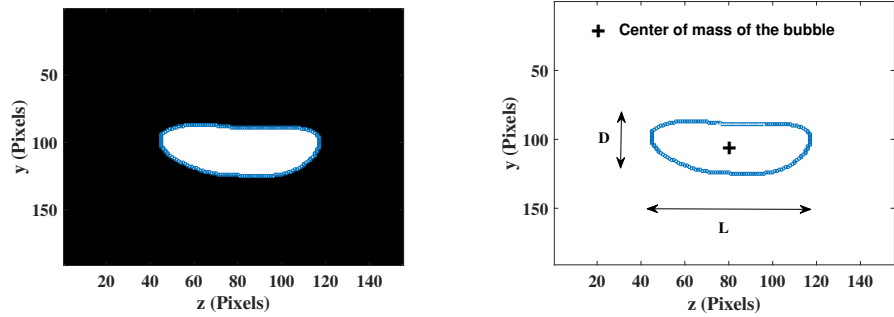


Figure 2.10: Left: Boundary detection of the biggest object. *Phantom* (side view). Right: Boundary detection of the biggest object (same bubble as figure 2.9 with Major (L) and minor axis (D) of the ellipse).

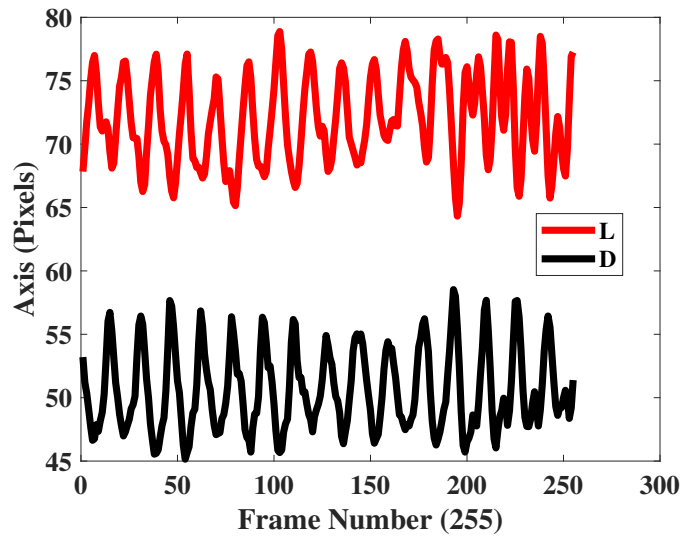


Figure 2.11: Variations of L and D for an example experiment for $V = 0.25\text{cm}^3$ at $\omega = 700\text{rpm}$

of the cell has a finite curvature (because of the shape of the tank). Thus, all the measurements from image processing of the gathered image sequences of *Phantom* must be converted to the real scale in both y (vertical direction) and

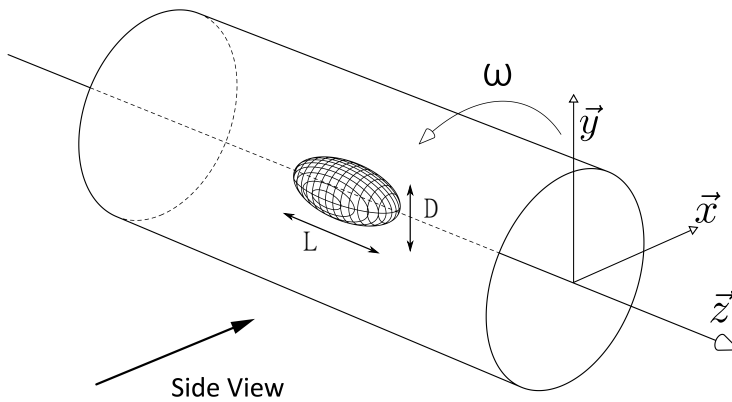


Figure 2.12: Configuration of the present problem, showing an approximately axisymmetric bubble lying close to the axis of rotation z .

z (horizontal axis direction). To overcome this issue and obtain the real scale of the bubble, we have designed a rectangular metal bar which can be inserted inside the tank from the holes (figure 2.13). This metal bar has been marked vertically via colored points along the y direction. The distance between each of the marked signs is 0.5 cm and the horizontal distance between the two corners for the calibration in z direction is $d = 6.2$ cm.

When the bubble is positioned close to the axis of rotation, it is trapped in the spot covered by the designed rectangular bar (figure 2.14).

Then, we need to measure the scale of y ($scale_y$) which depends on the y position (because of the tank curvature) for a given experiment. Afterwards, for expressing the output lengths of *Matlab* scripts in SI unit in z and y direction, we will have to multiply by $scale_z$ and $scale_y$ respectively.

Concerning the *Basler* camera calibration, we observe that the camera superposes the front plane (the plane positioned at Z_0 in figure 2.15) and the back plane (the plane positioned at Z in figure 2.15). To expand, the parallax for the captured bubble by the *Basler camera* must be taken into account to get an accurate scale conversion value at the given z position of the bubble. Indeed, depending on the position of the bubble along the z axis, the scale seen by the front view camera will change. This z coordinate of the bubble center of mass can be deduced from the *side view* images taken by the *Phantom camera*, for

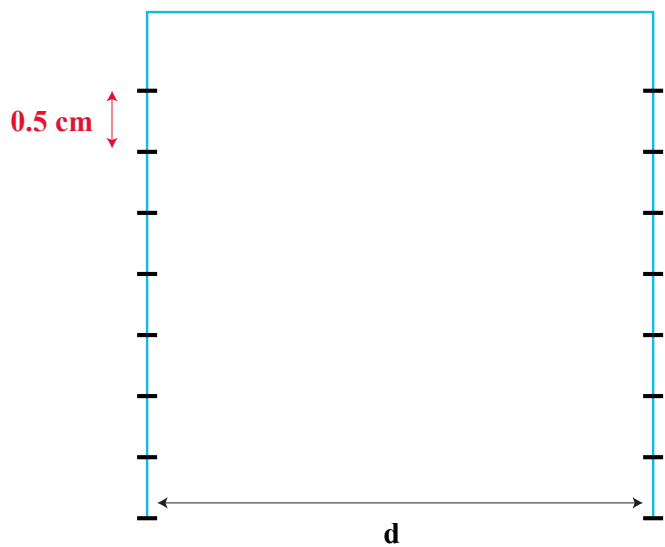


Figure 2.13: Designed metal bar with colored marked points for *side view* calibration

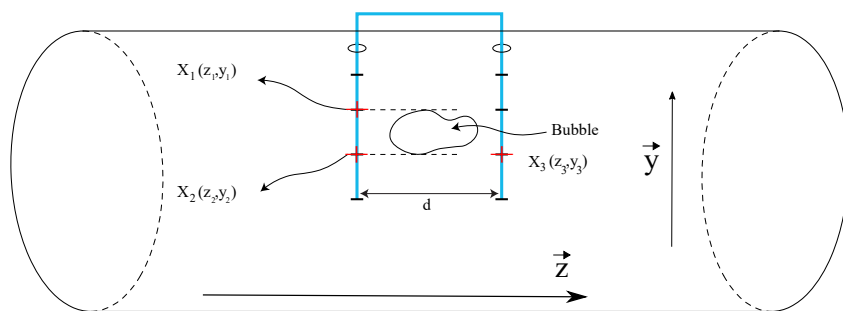


Figure 2.14: Schematic of the bubble inside the rectangular calibration metal bar.

each set of images of a specific rotating velocity ω . We therefore account for the parallax effect with the following method: We introduce a linear equation for the scale depending on the position of the bubble along the horizontal axis. We stick a transparent circular plastic with a dashed lines pattern to the front (Z_0) and back (Z) planes separately and record each with the front view Basler camera. We then measure the scale $scale_{Z_0}$ on the front view by using the y coordinates

of two points O_1 and O_2 separated by a distance D (figure 2.15):

$$scale_{Z_0} = \frac{y'_1 - y'_2}{D \text{ (cm)}}$$

We then stick the pattern to the back plane at Z , and measure the distance between two points P_1 and P_2 from which we similarly deduce:

$$scale_Z = \frac{y_1 - y_2}{D \text{ (cm)}}$$

As there is a linear relation for the calibration of plane Z and Z_0 , a linear function depending on the position of the bubble with slope m can be proposed as:

$$m = \frac{scale_Z - scale_{Z_0}}{Z - Z_0}$$

$$scale_{bubble}(Z_{bubble}) = scale_{Z_0} + m (Z_{bubble} - Z_0)$$

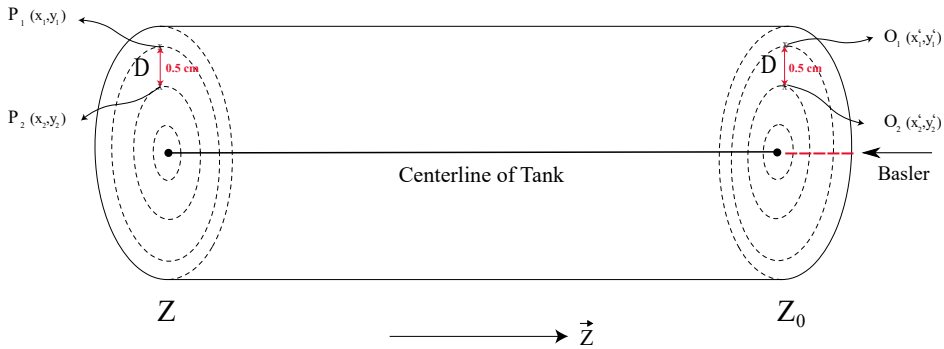


Figure 2.15: Stuck dashed pattern to the front plane (at Z_0) and background plane (at Z) separately.

In this function Z_{bubble} can be determined by finding the center of mass position in z from image analysis of the *side view* recording (see figures 2.16 and 2.17). It is evident that the center of mass oscillates around a fixed point in different omega. The position in z can vary in each image acquisition when we

change ω . Therefore, Z_{bubble} is defined as the mean value of z for each rotating velocity.

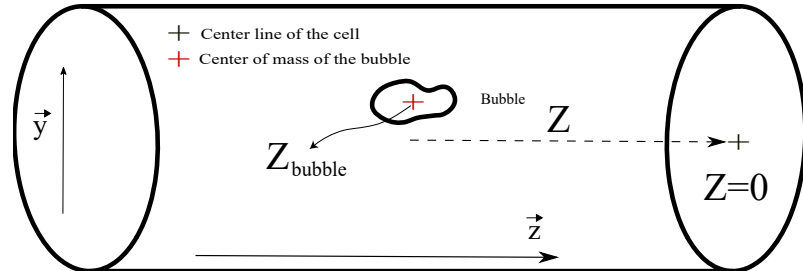


Figure 2.16: Configuration of z position of the bubble measured with *Phantom* camera

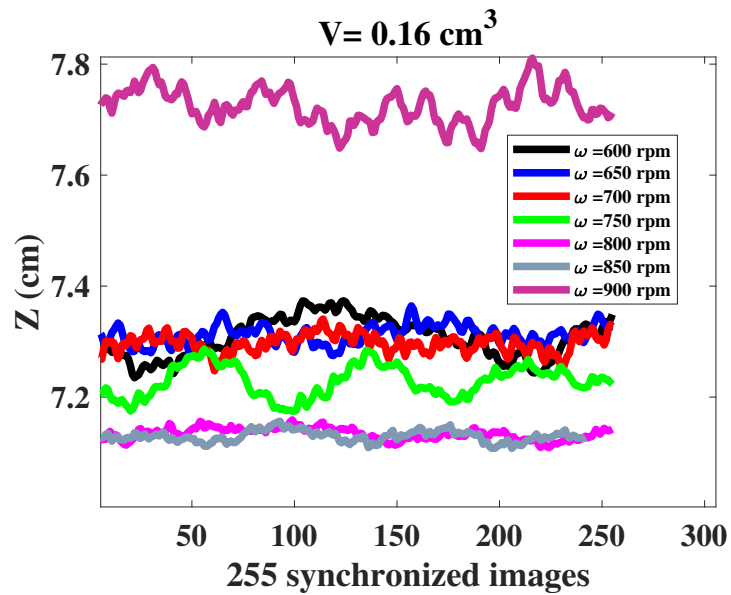


Figure 2.17: Center of mass oscillation of a bubble of volume $V = 0.16 \text{ cm}^3$ in diverse rotational velocities: the average of these values is used to measure Z_{bubble} position.

Cameras synchronization

Image acquisition and synchronization of both cameras are based on the *Phantom 4.3 V360*. This implies that the *Phantom camera* is the master to adjust the features of recording such as the frame rate. In fact, the *Phantom camera* in all the process before recording initialization is storing images in its circular memory buffer and we assigned it in post-trigger mode with capability of storing 1700 images before acquisition instruction. On the other hand, the maximum number of images that the *Basler camera* can have in its buffer is 255. Consequently, the total number of recorded images of the *Phantom camera* is 255 (synchronized) + 1700 (before *Basler camera*). Note that the frame rate of both cameras is fixed at 200 Hz.

When the *Phantom camera* enters into recording mode, it triggers the recording of the *Basler camera*. The internal clock of the *Phantom camera* is used as external clock of the *Basler camera*. However, it is mandatory to similarly capture images in various experiments (different volumes of the bubbles) to preserve consistency and accuracy of our data. This signifies the images should be captured at the same time interval for each bubble size at different rotational velocity. We use a signal generator to send a TTL signal to the camera, in order to launch the recording process (figure 2.18). The moment that we push the start bottom of the signal generator, it sends a TTL signal to the *Phantom camera* to record and likewise *Phantom camera* governs *Basler camera* acquisition (see figure 2.18 and 2.19).

A verification of the accuracy of our calibration along with consistency of the two cameras can be carried out by checking independently a defined value called dy for both cameras. We choose to check the maximum vertical distance of the boundary points in each ω during bubble sharp undulations (figure 2.20). To obtain this value, in image analysis script, a function measuring the maximum and minimum vertical values of the boundary points over 255 images is composed (see figures 2.21 and 2.22). This function deduces the distance between mentioned maximum and minimum point in each image and store them as a vector. Thus, to have a comparison of dy between *Phantom* and *Basler* in each ω we take into account the mean value of this quantity through the 255 synchronized images. So, if the mean values of dy (255 images) of each camera are close to each other, the synchronization and precision of our calibration shall be validated (see figure 2.23).

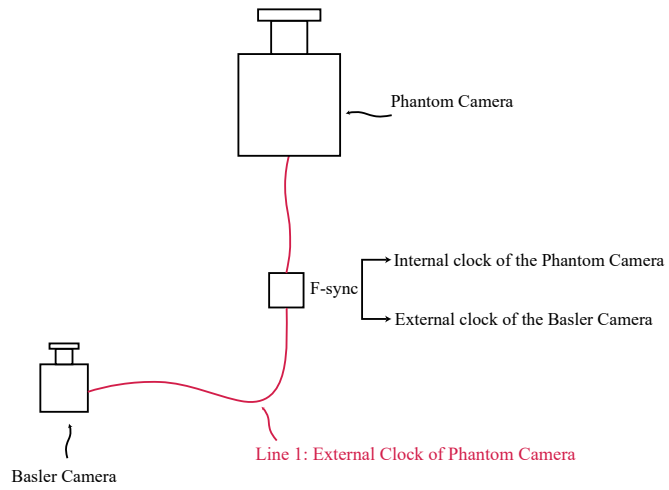


Figure 2.18: Technical assembly of the cameras synchronization.

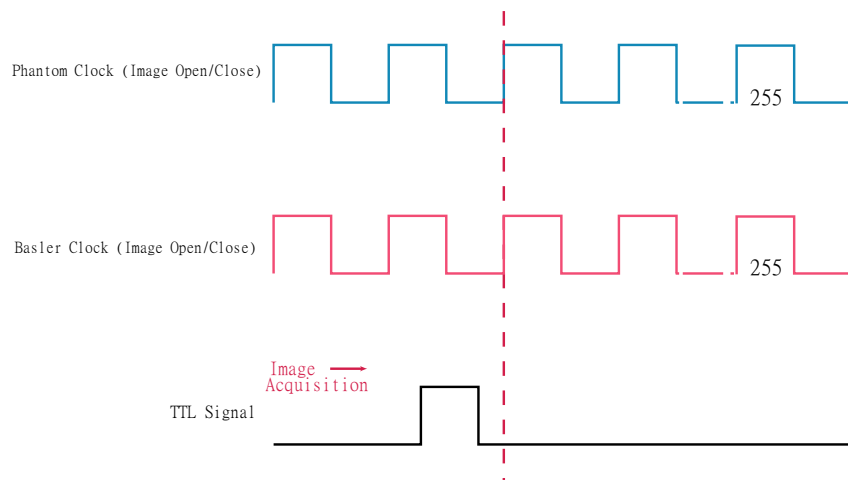


Figure 2.19: Sending TTL signal from the generator to the *Basler* and *Phantom* cameras clock. 255 synchronized images (for each camera separately) recorded after sent TTL signal of the generator.

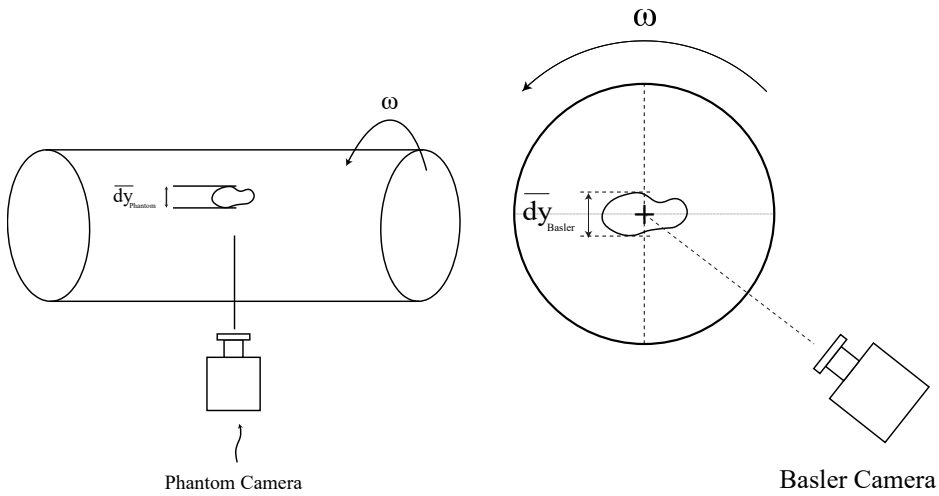


Figure 2.20: **Left:** Maximum vertical distance of the bubble recorded by *side view*. **Right:** Maximum vertical distance of the bubble recorded by *front view*.

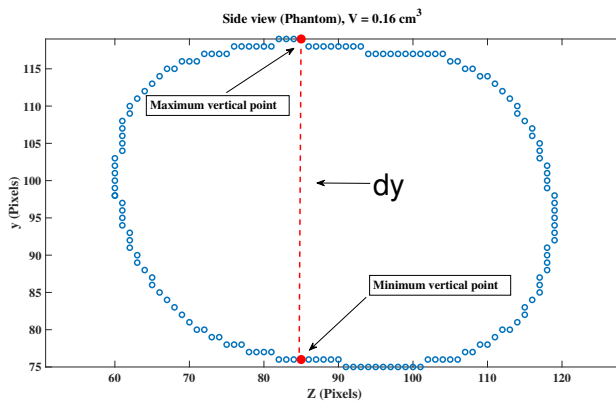


Figure 2.21: Schematic of the two chosen point by program for measuring maximum vertical distance through the boundary points *side view*.

Finding the center of the tank

Finding accurately the coordinates of the center of the cell on our images is crucial since the distance of the bubble to the axis of rotation is essential in order to understand the velocity seen by the bubble. The inner and outer walls

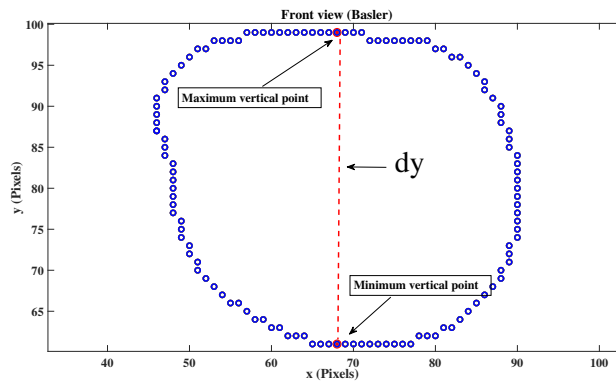


Figure 2.22: Schematic of the two chosen points by program for measuring maximum vertical distance through the boundary points *front view*.

of the cell are not entirely visible with eyes and there are range of restrictions to measure the center of the cell manually. We have tested different means to precisely find the center of the tank with a high accuracy. For instance, a first method we tried consisted in sticking a colored circular paper label (red disk in figure 2.24) to the approximated position of the cell center. Then we explored the center of this red disk in series of consecutive images, on the back wall of the tank. The mean value of found centers of the red disks represents the coordinate of the center of the tank. Note that in this method we take the center of the circle described when the red disk rotates, we do not rely on the disk being centered. We finally used a different, and more convenient, method for finding the center of the tank: we use a *Matlab* function which gives the center of a circle once the user has clicked on three points belonging to the circle. We chose three regularly spaced points belonging to the inner wall of the tank, and the outputs of the function are then the radius and coordinates of the center of the circle. In our case this method works better and is an efficient solution as from the front view image (*Basler*) parts of the contour of the inner wall are apparent and by clicking on three random points on the interior wall we can obtain the center of the circle around these three points. Figure 2.25 shows the line of inner wall as well as three chosen random points to be clicked. Moreover, figure 2.26 shows a zoomed part of the inner wall and figure 2.27 illustrates the center found by our *Matlab* function.

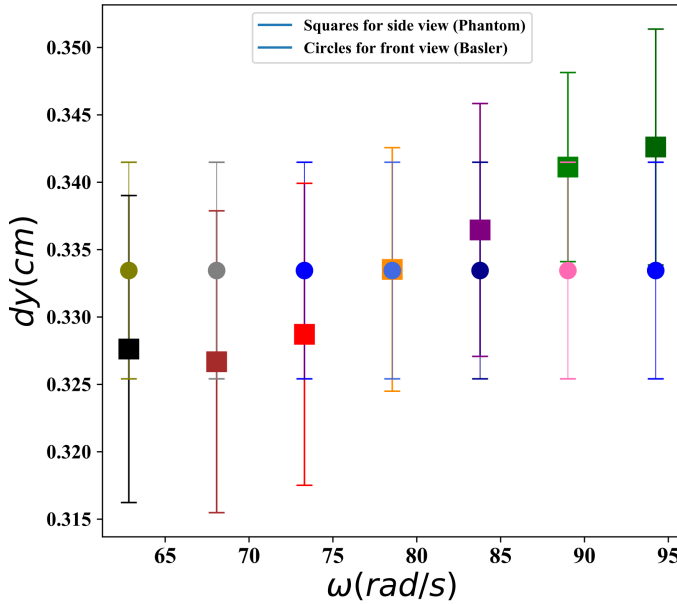


Figure 2.23: Mean vertical distance of the boundary in each ω for both views (*front view* and *side view*) where \square is related to *side view* and \circ is the value of *front view* for a bubble with volume of $V = 0.16 \text{ cm}^3$.

We carry out this method for each series of the images for a given ω , to improve the accuracy of found centers. Subsequently, we calculate the mean value of the centers for various ω . We define (X_C, Y_C) as the value of the center of the tank for each experiment $(X_C, Y_C) = \text{mean}(X_1 : X_7, Y_1 : Y_7)$ (see table 2.1).

2.2.3 Volume measurement and experimental data

As already explained in section 2.1.2, bubbles can be injected when the cell is at rest, with three different fixed needle Hamilton syringes and the injected volume V_0 of the bubble is therefore a priori known with a precision of μL . The value of volume can be read from the Hamilton syringes.

In the following, each series of data points, corresponding to a same injected

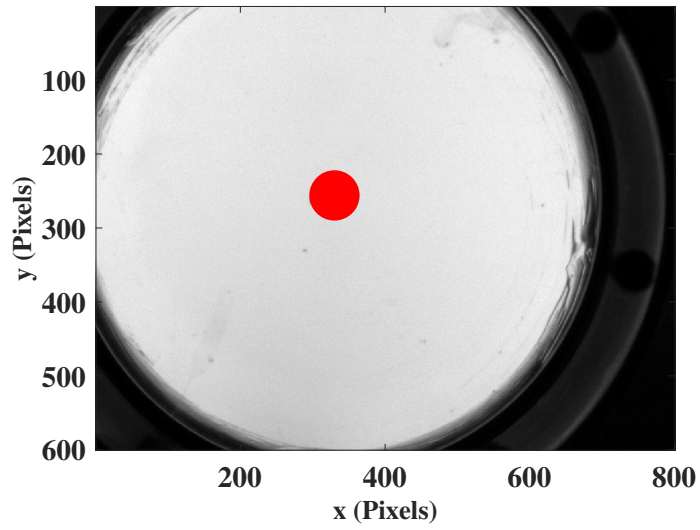


Figure 2.24: Labeling estimated position of the center with colored circular paper.

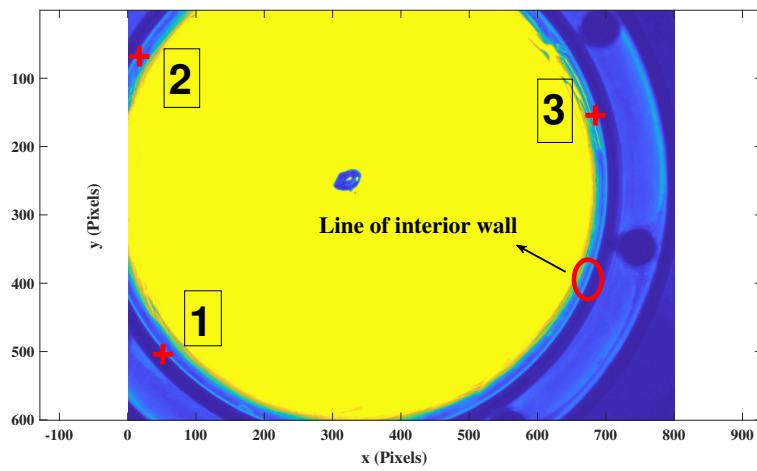


Figure 2.25: Three chosen clicked points on the interior wall of the cell as inputs of the *Matlab* function extracting the center of the circle made by these points.

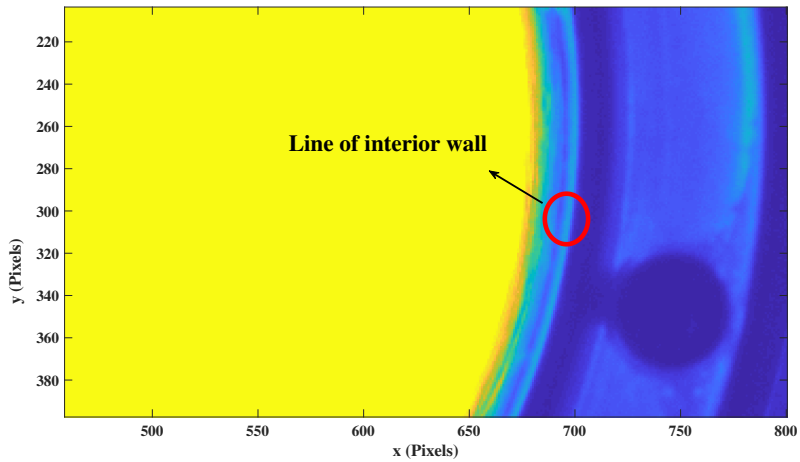


Figure 2.26: Contour of the interior wall of the tank to be clicked.

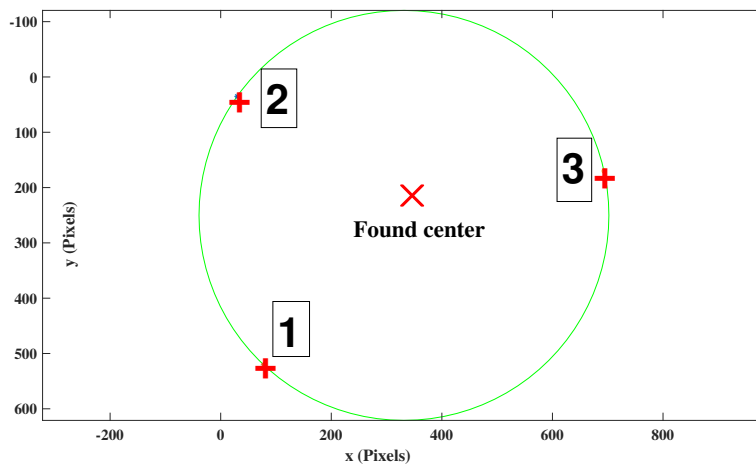


Figure 2.27: Found center of the circle circumscribed by line aligned with three clicked points.

bubble, is labeled by the mean volume V measured with this method over the range of ω . Note that for all the series, the volume of the bubble is very small

$\omega(\text{rad s}^{-1})$	$X_{\text{center}}(\text{pixels})$	$Y_{\text{center}}(\text{Pixels})$
62.83	X_1	Y_1
68.06	X_2	Y_2
73.30	X_3	Y_3
78.53	X_4	Y_4
83.77	X_5	Y_5
89.01	X_6	Y_6
94.24	X_7	Y_7

Table 2.1: Coordinates of tank centers found by three chosen points of interior wall for various ω .

compared to the volume of the cell (the ratio of volumes goes from 10^{-7} to $3 \cdot 10^{-4}$ for the biggest bubble). In order to be more explicit on the relevant bubble length scale for each series, we provide in table 2.2 a correspondence between V and the mean radius R_{eq} of an equivalent bubble with a spherical shape.

However, to filter out uncertainties on the final bubble volume introduced by the simple reading of the sample in the syringe (refraction effects when level reading; sometimes parasitic micro-bubbles created at the same time as the main bubble), we also measured the volume V at a given omega via image processing. Indeed, by assuming that the bubble is an ellipsoid and by measuring its axes on the front and side view projections (figure 2.28):

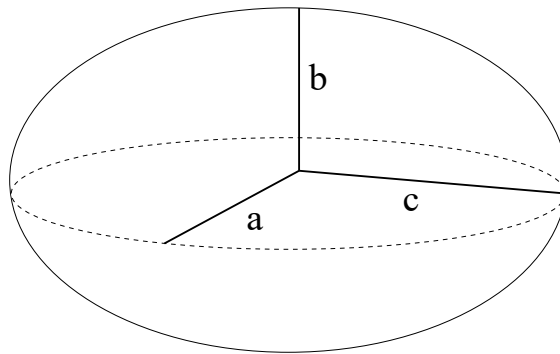


Figure 2.28: c and b are the major and minor axis of ellipsoidal bubble from *side view* images. a is the major axis of *front view*.

$$V = \frac{4}{3} \pi a b c$$

↓

For each image frame, $V = \frac{4}{3} \pi \frac{L}{2} \times \frac{D}{2} \times \frac{D}{2}$

↓

Therefore, for 255 synchronized frames for each ω ,

↓

$$\boxed{V = \frac{1}{6} \pi \times \text{mean}(L D^2)} \tag{2.1}$$

Mean volume V [cm ³]	Mean equivalent radius R_{eq} [cm]
0.00069	0.055
0.0039	0.098
0.0064	0.115
0.0071	0.119
0.012	0.14
0.020	0.17
0.028	0.19
0.035	0.20
0.038	0.21
0.051	0.23
0.061	0.24
0.089	0.28
0.11	0.30
0.17	0.34
0.22	0.38
0.25	0.39
0.27	0.40

Table 2.2: Characteristics of the bubbles: mean volume V and radius R_{eq} of a spherical bubble of equivalent volume.

Measurements of volume at low ω are typically within 5% of the injected volume V_0 . For the larger ω investigated, a small increase in the volume of the bubble with ω is typically observed, up to 15% for most series. We interpret this increase as due to the elastic deformation of the plexiglas tank, as detailed below. This phenomenon can be explained by the pressure difference seen by the wall of the cylindrical tank (ΔP_{wall}). We can write Barlow's formula to compute the elastic deformation of the tank wall with thickness of e as:

$$\Delta P_{wall} = P_0 + \frac{1}{2}\rho\omega^2 R^2 - P_{atm} = \frac{e}{R} E \frac{\Delta R}{R} \quad (2.2)$$

where $E = 3 \times 10^9 \text{ Pa}$ is the Young modulus of plexiglas and R is the radius of the tank. Then by writing the volume conservation relation for the whole tank we have,

$$\Delta V_{bubble} + \Delta V_{water} = \Delta V_{tank} \quad (2.3)$$

The volume variation of the tank can be estimated as,

$$\Delta V_{tank} = \Delta(\pi R^2 L) = 2\pi RL \Delta R$$

The volume variation of the bubble can be related to P_0 at the center of the tank with compressibility β_{bubble} as:

$$\beta_{bubble} \simeq \frac{1}{P_{atm}} = -\frac{1}{V_0} \frac{\Delta V_{bubble}}{\Delta P}$$

where β_{bubble} is the volume compressibility coefficient and $\Delta P = P_0 - P_{atm}$. We have assumed that:

$$\Delta V_{bubble} = V_0 \left(1 - \frac{P_0}{P_{atm}}\right)$$

The volume fluctuation of the water is defined as below where $\beta_{water} \simeq 10^{-10} \text{ Pa}^{-1}$,

$$\Delta V_{water} = \beta_{water} V_{water} (P_0 - P_{atm})$$

In our experiment the volume of the water filling the cylindrical tank is $V_{water} \simeq 800 \text{ cm}^3$. This means that the estimate for $\Delta V_{water} \simeq 10^{-7} \text{ cm}^3$. More-

over, V_{bubble} in our experiments have been up to $V_{bubble} = 0.25 \text{ cm}^3$. Then, the order of magnitude of ΔV_{water} is 10% of bubble volume. Thus, we can neglect the volume variations of water and maintain solely ΔV_{bubble} in equation 2.3 and rewrite it as :

$$\begin{aligned} \Delta V_{bubble} &= \Delta V_{tank} \\ V_0 \left(1 - \frac{P_0}{P_{atm}} \right) &= 2\pi R L \Delta R \end{aligned} \quad (2.4)$$

Now, with contribution of equations 2.2 and 2.4, we have two equations and two unknowns (ΔR and P_0) leading to a prediction for ΔV_{bubble} as a function of ω and V_0 . The experimental variations of the volume are illustrated in figure 2.29. The data points are the volumes of the experimental data showing for different sizes of the bubble how the volume increased, with $\Delta V_{bubble} = V_\omega - V_0$ where V_ω is the measured volume from relation 2.1 in each rotating velocity and V_0 is the volume of injected bubble into the cell with Hamilton syringes at the beginning of the experiment. Figure 2.29 shows the volume variations predicted by equations 2.2 and 2.4.

As it is apparent, there is an increase of volume in our range of rotational velocities for both experimental data and theoretical model. The model predicts that the volume can vary up to $\approx 14\%$ (figure 2.30). On the other hand, the experimental data shown in figure 2.29 display that the volume variation is up to $\approx 24\%$, which is a bit larger but of the same order of magnitude. Note that for the tiny bubbles of volume $V = 0.0039 \text{ cm}^3$ as well as $V = 0.0064 \text{ cm}^3$ the increase is much larger up to $\approx 80\%$ which is huge. The reason of this sudden volume variations of these small bubbles in experimental data compared to the model could be that these bubbles are not seeing P_0 at the center of the tank as they are not aligned with the axis. In the derivation of equation 2.4, it is assumed that the bubble is always straddling the axis of rotation and pressure P_0 is pressure at the center of the bubble which is the same as the pressure at the center of the tank. Nevertheless, in our experiments the bubble is not entirely centered and when the bubble is small enough, the interface does not straddle the axis of rotation. Thus, by increasing ω the pressure seen by the bubble P_0 decreases because of two distinct reasons: the decrease in P_0 modeled in figure 2.30, and the fact that the small bubbles moves closer to the axis when omega is increased.

The other point in figure 2.29 that should be remarked is the volume variation of the bubble with $V = 0.028 \text{ cm}^3$. The volume variation for this bubble is negative

at the beginning (figure 2.29). The reason is possibly the precision of noted volume injected by the Hamilton syringe and the noted value may have been underestimated.

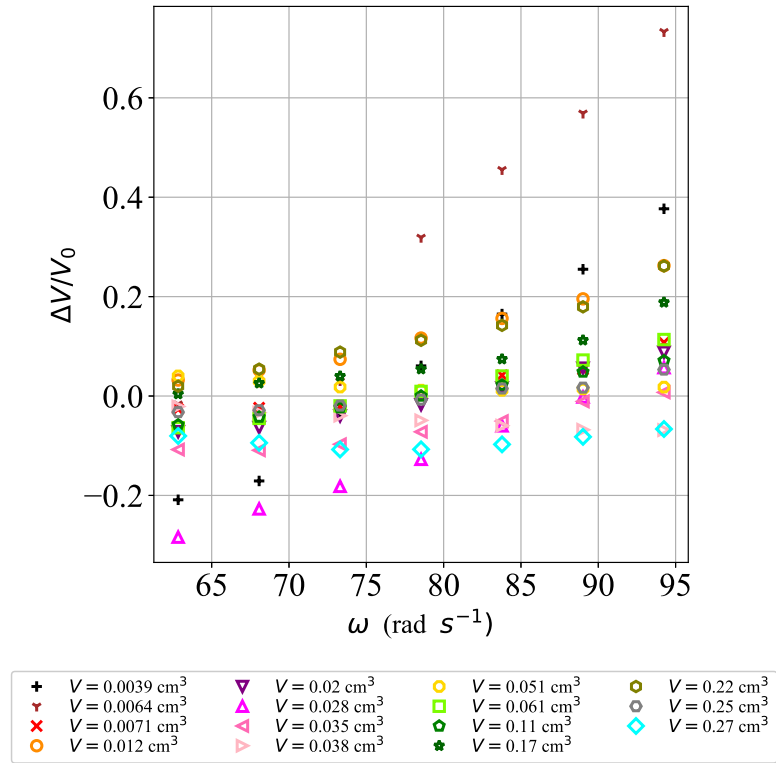


Figure 2.29: Variation of volume (assumption of ellipsoidal shape) via increasing ω measured with the method presented in section 2.2.3 for all the experimental data shown in table 2.2. $\Delta V_{bubble} = V_{\omega} - V_0$ where V_{ω} is the volume of the bubble with ellipsoidal shape in related ω and V_0 is the volume of injected bubble by syringe.

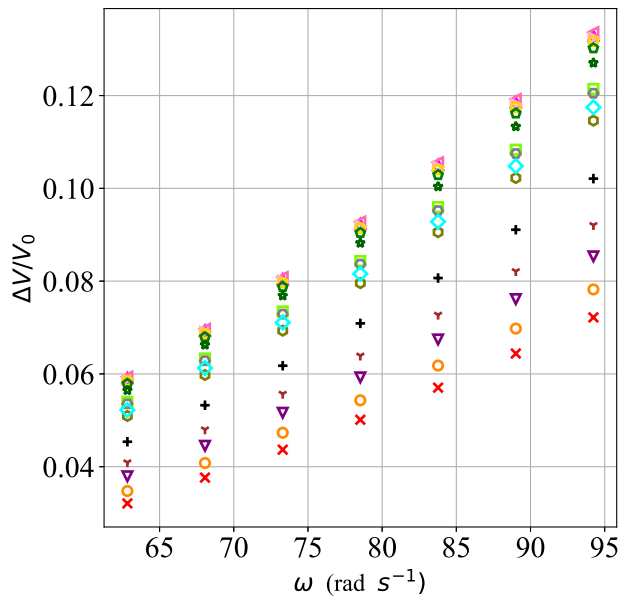


Figure 2.30: Variation of volume predicted by model discussed in equations 2.2 and 2.4 for the same volume size of experimental data via same legend as figure 2.28 with assumption of $\Delta V_{bubble} = V_{\omega} - V_0$. Same legend as figure 2.29.

2.3 Bubble equilibrium position

When the cell is rotated, the bubble migrates towards the axis of rotation. For moderate rotation frequencies, we observe that bubbles oscillate around their mean position with an amplitude large compared to the bubble size. This is illustrated in figure 2.31, with the red curve showing the vertical y and horizontal position z of the center of a bubble of volume $V = 0.14 \text{ cm}^3$ along the axis of the cell as a function of time, for $\omega = 31 \text{ rad s}^{-1}$. The values of y and z are made dimensionless with $R_{eq} = 3.2 \text{ mm}$, the radius of a spherical bubble of equivalent volume $V = 0.14 \text{ cm}^3$. The bubble exhibits strong oscillations around its mean position, of an amplitude comparable with the bubble size. The frequency of the vertical oscillations corresponds to the frequency of the rotating cell. The horizontal position fluctuates with an even larger amplitude (up to 15 mm), and at a lower frequency. When ω is increased up to $\omega = 89 \text{ rad s}^{-1}$, the bubble moves closer to the axis of the cell: for this larger frequency the amplitude of the

bubble oscillations is strongly reduced along both directions, and becomes small compared with R_{eq} (blue curve). A closer look at the motion of the bubble shows that bubbles follow a limit cycle around the mean position (figure 2.32). This limit cycle is reminiscent of the behavior observed recently for rigid spheres in the experiments of Sauma-Pérez et al. 2018, even though the latter experiments have been carried out at much lower Re . Our objective in the following is to focus on the mean position of the bubble as a function of rotation frequency and bubble size: we therefore chose to focus on ω in the range $[63 - 94] \text{ s}^{-1}$, for which the amplitude of the bubble oscillations remains moderate compared to the bubble dimensions. The upper value of 94 s^{-1} corresponds to the maximum ω that can be reached with the motor entraining the cell.

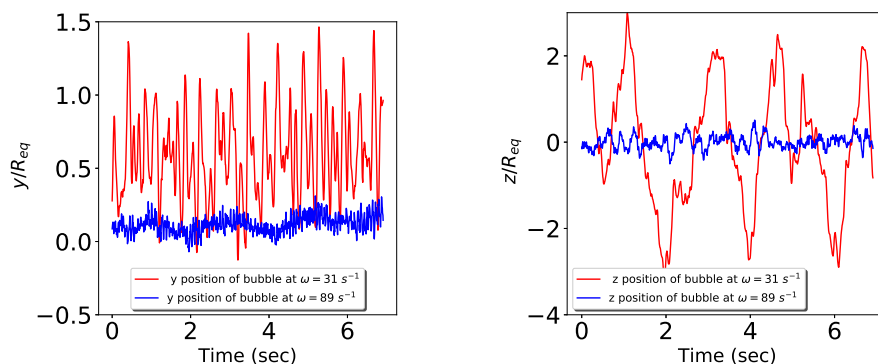


Figure 2.31: **Left:** Variation of dimensionless vertical position y of a bubble of volume $V = 0.14 \text{ cm}^3$ ($R_{eq} = 3.2 \text{ mm}$) as a function of time, for two rotation rates. The origin of y is taken on the axis of rotating cell, and the vertical position is made dimensionless with the equivalent spherical bubble size R_{eq} . **Right:** Same plot for dimensionless horizontal position (z) along the axis of the cell, with origin of z taken at the mean position of the bubble. The fluctuations are much smaller for the larger rotation rate.

All the quantities introduced in the following sections related to the bubble size and position are measured for each image, and then averaged over the total number of images recorded by each camera. The standard deviation around these averaged values will be indicated by the error bars.

We will assume in the modeling that the bubble is axisymmetric, of character-

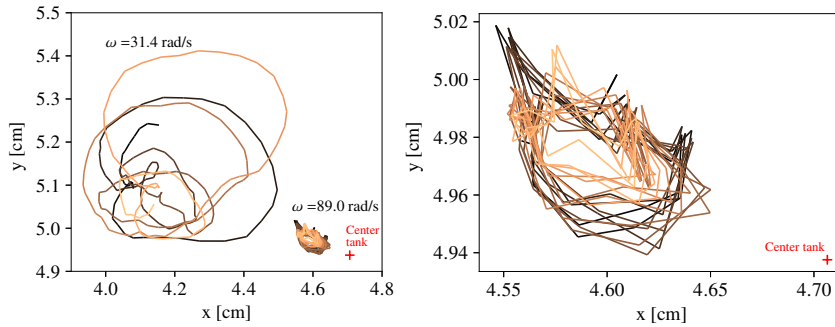


Figure 2.32: Left: Path followed by the center of the bubble with $V = 0.14 \text{ cm}^3$ and two experiments at $\omega = 31$ and 89 rad s^{-1} . Time goes from dark to light color in the gradient color line. Right: Zoom on smaller cycle for the case $\omega = 89 \text{ rad s}^{-1}$.

istic lengths L and D (figure 2.12). As illustrated in figure 2.33 and 2.34, for the larger bubbles investigated this assumption is not strictly valid, but the aspect ratio measured on front view projections remains smaller than 1.4 even for the larger bubbles and all ω investigated. For each image the equivalent bubble diameter D for a given injected volume and ω is then defined from the *front view* projection as the mean value between minor axis and major axis dimensions (as measured with the *Matlab* `regionprops` function). The length L is directly measured as the major axis from the side view projection, with the same *Matlab* function.

2.4 Dimensionless Parameters

We now wish to identify the parameters, and corresponding dimensionless numbers, needed to describe the equilibrium position and the shape of a bubble of volume V placed in a solid-body cylindrical rotational flow. As mentioned before, we assume the bubble is axisymmetric, and characterize its shape with two length scales: a length scale L corresponding to the dimension of the bubble along the axis of rotation z , and the smaller length scale D , corresponding to the mean diameter of the bubble projection in a plane normal to the axis of rotation (see figure 2.5).

We introduce three dimensionless numbers to describe the shape of the bubble: the aspect ratio $X = L/D$ which measures the stretching of the bubble, aspect

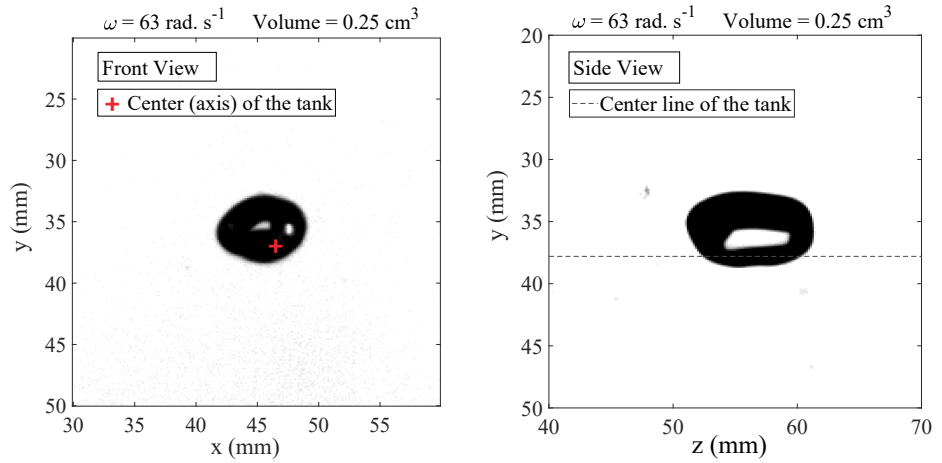


Figure 2.33: Left: Front view for a bubble of volume $V = 0.25 \text{ cm}^3$ ($R_{eq} = 3.9 \text{ mm}$), at $\omega \approx 63 \text{ s}^{-1}$. Right: Same bubble and same conditions simultaneously recorded from side view.

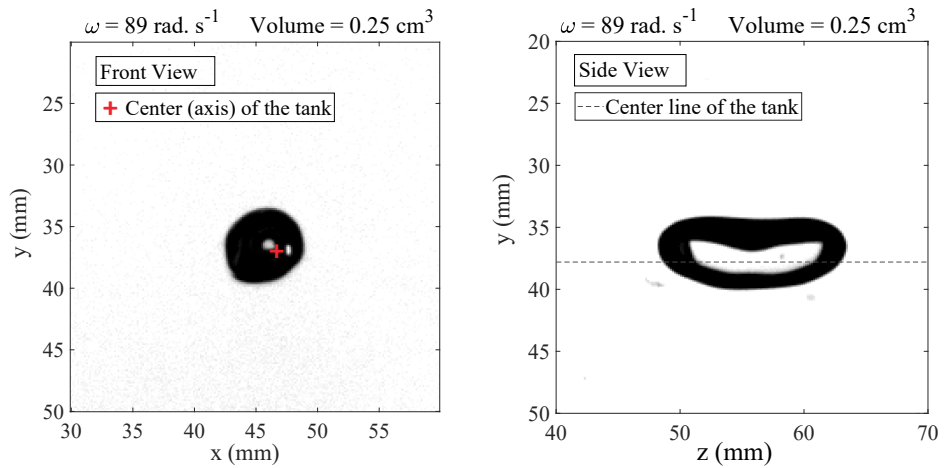


Figure 2.34: Left: Front view for a bubble of volume $V = 0.25 \text{ cm}^3$ ($R_{eq} = 3.9 \text{ mm}$), at $\omega = 89 \text{ s}^{-1}$. Right: Same bubble and same conditions simultaneously recorded from side view.

ratio X_F defined as the ratio of major to minor axis as measured on the front view and the ratio $\alpha = V/(LD^2)$. The latter characterizes the form of the bubble

in a section containing the rotation axis z : it is for example expected to be equal to $\pi/6$ if the bubble is an ellipsoid, or to $\pi/4$ if the bubble is a cylinder. Note that the cylindrical shape is the limit shape expected for very large ω , as predicted by the model of Rosenthal 1962. We will discuss the values of X , X_F and α in chapter 3.

The physical control parameters characterizing this problem are:

- $\rho \rightarrow$ carrier liquid density
- $g \rightarrow$ acceleration of gravity
- $\omega \rightarrow$ rotational velocity of the tank
- $\sigma \rightarrow$ gas-liquid surface tension
- $\mu \rightarrow$ dynamic viscosity of the liquid

In addition, we must consider the bubble position in the cross section, which determines the flow around the bubble and hence the force exerted by the liquid upon the bubble: we characterize this position with the coordinates of the bubble centre in polar coordinates, namely the distance r_e to the axis of the cell, and the angle θ with the vertical direction (figure 2.35). The above parameters can be grouped into five additional independent dimensionless numbers as below:

- Rossby number $\rightarrow Ro = r_e/D$
- Reynolds number $\rightarrow Re = \rho\omega r_e D/\mu$
- Froude number $\rightarrow Fr = \omega^2 r_e/g$
- Weber number $\rightarrow We = \rho\omega^2 D^3/8\sigma$
- Angle $\rightarrow \theta$

Note that we have chosen to introduce a Reynolds number based upon the mean velocity seen by the bubble. An alternative choice could be to introduce a Reynolds number based upon the shear seen by the particle. This dimensionless number does not depend on r_e . This implies that the shear (ΔU) seen by the bubble imposed by the ambient flow velocity of U is:

$$\Delta U = \omega \left(r_e + \frac{D}{2} \right) - \omega \left(r_e - \frac{D}{2} \right) = \omega D$$

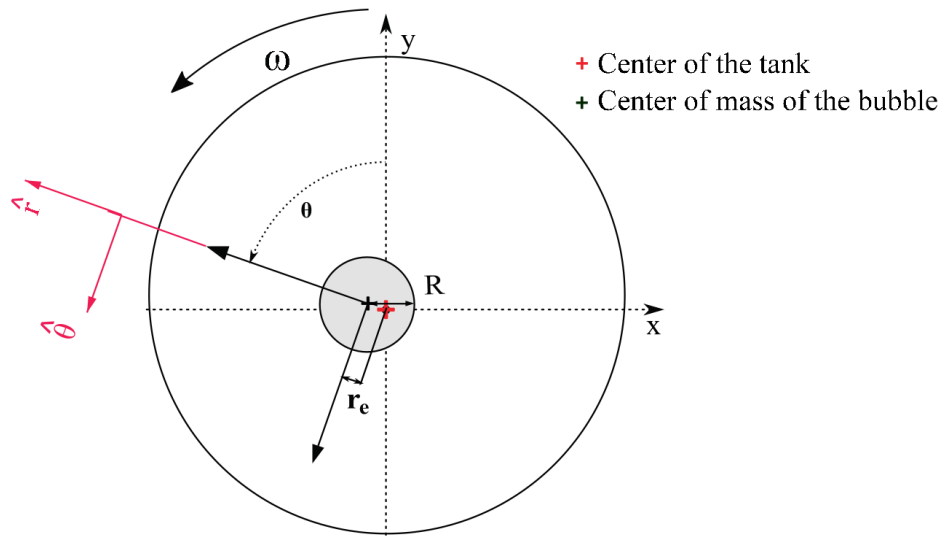


Figure 2.35: Bubble position in the cell cross-section: the center position of the bubble is characterized by r_e and θ

$$Re_{shear} = \frac{\rho\omega D^2}{\mu} = Re/Ro$$

We will discuss in chapter 4 the relevance of this choice. The liquid-gas density and viscosity ratios can also be introduced. All experiments are here carried out with air and water, and since these two parameters are constant in the present study we will not discuss them in the following.

The main control parameter driving the stretching of the bubble (discussed in chapter 3) is expected to be We , and similarly the forces acting on the bubble (discussed in chapter 4) are expected to be mostly controlled by Re . We will show in the following chapters that corrections in Ro have to be introduced when the bubble approaches the axis of rotation of the cell.

3

Deformation of the bubble

In this chapter we present results regarding the position of the gas bubble and its shape when it is close to the axis of rotation. The position of the bubble and its variations when ω is increased yield precious information regarding the flow around the bubble. Therefore, at first the mean bubble position is discussed and in the following the shape of the bubble interface is explored.

3.1 Bubble Position

As it has been explained in section 2.3 the lower rotational velocity investigated is $\omega = 63 \text{ rad s}^{-1}$ where the position of the bubble is close to the axis of rotation, but the bubble is not entirely centered. As is shown in figure 3.1, by increasing the rotating velocity of the cell, the bubble is displaced towards the center of the tank. The value of r_e is expected to be directly impacted by ω and g . We can estimate that the pressure gradient on the periphery of the bubble is equal to the buoyancy force as:

$$F_B = \Delta\rho g V_b \sim \frac{\partial P}{\partial r} \times V_b$$

$$\frac{\partial P}{\partial r} = \rho r_e \omega^2 \sim \rho g \longrightarrow r_e \sim \frac{g}{\omega^2}$$

In this simple approximation, the drag and lift forces acting on the bubble are neglected. In chapter 4 we will discuss the values of drag and lift, and explain why this assumption, though a priori strong, works relatively well. We plot on figure 3.2 the dimensionless distance to the axis r_e/D , which is exactly the Rossby number Ro introduced in section 2.4, as a function of $g/(D\omega^2)$. We see that r_e/D is smaller than 1 for most of our experimental conditions, except for the smallest bubbles investigated. The error bars on this graph correspond to the standard deviation of r_e values on the set of 255 images. In addition, figure 3.2

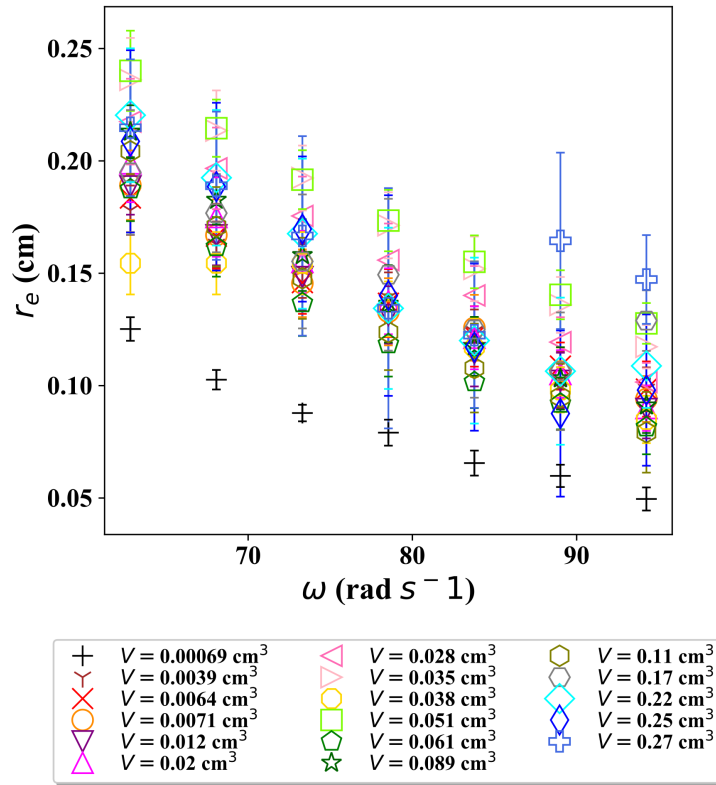


Figure 3.1: Variation of the distance of the center of the mass of the bubble to the center of the cell r_e as a function of ω .

shows that the average r_e can indeed be estimated by g/ω^2 . This is equivalent to saying that the Froude number introduced in section 2.4 is close to one for all our data (figure 3.3). The data for the smallest bubble of $V=0.69 \text{ mm}^3$ departs from this trend, and for this series r_e appears to be significantly smaller than g/ω^2 (and hence Fr significantly smaller than one). This behavior could be related to the smaller Re for this very small bubble (of order 100): we will show in section 4.2 that this results in a larger drag coefficient for this particular series than for all other (larger) bubbles.

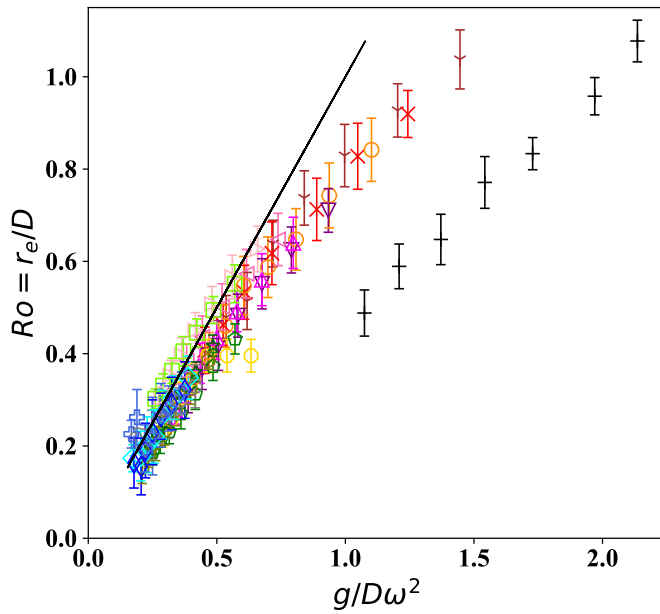


Figure 3.2: $Ro = r_e/D$ as a function of $g/D\omega^2$. Same legend as in Figure 3.6. The solid line indicates $Ro = g/D\omega^2$.

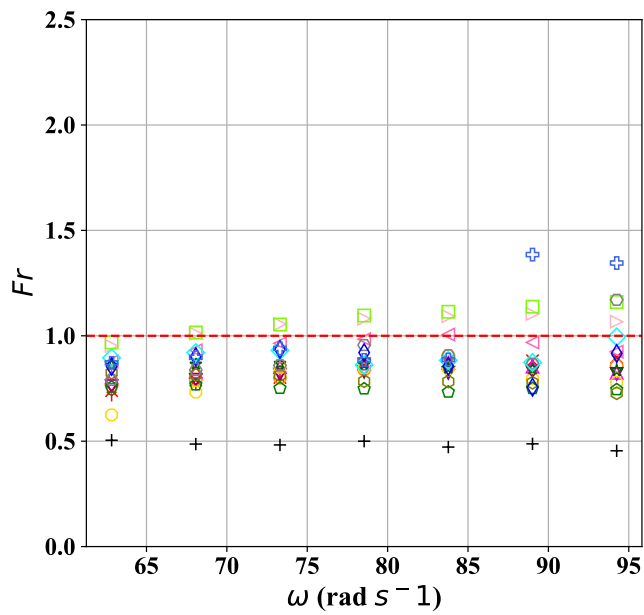


Figure 3.3: Froude number as a function of ω : the Froude number is close to one for most series, except for the smaller bubble investigated for which $Fr \approx 0.5$.

Moreover, figure 3.4 exhibits that the bubble always make the minimum angle (θ) of 50 to 89 degrees with the vertical axis and the angle is diminishing by increasing ω for all the series.

These values of θ correspond to positions where the bubble lies left of the tank center on a front view, when the rotation is anticlockwise (see figure 3.5). We will come back to the issue of the position of the bubble more detailedly in chapter 4, when discussing the forces acting on the bubble.

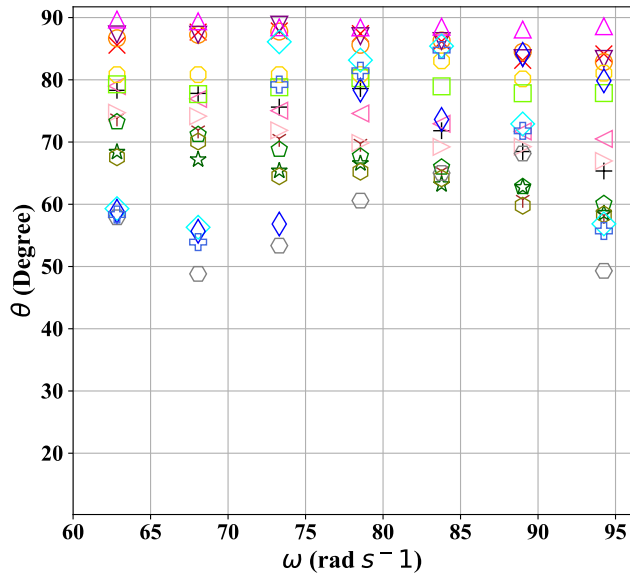


Figure 3.4: Variation of θ in degrees, ranging between $50 < \theta < 89$ as a function of ω .

3.2 Bubble deformation

3.2.1 Experimental results

We present in this subsection the measurements of the bubble aspect ratio, defined as $X = L/D$, as a function of ω and for a large range of bubble volumes V (from 0.69 mm^3 to 0.27 cm^3). As expected, we observe that when ω is increased, the bubbles are stretched along the axis of rotation (figures 2.33 and 2.34), and hence that their aspect ratio $X = L/D$ increases. Figure 3.6 shows the variations

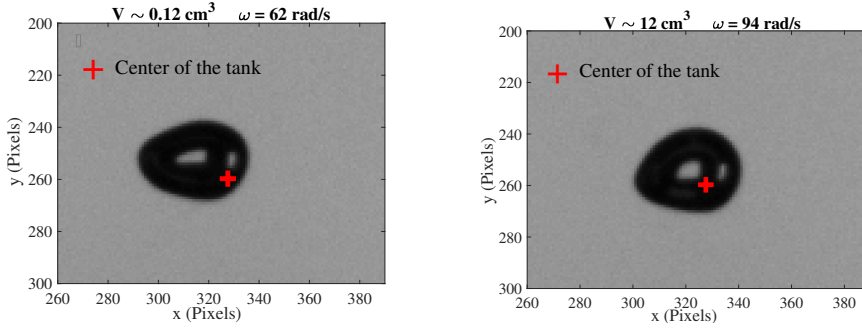


Figure 3.5: Bubble position respect to the center of the cell for a bubble of volume $V = 12 \text{ cm}^3$.

of X as a function of ω for a large range of bubble volumes. The aspect ratio increases monotonically when the volume is increased for almost all series, and reaches a value of 2.2 for the largest bubble investigated here and the largest ω . Additionally, the aspect ratio of the bubble X_F in the cross section (as measured on the *front view*) diminishes for all the series (see figure 3.7), down to values smaller than 1.25 for the largest rotation rate. This shows that the bubble is close to axisymmetric for the larger rotational velocities ω investigated.

3.2.2 Discussion of ellipsoidal shape assumption

Regarding the shape of the bubble, we define two dimensionless numbers called $\alpha = \frac{V}{LD^2}$ and $\beta = \frac{A_b}{LD}$: the latter grouping is, similar to α , a number characterizing the shape of the bubble: $\beta = \pi/4$ for an ellipsoid and $\beta = 1$ for a cylinder. At any rate, α and β are not expected to vary much when the deformation of the bubble is moderate. In particular for the range of longitudinal aspect ratio investigated here ($1 < X < 2.2$), the model of Rosenthal 1962 predicts that α varies between $\pi/6 \approx 0.52$ and 0.56, and that β varies between $\pi/4 \approx 0.78$ and 0.82, i.e. close to the value for an ellipsoid.

In order to check this experimentally, a possibility is to estimate α directly from V_0 , L and D , by assuming that V remains relatively close to the injected volume V_0 , which should be true for lower ω values (as already seen in subsection 2.2.3). We plot in figure 3.8 the variations of this estimate $\alpha_{inj} = V_0/LD^2$ as a function of ω : the values are relatively close to the ellipsoid value $\pi/6$ for all series (red

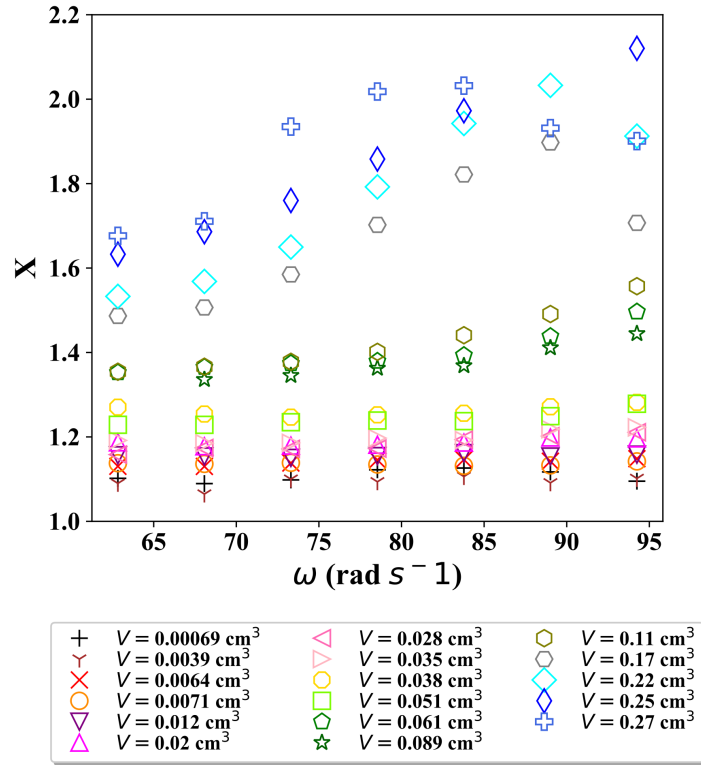


Figure 3.6: Variation of the aspect ratio $X = L/D$ as a function of ω .

dotted line), in particular for the lower value of ω . It decreases down to 0.4 for the largest ω . We interpret this decrease as caused by the fact that at large ω the volume V_0 used for the calculation of α_{inj} is an underestimation of the actual volume V of the stretched bubble (see section 2.2.3).

All in all, we observe that $\alpha \approx \pi/6 \approx 0.52$ at the lower ω . For larger ω we cannot check directly that this holds since the volume V cannot be measured reliably from the two projections given the strong bubble deformations, and α_{inj} probably underestimates α . The model of Rosenthal 1962 predicts $\alpha = 0.56$ for $\omega = 94 \text{ rad s}^{-1}$, i.e. a modest increase of about 7% from the value at $\omega = 63 \text{ rad s}^{-1}$. In order to simplify the discussion, we assume in the following that α remains close to its value for an ellipsoid, i.e. $\pi/6$ for all our conditions. Similarly, and in

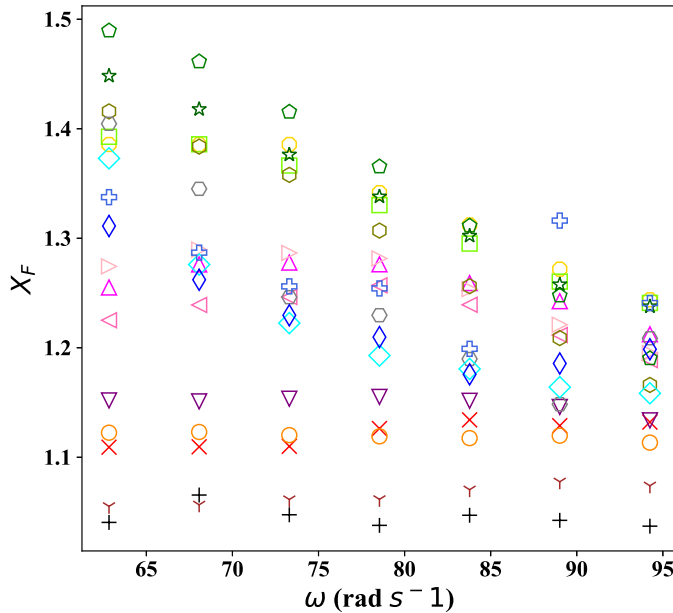


Figure 3.7: Variations of the aspect ratio X_F (aspect ratio of *front view*) as a function of the rotation speed ω . Same legend as figure 3.6.

order to be consistent with this choice, we assume $\beta = \pi/4$.

3.2.3 Model of Rosenthal 1962

The stretching of the bubble along the axis of rotation results from the difference in pressure between the region of the bubble straddling the axis of rotation, where pressure is minimal, and the periphery of the bubble: this effect has been modeled by Rosenthal 1962 in the limit of zero buoyancy and viscosity: within his model the axisymmetric bubble centered on the cell axis of rotation. The analytical solution is based on the assumption of a bubble surrounded by a liquid body with a rotating adjacent flow. The main assumptions made are:

- The bubble is axisymmetric (figure 3.9).
- The gravitational field is neglected

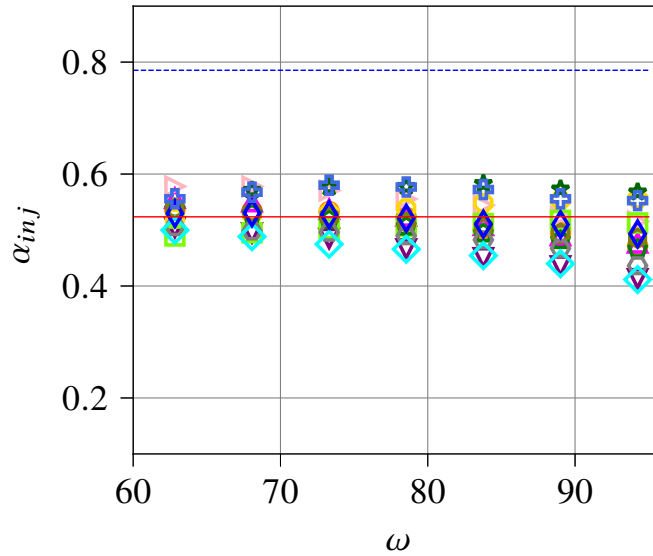


Figure 3.8: Coefficient $\alpha_{inj} = V_0/(LD^2)$ as a function of ω . The red line indicates the value for an ellipsoid $\pi/6$. The blue dashed line shows the value for a cylinder, $\pi/4$.

- Viscosity is negligible

The equation of the interface in figure 3.9 is $r = f(z)$. As it is shown in chapter 2.1 section 2.1.1, the pressure distribution in both phases of liquid and gas are :

$$\begin{cases} P_b = \frac{1}{2} \rho_b \omega^2 r^2 + P_{0b} \\ P_l = \frac{1}{2} \rho_l \omega^2 r^2 + P_{0l} \end{cases}$$

The Laplace law for the bubble is given by:

$$P_b - P_l = \sigma J$$

where σ and J are respectively the surface tension and total curvature. We can write the total curvature as a function of the distance to the axis f as (axisymmetric assumption):

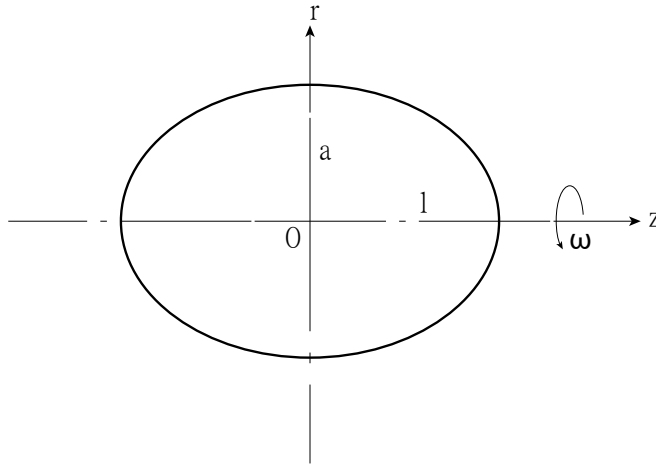


Figure 3.9: Schematic of rotating bubble around the horizontal axis of z , Rosenthal 1962.

$$J = \frac{1}{f} \frac{d}{df} \left(\frac{f}{(1+f'^2)^{1/2}} \right) \quad (3.1)$$

Then, the Laplace law can be rewritten as:

$$\frac{d}{df} \left(\frac{f}{(1+f'^2)^{1/2}} \right) = \frac{(P_{0b} - P_{0l})f}{\sigma} - \frac{(\rho_l - \rho_b) \omega^2 f^3}{2\sigma} \quad (3.2)$$

With conditions of :

$$\begin{cases} f = 0 & \text{at } Z = l \\ f' = 0 & \text{at } Z = 0 \end{cases}$$

Then with integration of equation 3.2 :

$$(1+f'^2)^{-1/2} = \frac{(P_{0b} - P_{0l})f}{2\sigma} - \frac{(\rho_l - \rho_b)\omega^2 f^3}{8\sigma} \quad (3.3)$$

By knowing the maximum minor axis of the bubble a , and applying Laplace law this time at the tip of the bubble, the curvature at the tip of the bubble (on the axis) is $-\frac{(1+e)}{a}$ where e is the eccentricity of the deformed ellipsoidal bubble. Then we have:

$$\frac{1+e}{a} = \left(\frac{d}{df}(1+f'^2)^{-1/2}\right)_{f=0} = \frac{(P_{0g} - P_{0l})}{2\sigma} \quad (3.4)$$

Now with condition of $f' = 0$ at $f = a$ and combining 3.3 and 3.4:

$$\frac{e}{a^3} = \frac{\rho_l \omega^2}{8\sigma} \quad (3.5)$$

Therefore, the simplified differential equation will be;

$$(1+f'^2)^{-1/2} = (1+e)\frac{f}{a} - e\frac{f^3}{a^3} \quad (3.6)$$

From 3.6 the major axis (l) and volume of the bubble can be deduced as:

$$l = a \int_0^1 \frac{A}{(1-A^2)^{1/2}} dx, \quad V = 2\pi a^3 \int_0^1 \frac{x^2 A}{(1-A^2)^{1/2}} dx \quad (3.7)$$

where $A = x(1+e-ex^2)$. On the one hand by replacing a with $D/2$ (the notation used in our experimental data) in 3.5, the following relation for e is obtained:

$$\frac{e}{D^3} = \frac{(\rho_l - \rho_g)\omega^2}{8\sigma} \longrightarrow e = \frac{\rho_l \omega^2 D^3}{8\sigma} \longrightarrow \boxed{e = \frac{We}{8}} \quad (3.8)$$

On the other hand from equation 3.6, the aspect ratio X can be written as $X = \frac{L}{D} = \int_0^1 \frac{A}{(1-A^2)^{1/2}} dx$. Then rewriting equation 3.7 with equation 3.8 as a function of the Weber number, and noting \tilde{r} the dimensionless distance to the axis $\tilde{r} = 2r/D$, we obtain:

$$X = \int_0^1 \frac{\tilde{r}(1 + (1 - \tilde{r}^2)We/8)}{(1 - \tilde{r}^2(1 + (1 - \tilde{r}^2)We/8)^2)^{1/2}} d\tilde{r} \quad (3.9)$$

This equation predicts that the aspect ratio X is a sole function of the Weber number. Figure 3.10 shows the experimental data of figure 3.6, replotted as a function of the Weber number (same legend as figure 3.6). The solid line corresponds to the prediction of equation 3.9.

The aspect ratio of the different series in Figure 3.6 are regrouped along a same

curve in the (X, We) plane. However, the experimental aspect ratios are larger than the predicted one, and the relative departure to the prediction decreases when Weber is increased. This is directly related to the position of the bubble: the model assumes that the bubble center lies on the axis of rotation, but in the experiment buoyancy causes the bubble center to be at a finite distance r_e from this axis: the value of r_e decreases (see figure 3.1) when Weber is increased, due to the steeper pressure gradient at larger rotational velocities, which explains the trend observed on figure 3.10.

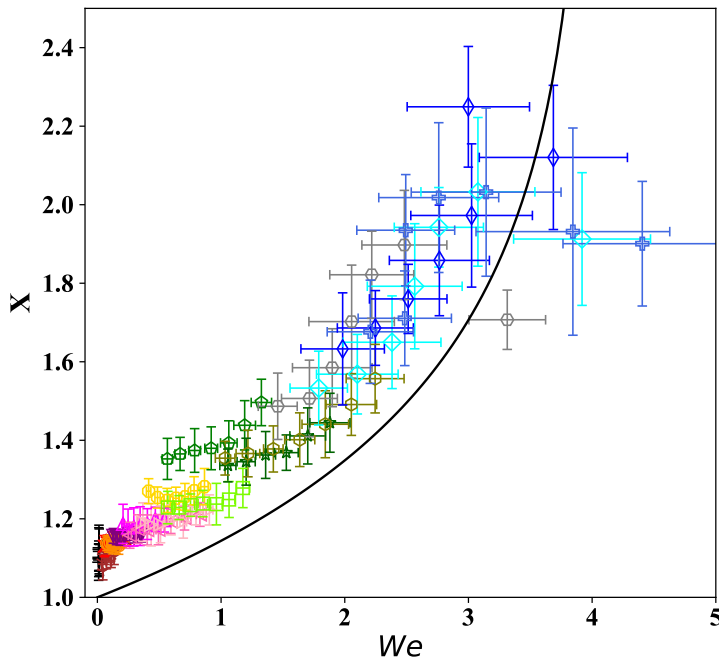


Figure 3.10: Bubble aspect ratio as a function of Weber number. Same as in Figure 3.6. The solid line corresponds to the model of Rosenthal 1962.

When the bubble is centered, the pressure difference between the bubble periphery and axis due to the parabolic pressure field is

$$\Delta P_0 = \rho_l \omega^2 D^2 / 8$$

The fact that the bubble is shifted away from the axis of the cell at a finite r_e

means that the pressure difference it is submitted to will be larger than if it were centered on the axis. The minimum pressure exerted on the bubble will still be the pressure at the axis of the cell if $Ro < 0.5$, which is the case for most of our data except for smaller bubbles, but the average pressure around the periphery will be larger because of the convexity of the pressure profile in the solid body rotational flow. It is easy to show by integration that the pressure difference between the mean pressure at the periphery of the bubble and pressure on the axis of the rotating cell, for a bubble of diameter D whose center is displaced at a distance r_e from the axis will be given by:

$$\Delta P = \Delta P_0(1 + 4r_e^2/D^2) = \Delta P_0(1 + 4Ro^2)$$

see figure 3.11. This result can be rapidly recovered by just considering the mean pressure over the diameter represented by the dashed line on figure 3.11:

$$\Delta P = \frac{P^+ + P^-}{2} - P_{axis} = \frac{1}{4}\rho_l\omega^2\left(\left(r_e + \frac{D}{2}\right)^2 + \left(r_e - \frac{D}{2}\right)^2\right) = \frac{1}{8}\rho_l\omega^2D^2\left(1 + \frac{4r_e^2}{D^2}\right)$$

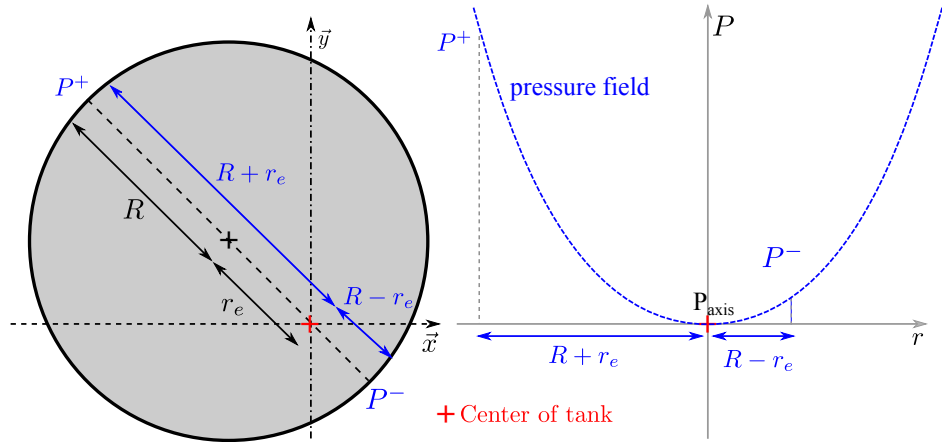


Figure 3.11: Sketch of the bubble of radius R , illustrating pressures P^+ and P^- at the surface of the bubble and their corresponding values on the parabolic pressure field in the tank. For a bubble shifted of a distance r_e from the tank axis, the pressure difference between mean pressure at periphery and pressure on axis of the cell is $\Delta P = \frac{P^+ + P^-}{2} - P_{axis}$.

Because of this shift off the axis, the bubble is obviously not axisymmetric anymore, as supposed in the model of Rosenthal 1962, and finding a generalization of equation 3.9 for the non axisymmetric problem appears difficult. We propose to avoid this difficulty by considering that the displaced bubble is equivalent to a centered bubble rotating at a larger ω' such that

$$\omega' = \omega(1 + 4r_e^2/D^2)^{1/2} = \omega(1 + 4Ro^2)^{1/2}$$

i.e. one which generates the actual pressure difference ΔP instead of ΔP_0 . This is equivalent to introducing a modified Weber number,

$$\begin{aligned} & \underbrace{We = \rho_l \omega^2 D^3 / 8\sigma}_{\text{bubble aligned with axis of rotation Rosenthal 1962 3.10}} \\ & \quad \downarrow \\ & We' = \underbrace{\frac{\rho_l D^3 \omega^2 (1 + 4Ro^2)}{8\sigma}}_{\text{Bubble shifted from axis}} \\ & \quad \downarrow \\ & We' = \rho_l \omega'^2 D^3 / 8\sigma = We(1 + 4Ro^2) \end{aligned}$$

Based on the results of figure 3.2, we estimate that $Ro \approx g/(D\omega^2)$, which yields,

$$We' = We(1 + 4g^2/(D^2\omega^4))$$

We plot on figure 3.12 the aspect ratio X as a function of this modified Weber number: even though there is still a slight underestimation of the aspect ratio for small bubbles, this improved model predicts relatively accurately the aspect ratio, in spite of the strong assumptions made on the shape of the bubble. The correction introduced in the Weber number captures correctly how buoyancy drives bubbles away from the axis of the cell at a finite r_e , and therefore exposes them to a steeper pressure gradient than the one they would experience if they

were centered. The discrepancy observed for the very small bubbles may be related to the impact of the mean velocity $r_e\omega$ on the shape of the bubble: for the small bubbles, the Weber number $We_{r_e} = 4WeRo^2$ built with the mean flow seen by the bubble is larger than the Weber number introduced in section 2.4, which points to a possible distinct origin of the deformation for this case.

The data for the larger bubbles show a non monotonic behavior for the largest Weber numbers (a behavior already present on figure 3.10): the decrease of the aspect ratio at the larger We is correlated to a very strong increase in the fluctuations around the mean aspect ratio, as shown by the larger error bars for these points. These shape fluctuations, which will be discussed in the following section 3.3, are in addition associated with a strong increase in the fluctuations of the distance to the axis r_e . A simple model based on the mean values of these quantities is probably not sufficient to capture the bubble shape for these non-stationary conditions.

A further explanation for the underestimation of the aspect ratio X at large We could reside in the method used for the determination of D , mean diameter in the cross section: we determine D from front view projections, but for strongly distorted bubbles at large We the size of this projection is certainly larger than the local D at a given longitudinal position z . This will lead to an underestimation of X for strongly distorted bubbles.

3.3 Break-up

As it has been already mentioned, by increasing ω , the longitudinal aspect ratio of the bubble (X) rises. This stretching of the bubble leads to rupturing for volumes larger than $V = 0.27 \text{ cm}^3$. Indeed, two types of break-up have been observed during the experiments in this type of flow. One is the situation where the bubble splits into two bubbles from the middle. For this type of break-up, regarding the figure 3.13 the aspect ratio (X) of the bubble with volume $V = 0.3 \text{ cm}^3$ at $\omega = 89 \text{ rad s}^{-1}$ fluctuates in time interval $[0, 4.5]$ seconds. After $T = 4.5 \text{ s}$ the bubble becomes distorted and experiences its highest value of X almost up to 5 (two times the average value until $T = 4.5 \text{ s}$). Afterwards, rupturing occurs and the bubble splits into nearly two same size bubbles (figure 3.14). We call this configuration of the bubble rupturing (figure 3.14) *middle* break-up.

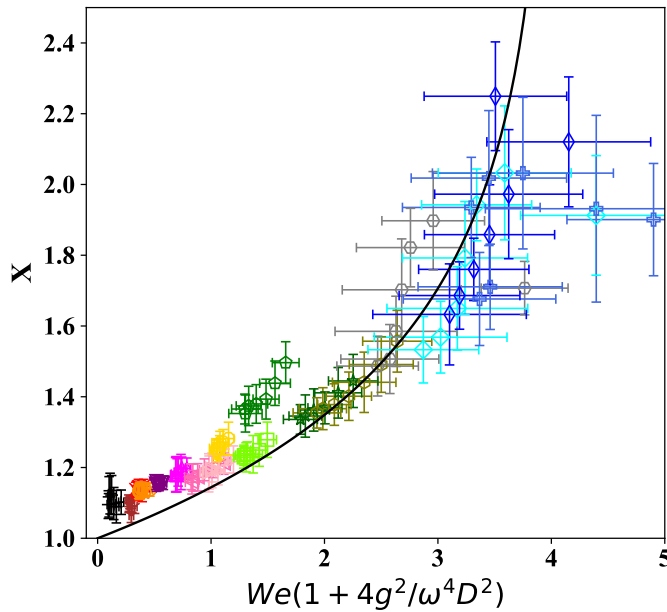


Figure 3.12: Bubble aspect ratio as a function of corrected Weber number. The legend is the same as in Figure 3.6. The solid line corresponds to equation 3.9, but integrated with the modified Weber number $We' = We(1 + 4g^2/(\omega^4 D^4))$.

Another type of bubble break-up has been observed. In this case the bubble breaks into two unequal size bubbles (figure 3.15). As a matter of fact, the longitudinal bubble aspect ratio (X) increases and reaches a peak, but it does not rupture. Then, the aspect ratio decreases and the break-up occurs (see figure 3.16). Figure 3.17 illustrates the broken bubbles in volume range of $[0.34, 0.41] \text{ cm}^3$. We observe that the bubble breaks above a given ω and the circle indicates the ω for which break-up occurs for each volume of the bubble. This means that there is a maximum beyond which the bubble breaks. The smallest bubble ruptures at $\omega \simeq 89 \text{ rad s}^{-1}$ and the largest ones break between $\omega \simeq 68 \text{ rad s}^{-1}$ and $\omega \simeq 74 \text{ rad s}^{-1}$.

As illustrated in figures 3.16 as well as 3.13, the bubble in a specific value of the ω for which it breaks, has a huge distortion as can be seen from the large values of the longitudinal aspect ratio X . Rosenthal 1962 predicted that for an ω lower

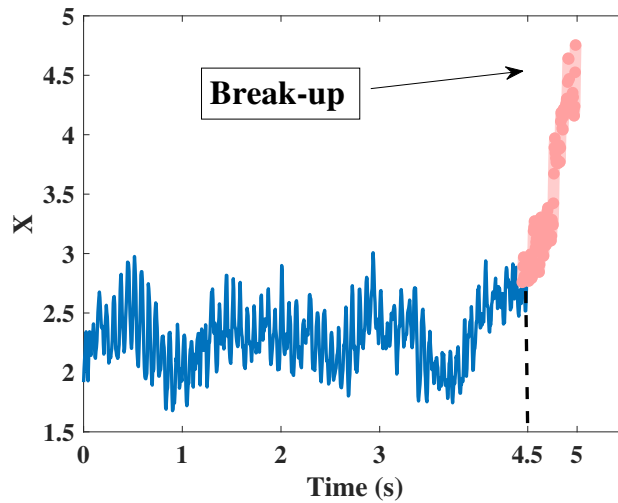


Figure 3.13: Aspect ratio X as a function of time (s) for the bubble $V = 0.3 \text{ cm}^3$ in $\omega = 89 \text{ rad s}^{-1}$. The red highlighted part of the graph is when the bubble is distorted and the value X sharply rises and then break-up of the bubble occurs.

than a specific value, the pressure gradient is not large enough to stabilize the bubble. So, the bubble becomes unstable. By verifying Rosenthal 1962 criterion for the instability of the bubble, in our case break-up is above the threshold and our bubbles are always in stable situation which is contrary to the experimental observation (see figure 3.18). In fact, the break-up we observe might be caused by a periodic forcing upon the bubble at the correct frequency through a mechanism of resonance on the interface, where the eigenfrequency of the stretched bubble is equal to the tank frequency (ω).

The interface of the elongated bubble along the axis of rotation can experience a series of eigenmodes. The results of Rayleigh shows (Risso 2000) that the frequency of an oscillating spherical bubble of radius R is:

$$\omega_n = \sqrt{\frac{(n-1)(n+1)(n+2)}{\rho_l} \frac{\sigma}{R^3}}$$

where n is characterizing the mode of oscillation of the bubble. By assuming that the bubble is entirely centered and using equation 3.6 (Rosenthal 1962), the

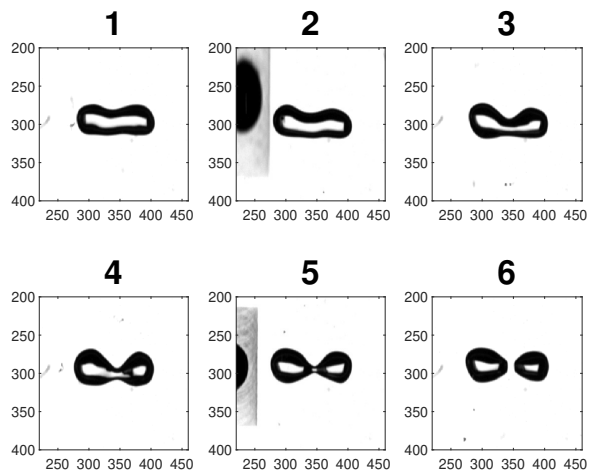


Figure 3.14: Six consecutive frames of the bubble before break-up moment showing how the bubble splits into two nearly equal size bubbles.

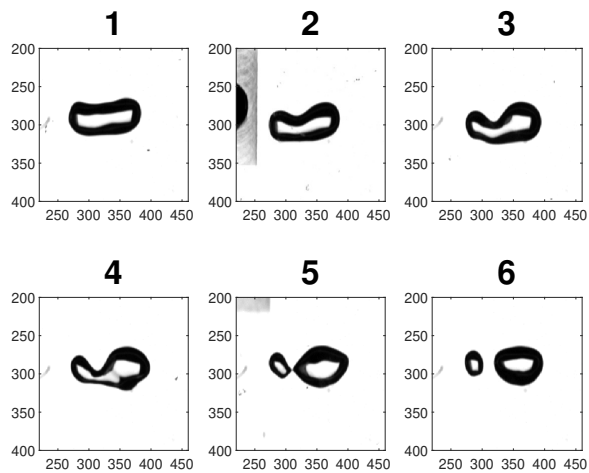


Figure 3.15: Six consecutive frames of the bubble before break-up moment showing how the bubble splits into a tiny and a large bubble.

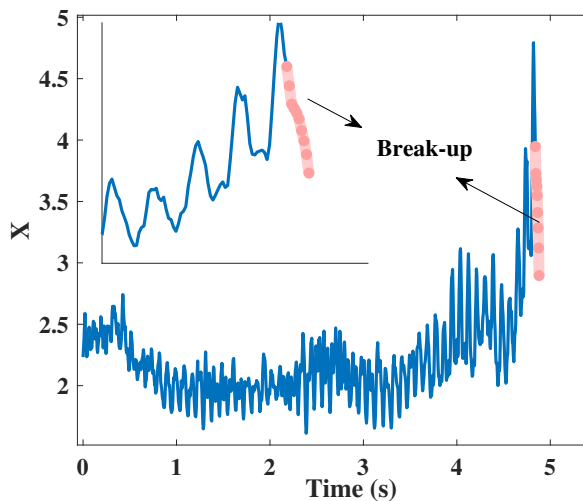


Figure 3.16: Six consecutive frames of the bubble before break-up moment showing the split bubble into a tiny and large bubble.

theoretical value of ω_n for diverse volume sizes of the broken bubble can be measured in various interface shape modes ($n = 2, 3, 4$). Figure 3.19 illustrates the variations of the eigenfrequencies of a bubble of volume $V \approx 0.35 \text{ cm}^3$: these frequencies decrease as a function of ω when omega is increased, due to the stretching of the bubble. This figure shows that a coincidence of the frequency of the tank (red line) with the frequency of the bubble occurs for modes $n = 2$ and 3. On the other hand, images of the bubble at the moment of break-up (figures 3.14, 3.16) confirm that the shape mode of the bubble is probably in configuration of $n = 2$. This theoretical prediction is approximately consistent with the experimental data. For instance, for the bubble ($V \approx 0.35 \text{ cm}^3$) break-up occurs at $\omega \approx 73 \text{ rad s}^{-1}$, but the theoretical prediction in figure 3.19 shows the intersection of the ω_{cell} and calculated eigenfrequency of the bubble (ω_0) in shape mode $n = 2$ happened at $\omega = 66 \text{ rad s}^{-1}$ (rotational velocity of the break-up moment). There is a small difference between the ω of break-up during the experiment and the theoretical value of ω in which break-up occurred. Note that the eigenfrequency is estimated from that of a spherical bubble, but the bubble is actually close to a prolate ellipsoid. However, the model is still consistent with a resonance mechanism. Therefore, we can conclude that with respect to

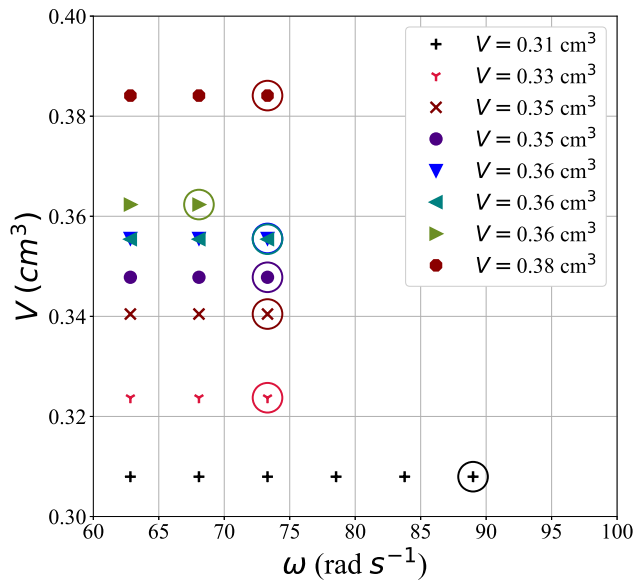


Figure 3.17: Volume as a function of ω for the bubbles which experienced break-up. The circles are marked for the ω of break-up.

figure 3.18, the bubble is supposed to be stable, but the resonance causes huge fluctuations leading to break-up.

Supposing that the shape mode of the bubble at the moment of break-up is at $n = 2$, the eigenfrequency of the stretched bubble is estimated as:

$$\omega_0 = \sqrt{\frac{96}{\rho_l} \frac{\sigma}{L^3}} \quad (3.10)$$

In addition, figure 3.20 left exhibits that the ratio ω/ω_0 at break-up is in a range between 1.7 and 2.1 independently from the size of the bubble and the rotational velocity of the tank. We observe that ω/ω_0 is of the order of 2, which seems a bit large. This could be caused by the large stretching of the bubble when resonance is approached, which leads to large values of L and hence lower values of ω_0 close to break-up. The particularity of the problem here is that the eigenfrequency of the bubble depends on the forcing itself, as is the case in parametric instabilities.

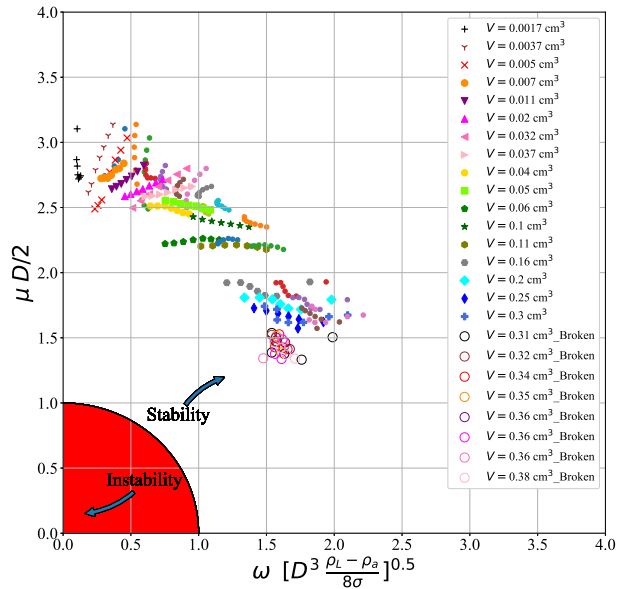


Figure 3.18: Stability criterion of the bubble aligned with the center of rotation proposed by Rosenthal 1962 for all the experimental data in demineralised water. Here μ is the wave number as $2\pi/\lambda$, where λ is the wavelength of the considered perturbation. We consider here a perturbation such that $\lambda = L/2$.

Note that this effect is not taken into account in figure 3.19, which is only based on the model for bubble size with the model of Rosenthal 1962, and not on the experimentally measured bubble size. Note also that as mentioned above the bubble is here a prolate ellipsoid of major axis L , and not a sphere of diameter L : the estimate of equation 3.10 is therefore probably smaller than the actual eigenfrequency of the prolate bubble, which may also explain the large ω/ω_0 ratios at break-up.

We also plot in figure 3.20 right the same graph, but with this time ω_0 estimated

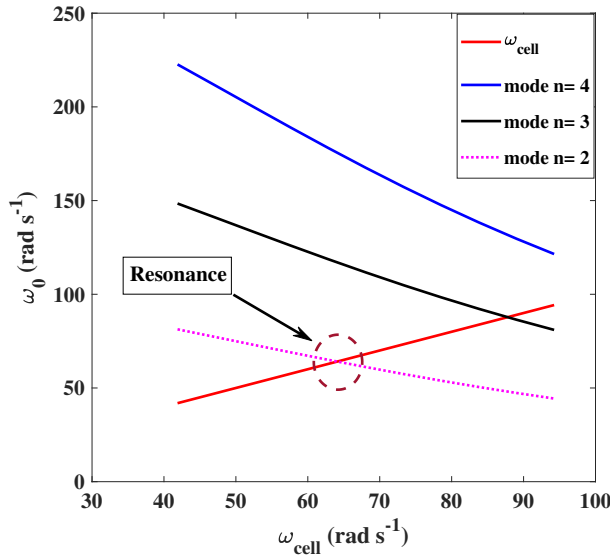


Figure 3.19: Eigenfrequencies of a bubble of $V \approx 0.35\text{cm}^3$ as a function of ω_{cell} . The red line is the rotational velocity of the tank (ω_{cell}). The dashed magenta line is the theoretical value of the oscillated bubble frequency at shape mode $n = 2$ (interface configuration of the bubble when break-up occurs). Black and blue line are the calculated frequency of the oscillated bubble in other shape modes $n = 3$ and 4. The marked point (break-up) is the moment that the frequency of the bubble coincides with the frequency of the tank at shape mode $n = 2$ ($\omega = 66\text{ rad s}^{-1}$).

from the (constant) characteristic size of the bubble R_{eq} as:

$$\omega_{0R} = \sqrt{\frac{12}{\rho_l} \frac{\sigma}{R_{eq}^3}}$$

Figure 3.20, right shows that the value ω/ω_{0R} for the all the series of volumes is in a range between 0.66 to 0.83. We will come back to this question of bubble break-up in chapter 5, where similar break-up experiments in the presence of surfactant are described.

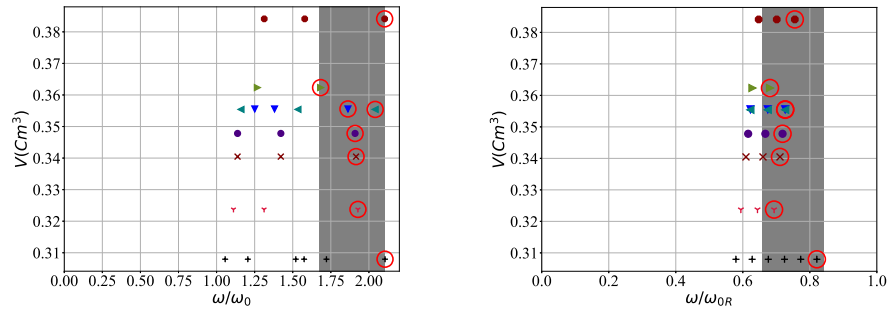


Figure 3.20: Volume of the broken bubble as a function of ratio ω/ω_0 (ratio between tank rotation frequency, and frequency of the stretched bubble ω_0) for all experimental series experiencing break-up. Circles identify the rotation speed ω for which rupturing occurred. Same legend as figure 3.17. **Left:** the value of $\omega_0 = \sqrt{\frac{96}{\rho} \frac{\sigma}{L^3}}$. **Right:**

$$\omega_{0R} = \sqrt{\frac{12}{\rho} \frac{\sigma}{Req^3}}.$$

4

Forces acting on the bubble

In this chapter our objective is to deduce the forces upon the bubble (drag and lift), based on measurements of the particle position. Previous studies for a spinning air bubble in water with a contaminated interface have been concerned with the values of C_L and C_D (lift and drag coefficient) as a function of Re and for large Ro (Rastello et al. 2009; Van Nierop et al. 2007), i.e. bubbles located far from the axis of rotation. In other words, forces upon much smaller bubbles, and for lower Re (see figure 4.1).

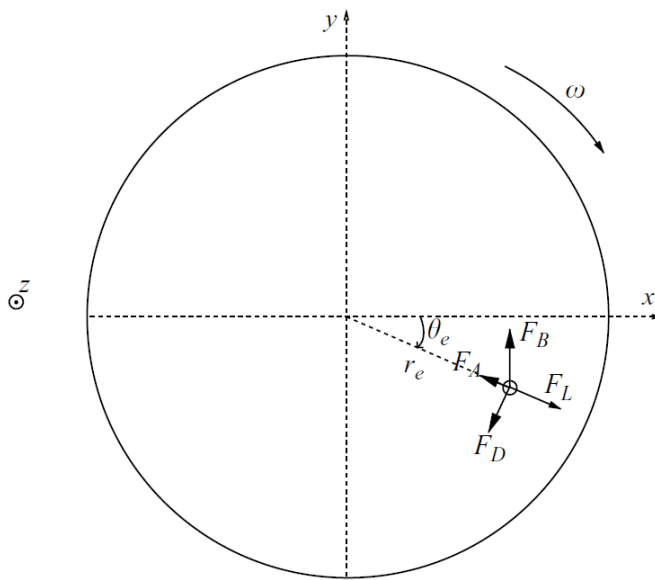


Figure 4.1: Acting forces upon the bubble at equilibrium position with $Ro \geq 6$, Rastello et al. 2009

4.1 Modeling of the forces

As it has already been mentioned, in the present work the bubbles move closer to the axis of rotation when ω is increased. Their average position is characterized by the distance r_e and the angle θ (see figure 2.35). The aim of this section is to deduce the forces acting on the bubble in the limit of large bubble sizes.

Following Magnaudet and Eames 2000, we assume that the force exerted by the liquid on the bubble can be written as a superposition of pressure gradient and added mass forces F_A , drag force F_D , lift force F_L , plus of course buoyancy F_B (figure 4.2), and write the equation of motion of the bubble of velocity \mathbf{v} as:

$$\rho V C_A \frac{d\mathbf{v}}{dt} = \rho V (C_A + 1) \frac{D\mathbf{U}}{Dt} + F_D + F_L - \rho V \mathbf{g} \quad (4.1)$$

where \mathbf{U} is the velocity of the undisturbed ambient flow taken at the center of the bubble. The lift and drag forces are defined as respectively the components of the fluid force in the directions parallel and perpendicular to the fluid velocity at the center of the bubble. The force due to the pressure field of the solid body rotating flow (i.e. isotropic normal stress, which is also exerted by the fluid) is in this expression separated from the lift/drag. The added mass force, corresponding to the inertia of the surrounding fluid, and which is also of course transmitted via the stress exerted by the fluid, is also separated from the lift and drag forces.

As illustrated in figure 2.31 we study relatively large ω such that the amplitude of oscillations around the bubble mean position remain small compared to the bubble size. We therefore neglect the variations of the velocity of the bubble, and the balance of forces on the bubble can be written (as in Rastello et al. 2009):

$$0 = V(C_A + 1) \frac{D\mathbf{U}}{Dt} + \frac{1}{2} C_D A_b |\mathbf{U}| \mathbf{U} + V C_L \mathbf{U} \times (\nabla \times \mathbf{U}) - V \mathbf{g} \quad (4.2)$$

where we have introduced the drag and lift coefficients C_D and C_L , and A_b which is the projection of the bubble area normal to the $\hat{\theta}$ direction. For an axisymmetric ellipsoidal bubble of axis L and D (figure 2.12), $A_b = \pi LD/4$. For small bubbles, the usual expression for the lift is:

$$F_L = \rho V C_L \mathbf{U} \times \mathbf{rot} \mathbf{U}$$

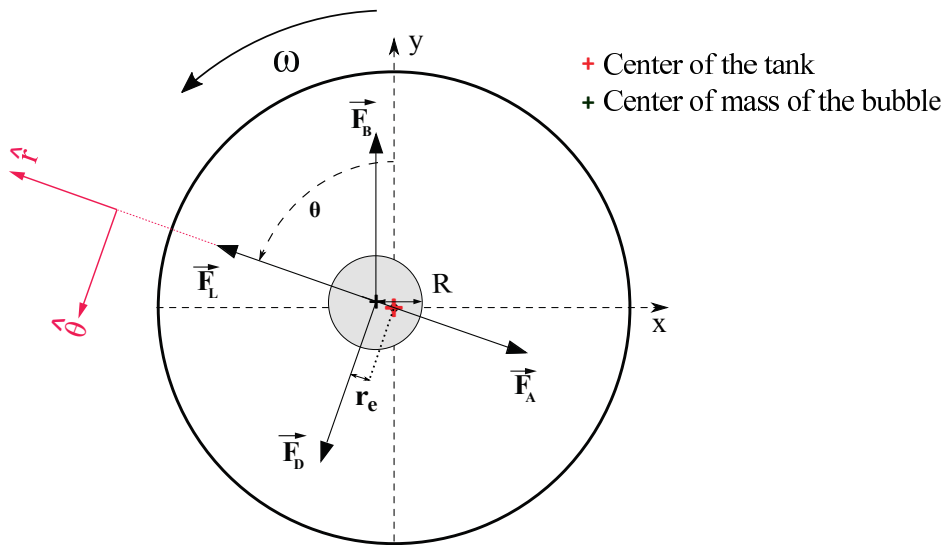


Figure 4.2: Bubble position in the cell cross-section: the center of the bubble is characterized by r_e and θ . The action of the liquid on the bubble is modelled as the sum of drag F_D , lift F_L , pressure and added mass contributions F_A .

here the base flow is a solid-body rotation, therefore, $\mathbf{rot}U = 2\omega\mathbf{z}$.
The lift force is then:

$$F_L = C_L 2\rho V \omega^2 r_e \hat{\mathbf{r}} \quad (4.3)$$

The added mass and pressure forces both scale with the pressure gradient caused by the base flow U :

$$F_{AM+P} = \rho V (C_A + 1) \frac{DU}{Dt} = -V (C_A + 1) \nabla P = -\rho V (C_A + 1) \omega^2 r_e \hat{\mathbf{r}} \quad (4.4)$$

This contribution is of the same form as the lift contribution. The added mass coefficient can be computed as a function of the shape of the bubble, as will be shown further.

The drag contribution can be written:

$$F_D = \rho C_D A_b \frac{1}{2} U(r_e)^2 \hat{\theta} = \rho C_D A_b \frac{1}{2} r_e^2 \omega^2 \hat{\theta} \quad (4.5)$$

By projections of equation (4.2) along \hat{r} and $\hat{\theta}$:

$$\longrightarrow \boxed{\hat{r} : F_B \cos\theta + F_L - F_A = 0}$$

↓

$$g \cos\theta + 2C_L \omega^2 r_e - (C_A + 1) \omega^2 r_e = 0$$

↓

$$(C_A + 1) - 2C_L = \frac{g \cos\theta}{\omega^2 r_e} = \frac{1}{F_r} \cos\theta$$

$$\longrightarrow \boxed{\hat{\theta} : -Vg \sin\theta + \frac{1}{2} \rho C_D A_b r_e^2 \omega^2}$$

↓

By recalling $\alpha = V/(LD^2)$ and $\beta = A_b/(LD)$

↓

$$\frac{C_D}{2} = \frac{Vg}{A_b r_e^2 \omega^2} \sin\theta = \frac{\alpha}{R_o F_r \beta} \sin\theta$$

From the projections of equation (4.2) along \hat{r} and $\hat{\theta}$

$$\begin{cases} (C_A + 1) - 2C_L = \frac{g}{r_e \omega^2} \cos \theta = \frac{1}{Fr} \cos \theta & (4.6a) \\ \frac{C_D}{2} = \frac{Vg}{A_b r_e^2 \omega^2} \sin \theta = \frac{\alpha}{Ro Fr \beta} \sin \theta & (4.6b) \end{cases}$$

This system shows that C_L is a function of r_e via the Froude number Fr , and also of θ and X via the added mass coefficient. The drag coefficient is a function of Fr , θ , Ro , $\alpha = V/(LD^2)$ and $\beta = \frac{A_b}{LD}$: we recall that the latter dimensionless number is, similar to α , a number characterizing the shape of the bubble: $\beta = \pi/4$ for an ellipsoid and $\beta = 1$ for a cylinder (discussed in chapter 3).

In order to simplify the discussion and regarding to chapter 3, we assume in the following that α remains close to its value for an ellipsoid, i.e. $\pi/6$ for all our conditions. Similarly, and in order to be consistent with this choice, we assume $\beta = \pi/4$. This assumption may lead to a slight underestimation of the drag coefficient at large ω , of at most 10%. We then use system (4.6) to deduce C_L and C_D from the measurements of the bubble average position and shape. Note that previous studies for air bubbles in water have been concerned with the values of C_L and C_D as a function of Re and for large Ro (Rastello et al. 2009; Van Nierop et al. 2007). The main difference for the large bubbles considered here is that we will consider low Ro , down to $Ro \approx 0.15$, when the bubble is close to the center of the rotating cell.

As mentioned above, α and β are almost constant for the conditions of our experiments. We will show in the following sections that C_L and C_D are not significantly impacted by X and We , and can be predicted as a function of Re and Ro only. We illustrate in figure 4.3 the values of Re and Ro for all the measurements presented here.

4.2 Drag coefficient

We plot in figure 4.4 the drag coefficient, deduced from equation (4.6b) via measurements of the mean values of r_e and θ , as a function of Re . The red solid line indicates the prediction of Schiller and Naumann 1933 for a solid sphere in a

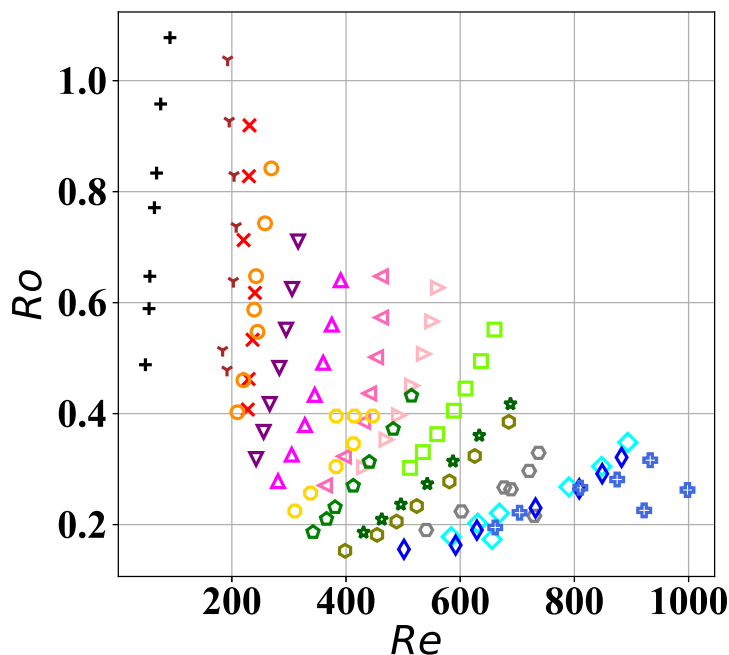


Figure 4.3: Cartography of the conditions covered by the present experiments in the $Re - Ro$ plane. Same legend as in Figure 3.6.

uniform flow. We have included in this graph the results of an additional measurement for a smaller bubble (gray asterisk, $V = 0.50 \text{ mm}^3$, $Re_q = 0.5 \text{ mm}$). For this particular bubble, ω is varied between 10 s^{-1} and 30 s^{-1} , and Ro varies between respectively 10 and 3 in this interval, i.e. this bubble remains relatively far from the cell axis. We recover in this particular case previous results also obtained with demineralised water (Rastello et al. 2009; Rastello et al. 2017): the points of this series fall close to the curve for solid spherical particles due to the inevitable presence of contaminants on the bubble interface. On the contrary, for larger bubbles closer to the cell center, and which for most of them straddle the axis of rotation ($Ro < 0.5$, see figure 4.3), we measure much larger drag coefficients, reaching values of up to 10. In addition, the scatter of the different series shows a strong influence of Ro on C_D : for a given Re , C_D is larger for a larger bubble, i.e. for smaller Ro . The large values of C_D (up to 8 and 10) show that expression

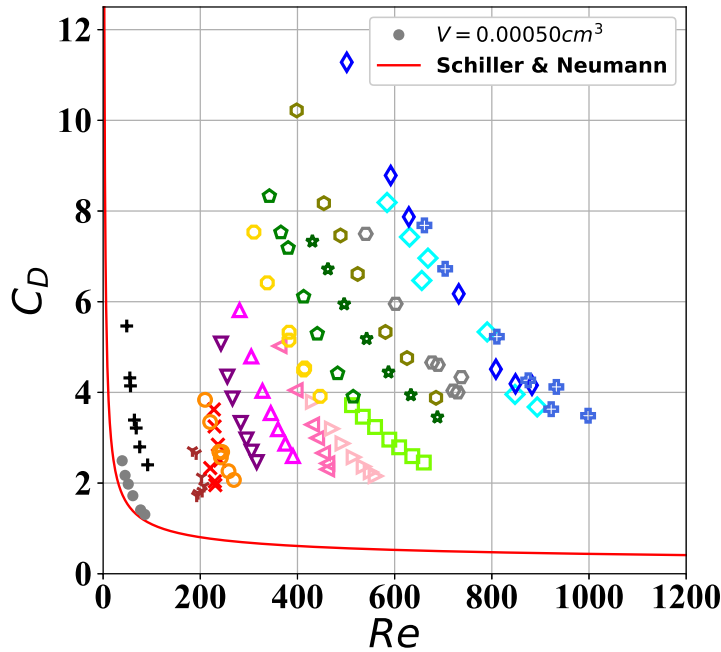


Figure 4.4: Drag coefficient C_D as a function of Re .

(4.5) does not capture correctly the order of magnitude of the drag force at low Ro .

A spinning wake is expected to envelop the bubble at this low Ro , and therefore the configuration is different from that at large Ro where different orders of magnitude of the fluid force are expected to coexist perpendicular or along the wake direction (namely equations 4.3 and 4.5). It seems reasonable to expect that in the present vortex-like low Ro limit, both lift and drag will be of similar orders of magnitude.

In order to model the impact of Ro , we account for the fact that the bubble is placed in a rotating flow, whose direction is changing on a scale much smaller than the bubble scale itself at low Ro . The shear Reynolds number $Re_{shear} = Re/Ro$ is large, in the range [500-5000] for most conditions, and wakes will therefore develop around the bubble.

Another way to put it, is to consider that the drag caused by the spinning wake around the bubble will be dominated by the dynamic pressure difference around the bubble: the order of magnitude of this difference is the difference between the (maximum) dynamic pressure at the point farthest from the origin and the (minimum) dynamic pressure at the point closest to the origin (see P^+ and P^- in figure 3.11), namely:

$$\Delta P_d \approx P^+ - P^- = \frac{1}{2}(\rho\omega^2(R + r_e)^2 - \rho\omega^2(R - r_e)^2) = 2\rho\omega^2 R r_e \quad (4.7)$$

instead of $\rho U(r_e)^2/2$ for the uniform flow limit. Instead of the classical form of the drag force in uniform flow (4.5), the proposed expression for the drag force is then:

$$F_D = C_{D\Delta} A_b \rho \omega^2 D r_e \hat{\theta} \quad (4.8)$$

where we have introduced a new drag coefficient:

$$C_{D\Delta} = C_D R o / 2$$

Note again that the order of magnitude introduced by equation (4.8) is larger than that of equation (4.5), since r_e is smaller than R for almost all our conditions (low Ro limit). The scaling law for the drag force is then similar to that introduced for the other forces exerted by the fluid (added mass, pressure and lift force), in equation (4.3).

We plot in figure 4.5 the variations of $C_{D\Delta}$ as a function of Re_{shear} . The values of $C_{D\Delta}$ are mostly in the range [0.6 - 0.9] which shows that the chosen definition captures the correct order of magnitude of the drag force. In addition, the data of figure 4.4 appears much better collapsed: for Re_{shear} varying in the range [500-4000] we find an approximately constant $C_{D\Delta}$ with $C_{D\Delta} \approx 0.75$. This means that the classical drag coefficient can be estimated as $C_D \approx 2C_{D\Delta}/Ro \approx 1.5/Ro$ at low Ro . An even simpler estimate for C_D can then be built from this expression, by further assuming that $r_e \approx g/\omega^2$ (valid for all series except the smaller

$V = 0.69 \text{ mm}^3$ bubble, see figure 3.2), which yields $C_D \approx 1.5D\omega^2/g$. We plot in figure 4.6 the measured C_D as a function of this simple prediction: the proposed expression manages to provide a relatively good estimate of the drag coefficient for the large range of conditions we investigate here. We believe the larger dispersion observed for large bubbles and large rotation rates is caused by larger fluctuations for these conditions. These fluctuations are probably due to the fact that ω becomes closer to ω_0 for these conditions (see section 3.3).

We have defined the standard deviation (error bars) of $C_{D\Delta}$ and C_D in figure 4.5 and 4.6 as:

$$dC_{D\Delta} = \sqrt{\left| \frac{\partial C_{D\Delta}}{\partial C_D} dC_D \right|^2 + \left| \frac{\partial C_{D\Delta}}{\partial R_o} dR_o \right|^2}$$

$$dC_D = \sqrt{\left| \frac{\partial C_D}{\partial D} dD \right|^2 + \left| \frac{\partial C_D}{\partial r_e} dr_e \right|^2 + \left| \frac{\partial C_D}{\partial \theta} d\theta \right|^2}$$

The data for the smaller bubble (black cross points) show much larger values of the drag coefficient $C_{D\Delta}$ in figure 4.5. This results from the fact that the measured $r_e\omega^2/g$ for this series of points is smaller than for the other bubbles investigated, as mentioned above (figure 3.2). Indeed, for such a small bubble ($V = 0.69 \text{ mm}^3$, $R_{eq} = 0.55 \text{ mm}$), the values of Re are significantly smaller: the reasoning behind the expression of equation (4.8) is not expected to be valid.

Finally, we come back to the issue of the a priori surprising relevance of the simplified force balance presented in section 3.1, namely "buoyancy = pressure gradient", which correctly predicts $r_e \approx g/\omega^2$ (figure 3.2). The fact that $C_{D\Delta}$ is constant for the data presented here implies that the drag force actually scales similarly as the pressure gradient itself: buoyancy is actually mostly balanced by drag, and not pressure gradient, and this explains the relevance of the simple $r_e \sim g/\omega^2$ scaling.

4.3 Lift

We can measure the lift coefficient through the value of $2C_L - C_A$, obtained from equation (4.6a) as:

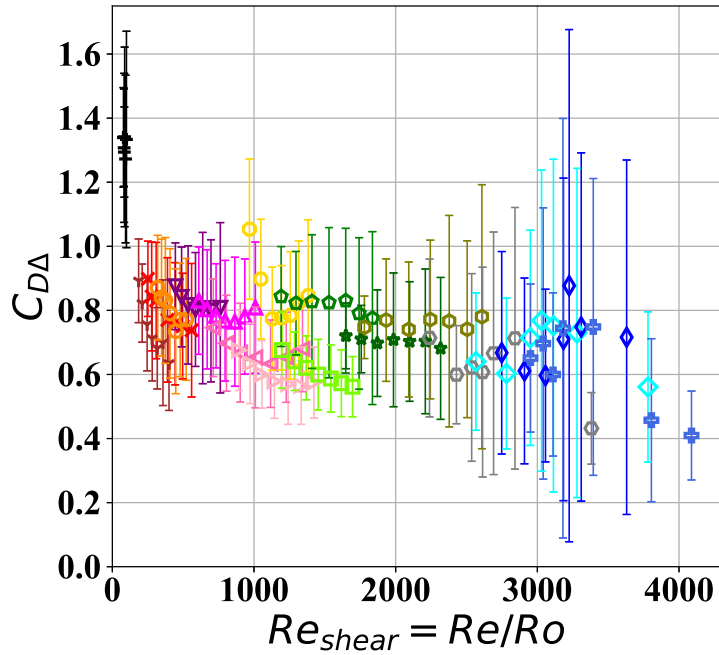


Figure 4.5: Drag coefficient C_{DA} as a function of the shear Reynolds number Re_{shear} .

$$2C_L - C_A = 1 - \frac{g}{r_e \omega^2} \cos\theta$$

We show the variations of $2C_L - C_A$ as a function of Re_e in figure 4.7. In order to isolate the lift coefficient, and compare it to the results of the literature, we need to estimate the added mass coefficient. This coefficient can be computed analytically based on the measured shape of the bubble, provided the bubbles are assumed to be ellipsoidal. As mentioned above, the model of Rosenthal 1962 predicts a small departure from the ellipsoidal shape, but this is assumed to be negligible here given the moderate deformation of the bubbles (coefficient α expected to increase from 0.52 to at most 0.56). The stretching of aspect ratio X along the axis of the cell, which has been discussed in chapter 3, tends to increase the value of the added mass coefficient along the \hat{r} direction. However, the bubbles also tend to flatten slightly along $\hat{\theta}$ due to the rotational

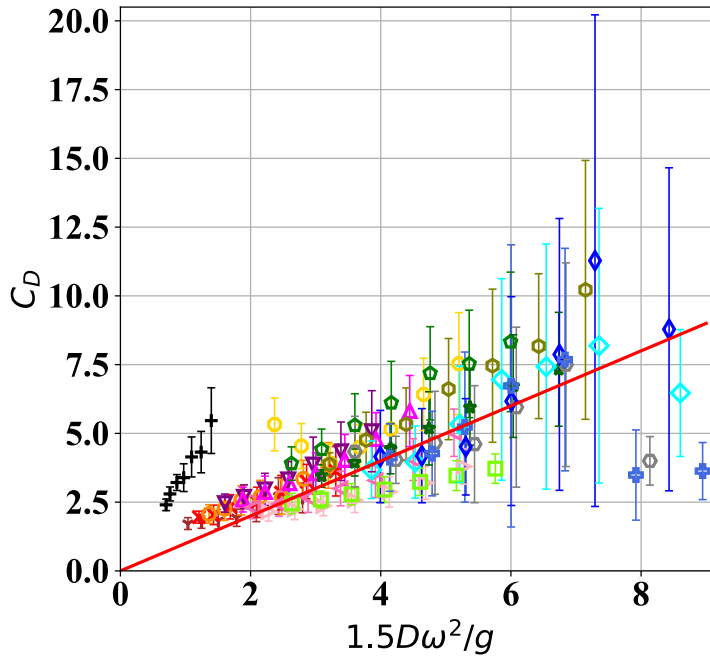


Figure 4.6: Drag coefficient measured from bubble position, plotted as a function of proposed simplified model $1.5D\omega^2/g$; this prediction provides a good estimate of C_D for the large range of conditions investigated here.

flow when Ro is not too small (figure 2.33-left), and are therefore not strictly axisymmetric. The aspect ratio in the $(\hat{r}, \hat{\theta})$ plane can reach values up to 1.4 (figure 3.7) for the largest bubbles and largest values of We_{re} , Weber number based on the mean velocity $r_e\omega$: this flattening, even at moderate aspect ratios, is expected to decrease the added mass coefficient along \hat{r} compared with the axisymmetric assumption. We chose here to compute C_A numerically from the mean bubble dimensions deduced from the visualizations: we assume that the bubbles are ellipsoidal, and integrate the expressions proposed by Lamb 1993 as detailed in the following subsection.

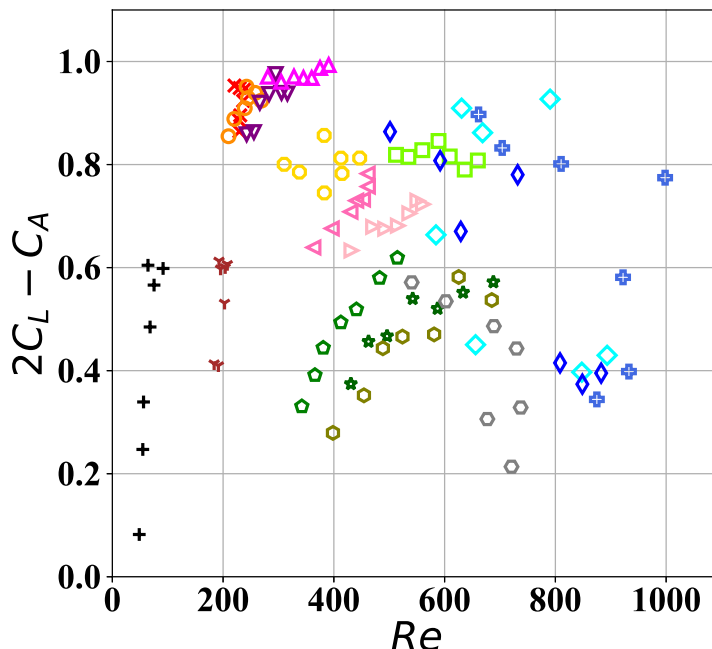


Figure 4.7: Variations of $2C_L - C_A$ as a function of Re , from equation (4.6a).

4.3.1 Variations of the added mass coefficient (C_A)

The added mass coefficients of an ellipsoid moving in an infinite fluid can be found in Lamb 1993. They are obtained by calculating the motion of a liquid, at rest at infinity, produced by the translation of a solid ellipsoid through it. The ellipsoid is characterized by the half lengths a, b, c (figure 2.28) of its principal axes. We suppose that the half length c is aligned with the axis of rotation of the cell z , and that directions a and b make an angle γ with \hat{r} and $\hat{\theta}$ respectively (see figure 4.8).

We wish here to calculate the added mass coefficient relevant for equation (4.6a) which is the added mass coefficient along \hat{r} . This coefficient, which is simply noted C_A in the rest of our calculations, will be noted more precisely C_{Ar} in this section to avoid any ambiguity. The solution of motion with the use of special orthogonal curvilinear coordinates yields for added mass coefficients along axes

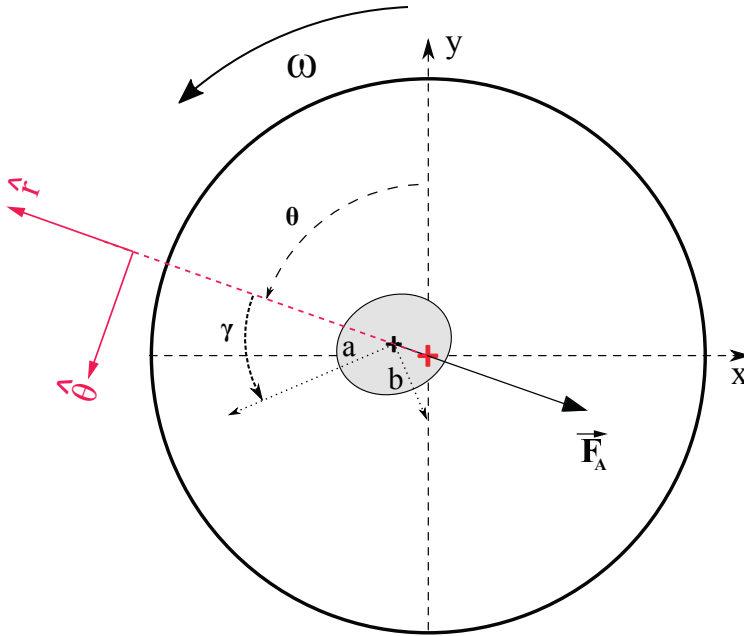


Figure 4.8: Sketch showing the cross section for an ellipsoidal bubble inclined of an angle γ relative to the cylindrical frame.

a and b :

$$C_{Aa} = \frac{\alpha_0}{2 - \alpha_0} \text{ where } \alpha_0 = abc \int_0^\infty \frac{d\lambda}{(a^2 + \lambda)\Delta} \quad (4.9)$$

$$C_{Ab} = \frac{\beta_0}{2 - \beta_0} \text{ where } \beta_0 = abc \int_0^\infty \frac{d\lambda}{(b^2 + \lambda)\Delta}$$

with $\Delta = ((a^2 + \lambda)(b^2 + \lambda)(c^2 + \lambda))^{\frac{1}{2}}$.

If we assume that the bubble is axisymmetric with $a = b = D/2$ in the $r - \theta$ plane, and stretched by pressure effects along z (with therefore $c > a = b$), coefficient α_0 and β_0 are equal and can be expressed as a function of the aspect ratio $X = L/D = c/a$:

$$\alpha_0 = \beta_0 = X \int_0^\infty \frac{d\lambda}{(1 + \lambda)\Delta_X} \quad (4.10)$$

where $\Delta_X = (1 + \lambda)(X^2 + \lambda)^{\frac{1}{2}}$. Values of X larger than one (corresponding to prolate ellipsoids) yield added mass coefficients $C_{Ar} = C_{Aa} = C_{Ab}$ larger than 0.5, since the stretching along z tends to increase inertia in the radial direction.

If we now drop the axisymmetric assumption, we are in a situation where a priori $c > a > b$. Let the two aspect ratio be $X = c/b$ and $X_F = a/b$. Coefficients α_0 and β_0 are given by:

$$\alpha_0 = XX_F \int_0^\infty \frac{d\lambda}{(X_F^2 + \lambda)\Delta'} \quad \text{and} \quad \beta_0 = XX_F \int_0^\infty \frac{d\lambda}{(1 + \lambda)\Delta'} \quad (4.11)$$

with $\Delta' = ((X_F^2 + \lambda)(X^2 + \lambda)(1 + \lambda))^{\frac{1}{2}}$.

Therefore, the values of C_{Aa} and C_{Ab} can be calculated from system 4.9. However, for computing C_{Ar} first we need to account for the orientation of the bubble. Then we write the general form of the added mass of an object imposing an inertia to the multiple phase flow system:

$$C_A \frac{d\mathbf{u}}{dt} = \mathbf{F}$$

We know that in the basis of the ellipsoidal bubble (a,b,c) this matrix is diagonal:

$$\underbrace{\begin{bmatrix} C_{Aa} & 0 & 0 \\ 0 & C_{Ab} & 0 \\ 0 & 0 & C_{Ac} \end{bmatrix}}_{\text{Added mass } C_A} \frac{d\mathbf{u}}{dt} = \mathbf{F}$$

In addition, if we introduce the angle of the bubble with the x axis as O , we have $\gamma = \frac{\pi}{2} + O - \theta$. We now express matrix C_A in basis (r, θ) with the help of the rotation matrix R_θ as:

$$R_Y^T C_A R_Y = \begin{bmatrix} \cos\gamma & \sin\gamma & 0 \\ -\sin\gamma & \cos\gamma & 0 \\ 0 & 0 & 1 \end{bmatrix} \begin{bmatrix} C_{Aa}\cos\gamma & -C_{Aa}\sin\gamma & 0 \\ C_{Ab}\sin\gamma & C_{Ab}\cos\gamma & 0 \\ 0 & 0 & C_{Ac} \end{bmatrix}$$

$$R_Y^T C_A R_Y = \begin{bmatrix} \overbrace{C_{Aa}\cos^2\gamma + C_{Ab}\sin^2\gamma}^{C_{Ar}} & \cos\gamma \sin\gamma (C_{Ab} - C_{Aa}) & 0 \\ \overbrace{\cos\gamma \sin\gamma (C_{Ab} - C_{Aa})}^{C_{Ar\theta}} & C_{Aa}\sin^2\gamma + C_{Ab}\cos^2\gamma & 0 \\ 0 & 0 & C_{Ac} \end{bmatrix} \quad (4.12)$$

↓

Since here we have $\frac{d\mathbf{u}}{dt}$ parallel to \hat{r} , we are just interested in the first column of the matrix. Therefore, we have:

$$\boxed{C_{Ar} = C_A = C_{Aa}\cos^2\gamma + C_{Ab}\sin^2\gamma}$$

Regarding the matrix above, when $\gamma \neq 0$ and because of the non-diagonality of the added mass matrix, an additional added mass term ($C_{Ar\theta}$) should be introduced in 4.6b (projection along $\hat{\theta}$) and subsequently in the expression for the drag coefficient discussed in the previous section.

$$\frac{C_D}{2} = \underbrace{\frac{Vg}{A_b r_e^2 \omega^2} \sin\theta}_A - \underbrace{\frac{C_{Ar\theta} V}{A_b r_e}}_B \quad (4.13)$$

Figure 4.10, left shows that the value $C_{Ar\theta}$ varies between -0.05 up to 0.2 for all experimental data. Moreover, figure 4.9 illustrates that the drag coefficient

approximately holds the same value if we take into account the contribution of $C_{Ar\theta}$. Furthermore, figure 4.10, right justifies that the relative contribution of the non-diagonal added mass term (term B in equation 4.13) is small compared to the diagonal term (term A in equation 4.13) and reaches at most 0.22 for largest bubbles. This justifies that the contribution of $C_{Ar\theta}$ is small and we can neglect this value when the carrier flow inside the tank is demineralised water. We will detailedly discuss the effect of $C_{Ar\theta}$ in the presence of surfactant in chapter 5.

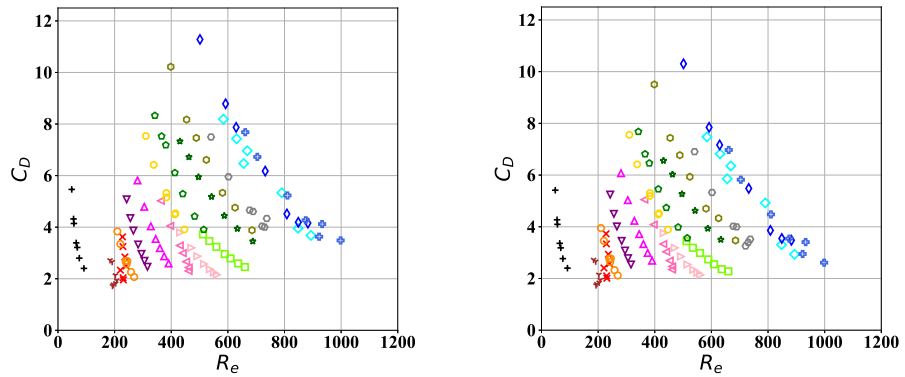


Figure 4.9: **Left:** Variations of the drag coefficient without consideration of $C_{Ar\theta}$ same figure as 4.4. **Right:** Same as figure left with consideration of $C_{Ar\theta}$ (term B in equation 4.13).

We show in figure 4.11 the variations of the added mass coefficient C_{Ar} as a function of Weber number We , which compares the pressure difference between periphery and axis to capillary pressure (see chapter 3): C_{Ar} increases with We , due to the increase in X when We is increased. The values of X_F , which also impacts C_{Ar} , are on the contrary expected to increase with

$$We_{re} = \rho(r_e\omega)^2R/\sigma = 4WeRo^2$$

, built with the mean velocity $r_e\omega$ seen by the bubble. As expected, the added mass C_{Ar} decreases when We_{re} is increased (figure 4.12) for a given series (i.e. given range of X).

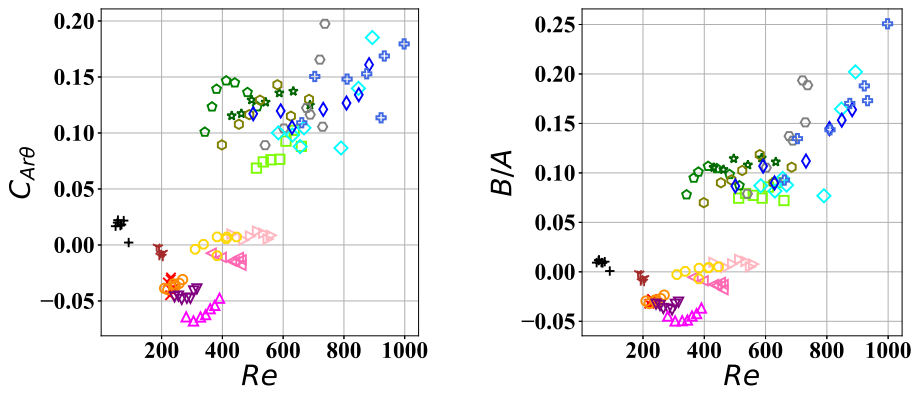


Figure 4.10: Left: Variations of $C_{Ar\theta}$ as a function of Re . Right: Ratio of the non-diagonal term B to diagonal term A in equation 4.13 to verify the effect of $C_{Ar\theta}$ in our drag coefficient measurement.

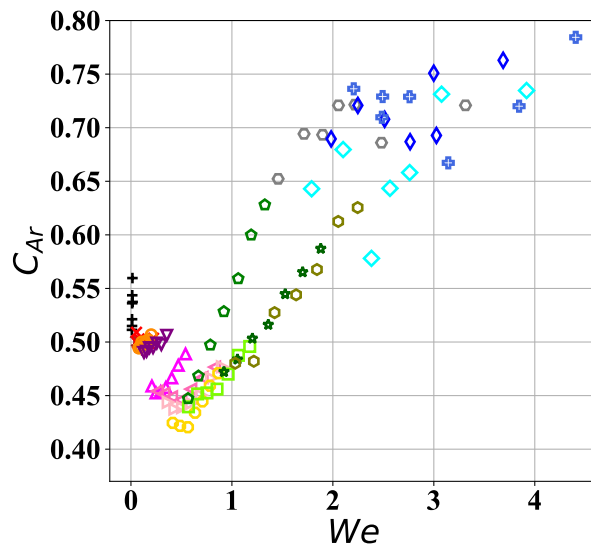


Figure 4.11: Added mass coefficient C_{Ar} as a function of We . C_{Ar} increases with We for most series.

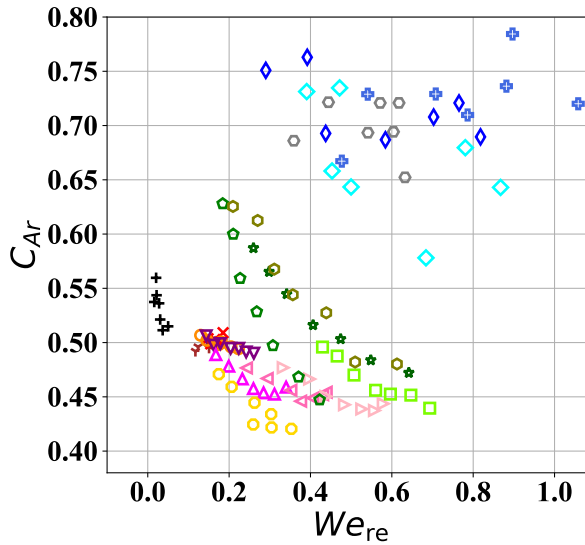


Figure 4.12: C_{Ar} as a function of We_{re} , which measures the impact of mean velocity $r_e\omega$ on the shape of the bubble. For a given series, the added mass decreases when We_{re} is increased due the increase in X_F .

4.3.2 Measuring the value of the lift coefficient (C_L)

These computed added mass coefficients are then used to deduce C_L : figure 4.13 shows the variations of the lift coefficient C_L as a function of Re , and the comparison to some of the correlations introduced in Rastello et al. 2017 for much larger Ro . The lift coefficient appears smaller than that measured by Bluemink et al. 2010 or Rastello et al. 2017. The fact that C_L is overestimated by these correlations could be caused by the smaller Ro in our experiments.

A decrease of the lift coefficient when Ro is reduced has been observed by Rastello et al. 2017 (see figure 20 of their paper). Note however that this decrease has been observed for $Ro > 6$ i.e. bubbles located much farther from the axis. Bluemink et al. 2010 observed similar trends for spheres and investigated a few locations closer to the axis. They noted that C_L decreased with the shear rate $Sr_\omega = Ro^{-1}$ up to $Sr_\omega = 0.4$ ($Ro = 2.5$) and that afterwards, the decrease stopped and C_L became constant. This suggests that the influence of Ro could also be limited in our case. The question of the limit of C_L when Ro becomes small remains an open question.

Besides the effect of Ro , we know from the literature (Kariyasaki 1987, Hayashi et al. 2020, Rastello et al. 2017, Magnaudet and Eames 2000) that bubble deformation can yield a decrease of the lift force and can even make this force change sign from positive to negative. Even though the main bubble stretching is aligned with the rotation axis, larger bubbles are actually also deformed in the (r, θ) plane, see figure 2.33 and figure 3.7 at low ω for example: for these non axisymmetric cases bubble deformation certainly affects the value of the lift coefficient. Note finally that the motion of the bubble around its equilibrium position may increase the inertia of the surrounding fluid, and hence lead to an increase in the *effective* added mass: the data of figure 4.13, which does not take this effect into account, is therefore expected to represent an underestimation of C_L .

When the bubble moves closer to the axis of rotation at low Ro , and in particular when it straddles the axis of rotation of the cell, the flow configuration changes: the relative importance of the shear increases, and the relevant Reynolds number is expected to become at some point the shear Reynolds number $Re_{shear} = Re/Ro$ introduced in sections 2.4 and 4.2. We plot in figure 4.14 the variations of the lift coefficient C_L as a function of Re_{shear} : the data of figure 4.13 appear better collapsed. The decrease of C_L as a function of Re/Ro observed in the range $Re_{shear} = 500 - 2500$ is consistent with the decrease observed by Rastello et al. 2017 when Ro^{-1} is increased, and when the Reynolds dependence is accounted for.

A sharp transition seems to occur for large bubbles when Re_{shear} becomes larger than 2800 (greyed region in figure 4.14). This corresponds to the conditions for which we approach the resonance described in section 3.3. We show in figure 4.15 how the increase in the lift coefficient appears correlated with the strong increase of the variance of the longitudinal aspect ratio X . The strong increase of these fluctuations appears related the forcing of the bubble stretching discussed in section 3.3. We introduced in chapter 3, section 3.3 $\omega_0 = \sqrt{96\sigma/\rho L^3}$ as an estimate of the eigenfrequency of the stretched bubble (Risso 2000): as explained in this section, when ω is increased, ω_0 decreases due to the stretching of the bubble and ω and ω_0 will be the same order of magnitude (see section 3.3 where the values of ω_0 close to break-up were discussed). Figure 4.16 shows that the transition observed around $Re_{shear} = 3000$ in figure 4.14 corresponds to ω approaching ω_0 . The resonance expected for these conditions may explain the

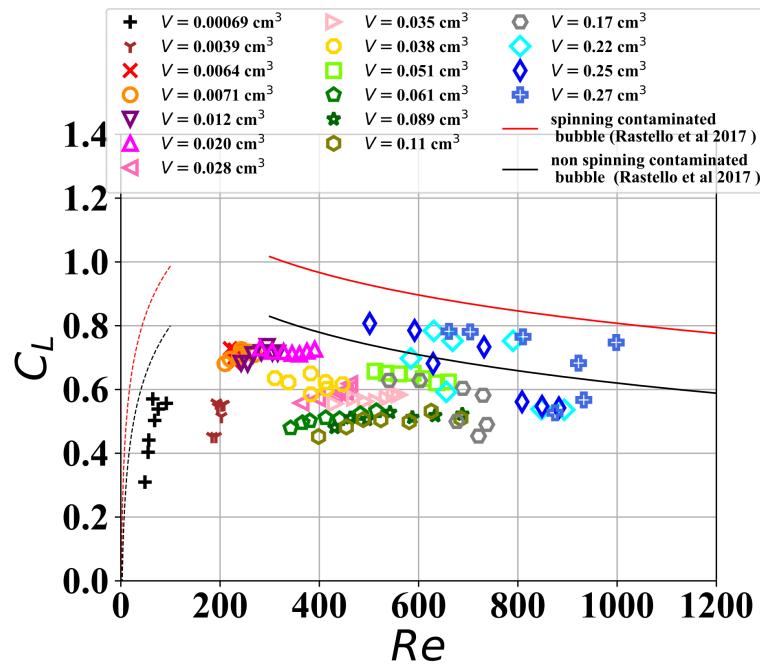


Figure 4.13: Lift coefficient as a function of Reynolds number. The dashed and solid lines correspond to equations (B1)-(B2)-(B5) in Rastello et al. 2017: Black line: the bubble does not spin. The lift is only induced by the rotation flow, equations (B2)-(B5). Red line: the bubble is supposed to spin with the same rotation speed as the tank. This scenario is possible as the bubble is contaminated and located on the rotation axis. Rotation adds a contribution equal to $3/16$, equation (B1). Equation (B2) is the correlation of the numerical results of Bluemink et al. 2010 for non-spinning sphere ($Re \leq 200, Sr_\omega = Ro^{-1} \leq 0.1$); equation (B5) is the correlation of the experimental data of these authors for non-spinning sphere ($Re > 274, Sr_\omega = Ro^{-1} \leq 0.4$), with a different additional constant: 1.82 against 1.99 in Bluemink et al. 2010.

strong increase observed in the fluctuations of the aspect ratio.

The question is then why the resonance provokes this steep apparent variation in the lift coefficient. A possibility could be that this apparent increase is caused by the much larger fluctuations in the position for these larger bubbles. Relative variations of r_e can reach up to 30-40% when resonance occurs, compared to

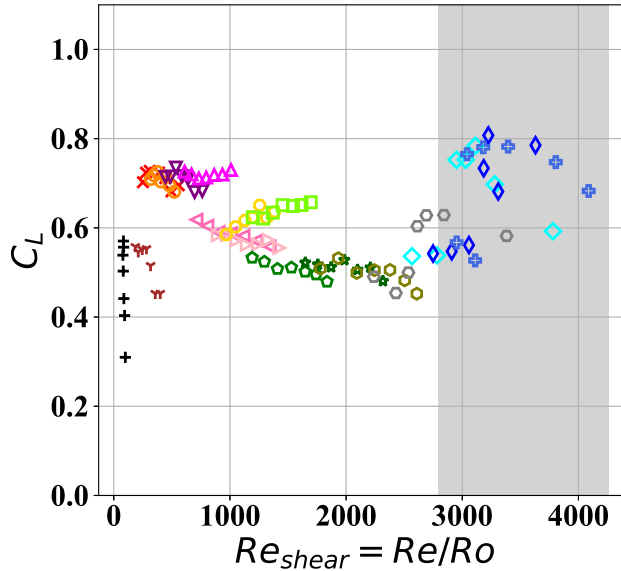


Figure 4.14: Lift coefficient as a function of shear Reynolds number, $Re_{shear} = Re/Ro$. The greyed region corresponds to conditions where the bubble experiences strong shape fluctuations.

less than 10% for all series of bubbles with $Re_{shear} < 2500$. These fluctuations in position are probably themselves triggered by the strong fluctuations in the shape of the bubbles. At any rate, because of these large fluctuations in r_e , mean values of C_L for $Re_{shear} > 2500$ deduced from the mean position result in fact from the averaging of a strongly non-stationary dynamics, something which is not accounted for in the equations leading to system (4.6).

4.3.3 Spinning

The other rather essential feature of our experiments compared to previous works is the question of bubble spinning. When experiments are performed in demineralized water like the one used here, the surface of the bubble is contaminated and in this case the bubble is expected to "spin". This has been shown for small bubbles at equilibrium far from the axis of rotation ($Ro \geq 6$) by tagging the flow near their surface with small fluorescent particles, in Rastello et al. 2009. Some of these particles stuck on the surface are clearly rotating around

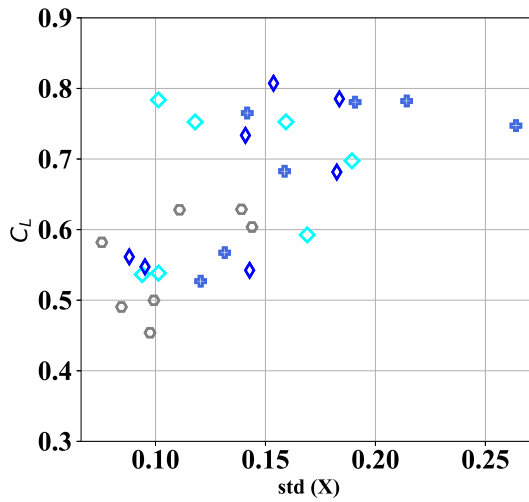


Figure 4.15: Lift coefficient as a function of the variance of the longitudinal aspect ratio X .

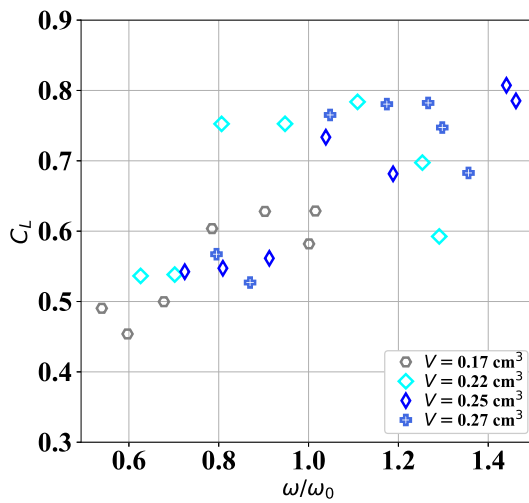


Figure 4.16: Lift coefficient as a function of the ratio between the tank rotation frequency and the eigenfrequency of the stretched bubble ω_0 .

the bubble (see for example fig 14 in this reference). Their motion has more recently been characterized in detail from numerous visualizations in Rastello et al. 2017. Visualizations suggest that the fluorescent particles rotate with the same velocity as that of the fluid at the surface, as imposed by the boundary conditions on the contaminated surface of the bubble. Rastello et al. 2017 assimilate their motion to the rotation of the surface and speak of a "spinning" surface. For bubbles with $Ro \geq 6$, the mean spinning rate is higher than the rotation rate: up to 1.6, depending on Re (figure 10 Rastello et al. 2017). This results in an extra Magnus-like lift force and a separated wake behind the bubble whose description can be found in Rastello and Marié 2020.

Knowing whether the bubbles still spin in the present flow situation would of course be interesting. Front view images show that when bubbles are non axisymmetric, the axisymmetry remains in average oriented along the same direction (see figure 4.17). However, the orientation of the bubble oscillates around this mean value at a frequency equal to the tank rotation frequency. This can be seen in figure 4.17, where the peaks in the orientation angle occur every 0.1 s, in agreement with the rotation frequency of 10 Hz. A sequence of images shows that even though the orientation remains approximately constant, the shape of the bubble fluctuates (see figure 4.18 below): we suspect that the bubble rotates, but the deformation which occurs at the same time prevents from measuring this rotation by simple visualization, as would be possible with a solid particle.

A direct measurement of the spinning such as that carried out in Rastello et al. 2009 could in principle be attempted to check if this rotation is indeed present, but this would be somewhat difficult to perform in the present case. In particular, it would be difficult to get a uniform seeding at the high rotation speeds we investigate here, with expected centrifugal effects and shorter exposure times (hence a need for a more powerful laser).

Now, given that these bubbles on average stabilize upon, or very close to the rotation axis ($Ro < 1$), it is probable that if spinning, they will spin at maximum with the rotation rate of the tank and not faster (Bluemink et al. 2008).

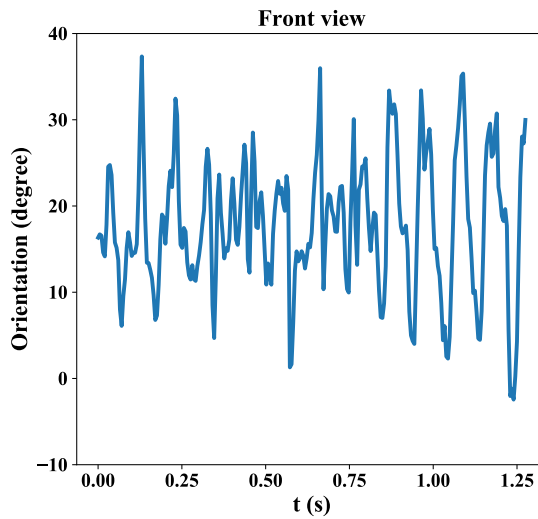


Figure 4.17: Bubble orientation relative to the horizontal direction, in degrees, for $V = 0.20 \text{ cm}^3$ and $\omega = 63 \text{ s}^{-1}$: the bubble orientation remains aligned towards the same mean direction of 17° , but oscillates around this value with a frequency equal to the tank rotation frequency, namely 10 Hz.

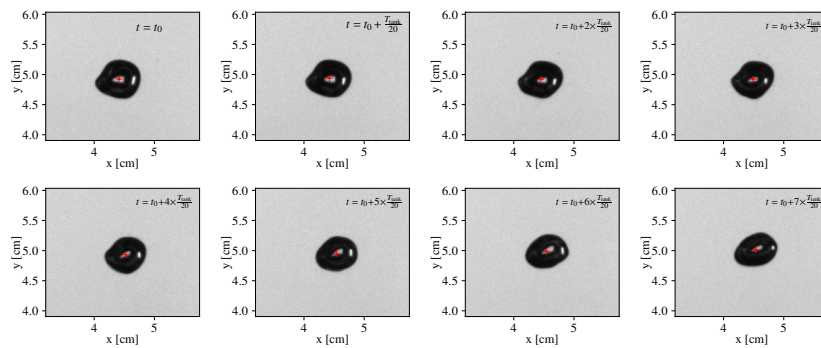


Figure 4.18: Sequence of images showing how the bubble deformation propagates along the perimeter for bubble of volume $V = 0.25 \text{ cm}^3$ at $\omega = 63 \text{ s}^{-1}$.

5

Effect of surfactants on bubble deformation and dynamics

In this chapter we will focus on the impact of the introduction of surfactant in the tank on bubble dynamics. As it has already been debated in 1.1.2, the surfactants distribution or small amount of impurities on the interface of the bubble alter the bubble dynamics. Surface tension of the surrounding water flow around the bubble has been constant ($\sigma \approx 71\text{mN/m}$) throughout all the results obtained in the previous chapters 3 and 4. In this chapter, the goal is adding soluble surfactant to the carrier flow inside the tank and investigate the behavior of the deformable bubble close to the axis of rotation. We will show that adding surfactants to the demineralised water leads to modifications of the bulk surface tension and of the dispersed phase (gas bubble) behavior.

We have used a chemical compound called *TetradecylTrimethylAmmoniumBromide* (*TTAB*) displayed in figure 5.1 to alter the surface tension of the bulk liquid. The critical micelle concentration (CMC) of *TTAB* is $C_{CMC} = 1.5\text{gr/L}$ (1.5gr of *TTAB* in 1L of demineralised water). At and above the C_{CMC} the surfactant distribution on the interface is saturated and there is no place on the interface to be permeated and filled by surfactants. Below the *CMC* value, the bubble interface is not entirely saturated by added soluble substance. To explore the effects of *TTAB* on the bubble dynamics, we have tested two separate *TTAB* concentrations in demineralised water. One solution of *TTAB* surfactant lower than C_{CMC} and the other higher than C_{CMC} .

TTAB : bromure de tétradécyltriméthylammonium ($\text{C}_{14}\text{H}_{29}\text{N}(\text{CH}_3)_3^+ \text{Br}^-$)

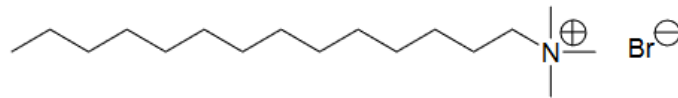


Figure 5.1: Structure of the *TTAB* surfactant. The chain of carbons is the hydrophobic side of the surfactant while the N^+ side is the hydrophilic head.

5.1 Solution with lower and higher concentration of TTAB in comparison with CMC

We have used two various recipes of *TTAB* in demineralised water. First, the solution below the CMC condition has been investigated. We have dissolved an amount of *TTAB* lower than 1.5gr in demineralised water. The process for making the solution is as below:

- **Step 1:** 0.5gr of *TTAB* (lower than CMC condition) dissolved in 100ml of demineralised water in a beaker of volume 100ml . Then, with use of magnetic laboratory agitator the solution was blended for 30 min at a temperature of 70° .
- **Step 2:** The solution prepared in the preceding step is poured into a beaker of 1L volume filled with 900 ml of demineralised water. Eventually, we have 1L solution which has been called C' (0.33 CMC) in the following sections of the manuscript.

The same scenario of solution preparation has been done for the amount of surfactant higher that the CMC concentration. For the second solution (higher concentration of *TTAB*), the value of *TTAB* added to the 100ml beaker filled via demineralised water is 3gr which is two times the CMC. We call this solution C'' (2 CMC). The objective is to test the effect of surfactants for both the unsaturated (lower than CMC, C' solution) and saturated (higher than CMC, C'' solution) interface. A summary of our solutions (C' and C'') preparation is illustrated in table 5.1.

Solution Name	TTAB (<i>gr</i>) in 1 L
C'	0.5 gr
C''	3gr

Table 5.1: Prepared surfactant solutions with *TTAB*. $C' = 0.33\text{ CMC}$ and $C'' = 2\text{ CMC}$.

The surface tension of the mentioned solutions in table 5.1 has been measured with a tensiometer (*Attension Theta Flex, Biolin Scientific AB*) similar to the process

of surface tension measurement for demineralised water explained in subsection 2.1.2. The measured surface tension is displayed as an output of the *Attension Theta Flex, Biolin Scientific AB* software. The surface tension for C' (0.33 CMC) solution as a function of time presents variations when the drop is issued, but surface tension converges to a plateau of 52 mN/m (figure 5.2).

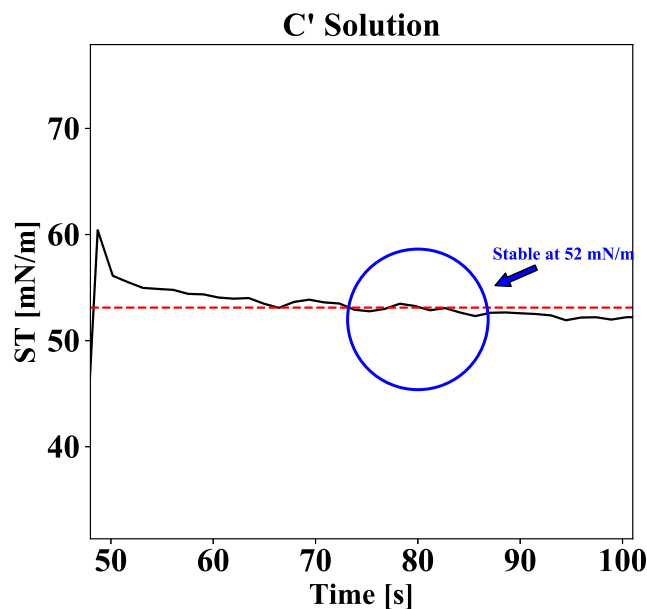


Figure 5.2: The measured surface tension of C' solution as a function of time shown by *Attension Theta Flex, Biolin Scientific AB*.

The variations of the surface tension value shown by the tensiometer are normal since we are in the condition of a lower concentration compared to the CMC, and there might be displacement of surfactant on the interface of the bubble released from the gauge needle.

In order to increase the accuracy of the surface tension measurement and verify the precision of the value found for C' (0.33 CMC) solution, we have used another pendant drop tensiometer named *Tracker Standard drop tensiometer* (located at Institut Lumière Matière, ILM) shown in 5.3. It measures the surface tension by a released drop from the gauge needle in front of a high resolution

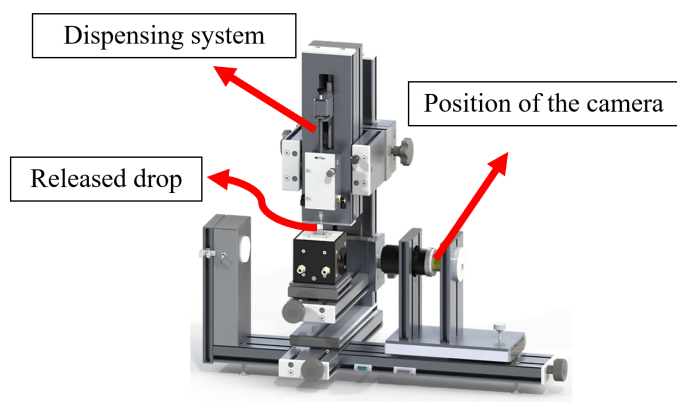


Figure 5.3: *Tracker Standard drop tensiometer device.*

camera identical to the *Attension Theta Flex, Biolin Scientific AB*. Then, the Tracker software implements the algorithms to determine the surface tension of the drop based on Young-Laplace equation. The difference of this tensiometer with the *Attension Theta Flex, Biolin Scientific AB* is the automatic control over the vibrations of the released drop from the gauge needle. This characteristic of the dispensing system facilitates the process of removing interface vibrations for the camera (to have an image acquisition without interface vibrations to measure surface tension with a higher precision). In addition, the dispensing system can oscillate sinusoidally and alter the volume of the released bubble from the gauge. This feature of the *Tracker Standard drop tensiometer* can also vary the volume of the bubble and therefore the area of the drop captured by the camera as a function of time which is consistent with our experimental condition (bubble volume variations, explained in subsection 2.2.3). Figures 5.4 and 5.5 display the values and error bars of the surface tension measured by *Tracker Standard drop tensiometer* when the volume of the released bubble changes sinusoidally as a function of time.

As it has been clarified, the value of the surface tension measured by two different tensiometers have been consistent (same values) in both cases of either with volume variations or fixed released volume of the needle gauges. Conse-

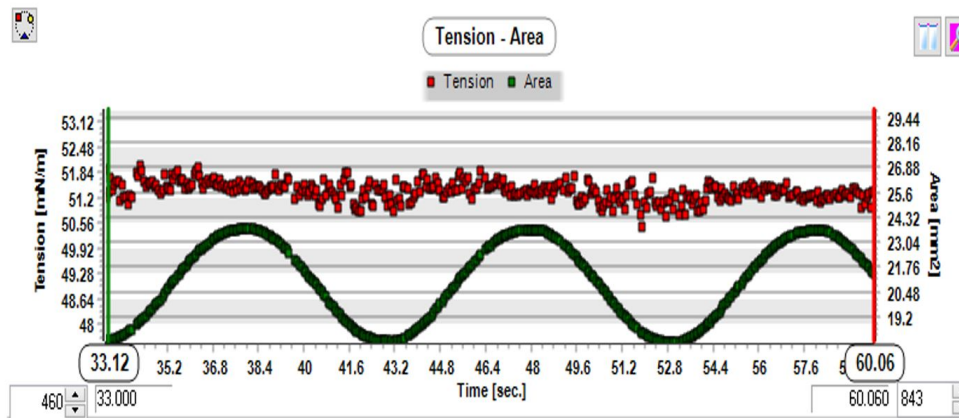


Figure 5.4: Red square points are the value of the surface tension measured by $(51.5 \pm 1.0 \text{ mN/m})$ *Tracker Standard drop tensiometer* when the volume of the bubble released from the gauge needle varies sinusoidally. The green sinusoidal signal is the area of the bubble captured by the high resolution camera when the volume varies.

quently we have assigned the surface tension values of our solutions (C' and C'') as below:

- For C' (0.33 CMC), $\sigma_{0.33CMC} = 51.5 \pm 1.0 \text{ mN/m}$
- For C'' (2 CMC), $\sigma_{2CMC} = 37 \pm 1.0 \text{ mN/m}$

For performing experiments to analyze the bubble dynamics in these two *TTAB* solutions (C' and C''), we have explicitly chosen the bubble volumes that do not encounter rupturing during the experiments. Since the surface tension has been reduced in comparison with demineralised water, we have not been able to investigate the dynamics of the bubble with volumes larger than $V = 0.16 \text{ cm}^3$ for ω in the range $[63, 94] \text{ rad s}^{-1}$. Therefore, in order to understand the dynamics of the bubble with presence of *TTAB* surfactant (C' and C'') and compare them with the case of demineralised water, we are limited to a range of volumes not larger than $V = 0.16 \text{ cm}^3$ (see tables 5.2 and 5.3).

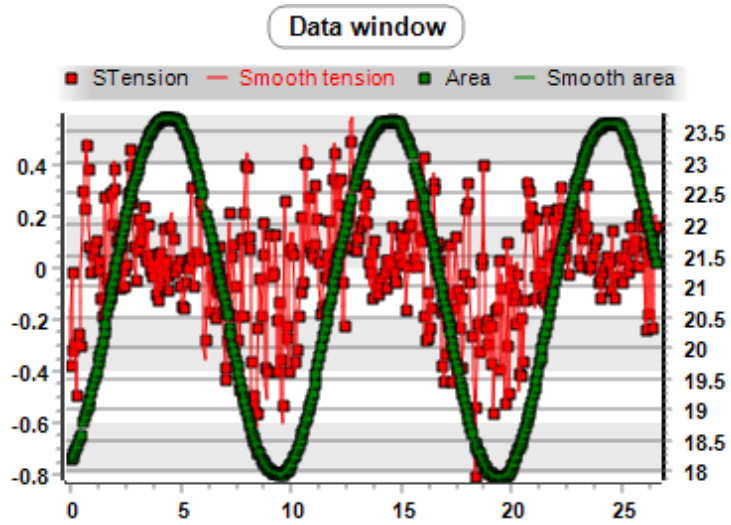


Figure 5.5: Zoom on variation of the surface tension when the volume of the released drop varies which justifies the chosen value of the 52 ± 1.0 mN/m.

Mean volume V [cm ³]	Mean equivalent radius R_{eq} [cm]
0.001	0.072
0.004	0.098
0.05	0.228
0.069	0.254
0.078	0.266
0.013	0.146
0.117	0.303
0.127	0.311

Table 5.2: Characteristics of the bubbles in solution C' (0.33 CMC): mean volume V and radius R_{eq} of a spherical bubble of equivalent volume.

5.2 Bubble deformation in presence of surfactants

5.2.1 Position of the bubble

Figure 5.6 shows r_e/D as a function of $g/D\omega^2$ for the C' and C'' solutions. This

Mean volume V [cm ³]	Mean equivalent radius R_{eq} [cm]
0.003	0.09
0.014	0.15
0.025	0.183
0.04	0.21
0.055	0.23
0.083	0.27
0.123	0.308
0.138	0.32
0.141	0.322

Table 5.3: Characteristics of the bubbles in solution C'' (2 CMC): mean volume V and radius R_{eq} of a spherical bubble of equivalent volume.

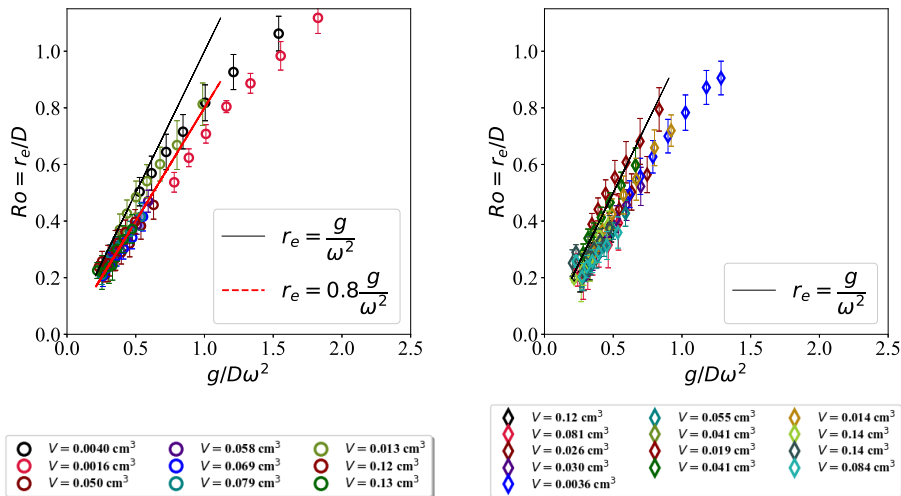


Figure 5.6: Variation of the Rossby number R_o as a function of $g/(D\omega^2)$. **Left:** bubbles in solution C'; **right:** bubbles in solution C''. The black line corresponds to equation 3.9. Same legend as figures 5.10 and 5.9.

figure displays a little difference in Rossby number (R_o) in case of C' (0.33 CMC) solution where the concentration is lower than CMC. On the contrary of the C'' (2 CMC) solution, the data of C' (0.33 CMC) solution are shifted slightly closer to

the axis of rotation and do not exactly follow the approximation of the $r_e = g/\omega^2$. The data follows the estimate of $Ro \sim 0.8g/D\omega^2$. Nevertheless, simultaneously to the section 4.2, we are still in condition of $Ro \leq 1$ (see figure 5.7) and the bubble crosses the center of rotation. Moreover, with increasing the rotating

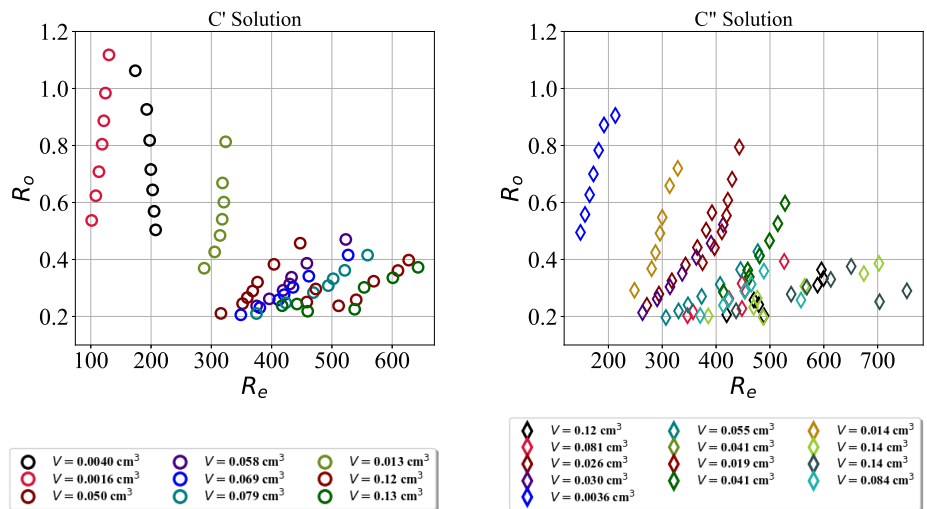


Figure 5.7: Rossby number as a function of the Reynolds number for bubbles in solutions C' (0.33 CMC) and C'' (2 CMC). \circ : C' solution (left); \diamond : C'' solution (right). Same legend as figures 5.10 and 5.9.

velocity ω , the larger bubbles of C' (0.33 CMC) experienced a drop of Ro (figure 5.7, left) proving that the bubbles with volumes larger than $V = 0.005\text{cm}^3$ in case of C' (0.33 CMC) solution are positioned closer to the axis of rotation in comparison with the data for water (figure 4.3) and for C'' (2 CMC) (figure 5.7 right). The other interesting point about the position of the bubble is the angle θ (polar coordinate of the center of the bubble) with the vertical axis of y (same as figure 4.2). Figure 5.8 shows that the angle θ with the y axis is around 80° for water, C'' (2 CMC) solution and C' (0.33 CMC) solution. This indicates that the bubble maintains a similar position in the presence of surfactants.

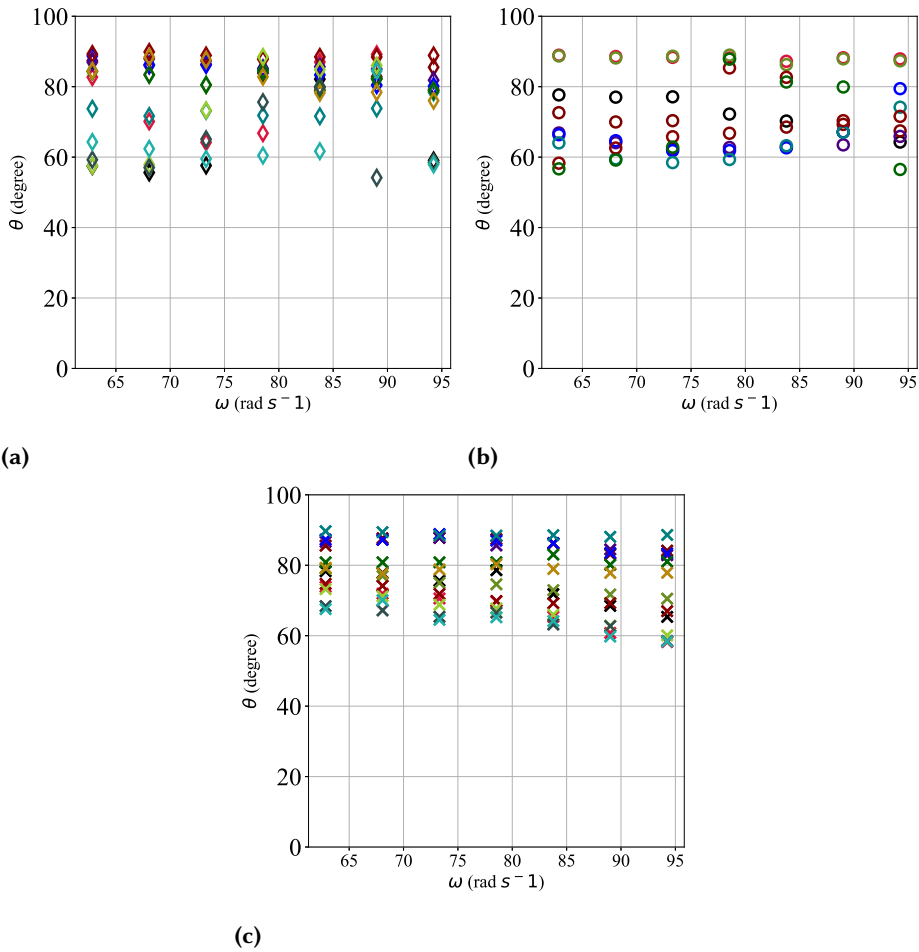


Figure 5.8: The angle θ (in figure 4.2) as a function of the rotation speed. **a)** bubbles in C'' solution (\diamond); **b)** bubbles in C' solution (\circ); **c)** bubbles in demineralised water (\times).

5.2.2 Bubble interface configuration

In order to study the deformation of the bubble in the two different discussed solutions (C' and C''), we first plot the variations of the longitudinal aspect ratio X as a function of the rotational speed. As illustrated in figures 5.9, 5.10 and 5.11, the aspect ratio X for the case of surfactant solutions are higher than for

demineralised water for given volume and ω values. The symbols \circ (data of C' solution) and \diamond (data of C'' solution) have been shifted up in comparison with symbols \times (data of demineralised water) for the same range of volumes ($0.004 \text{ cm}^3 < V < 0.13 \text{ cm}^3$) which shows that the bubble is much more stretched along the horizontal axis in presence of surfactants. Since the bubble is close to

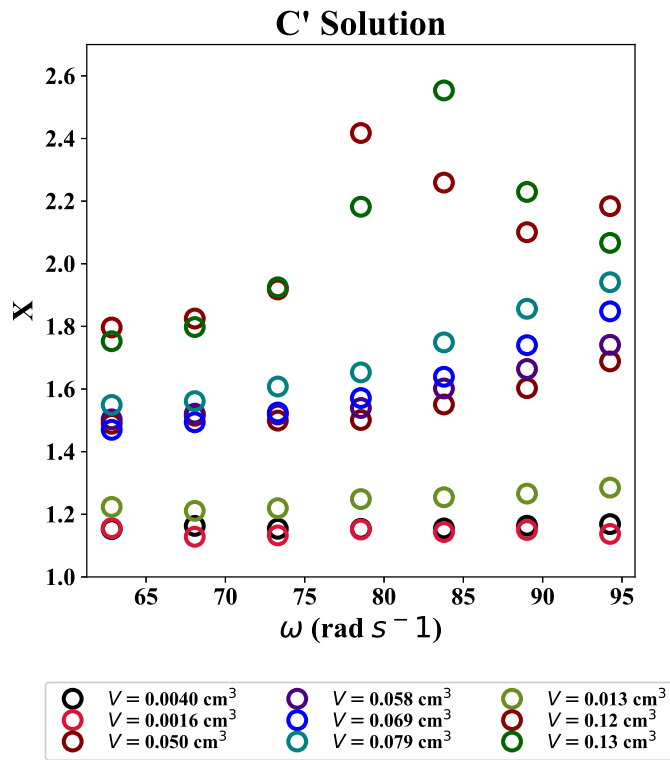


Figure 5.9: The aspect ratio of the bubble $X = L/D$ as a function of rotation speed ω for C' solution (0.33 CMC).

the axis of rotation (similar to condition of demineralised water), the aspect ratio of the bubble should be predicted by the model of Rosenthal 1962 as in figure 3.12 for demineralised water. Moreover, we plot the aspect ratio as a function of the corrected Weber number introduced in chapter 3, taking into account the corrected values of the surface tension measured by the tensiometers. As it is represented in 5.12, left, the data for the C' (0.33 CMC) solution (surface tension

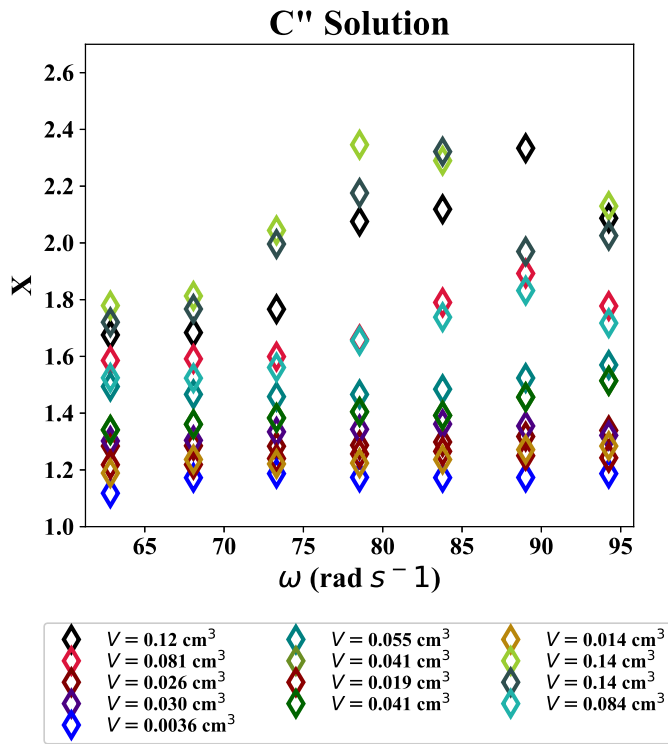


Figure 5.10: The aspect ratio of the bubble $X = L/D$ as a function of rotation speed ω for C'' solution (2CMC).

lower than CMC) are not perfectly collapsed with the Rosenthal 1962 prediction and the deformation of the experimental data are larger. However, the data for the C'' (2 CMC) have been very well fitted with the solid line of the model. These two physical phenomena can be interpreted via two concepts. On the one hand, concerning C' solution, the interface may not be comprehensively saturated with surfactant. Thus, there might be accumulation or inhomogenous distribution of the surfactant on the different regions of the bubble interface in particular close to the center of rotation of the tank. This displacement of the surfactants may lead to surface tension variations across the bubble. Therefore, the determined surface tension (52 mN/m) might not correspond to the effective value for the present ω range (rotational speeds in a range $[62, 94] \text{ rad s}^{-1}$). In order to test

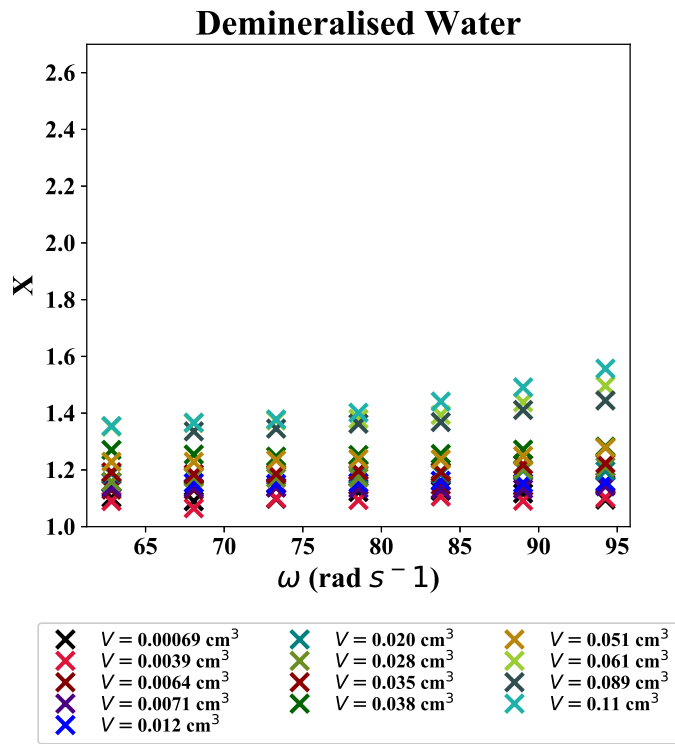


Figure 5.11: The aspect ratio of the bubble $X = L/D$ as a function of rotation speed ω for demineralised water.

this hypothesis, we alter in the Weber number the surface tension to the lower value $\sigma = 37 \text{ mN/m}$ which is the surface tension of the CMC condition, and we observe that in that case the data for C' (0.33 CMC) follows the model (figure 5.13 right). This means that the effective surface tension seen by the bubble is the CMC concentration even though we are at 0.33 CMC. On the other hand, regarding the C'' (2 CMC) solution (figure 5.12, left), the data is more properly aligned with the solid line of the model as was the case for demineralised water (figure 5.14, b). We interpret this as the fact that for C'' (2 CMC) solution the distribution of the surfactants on the bubble interface is saturated, and therefore more homogeneous than for the C' case. For the case of demineralised water, the bubble interface is not comprehensively clean and the bubble has a contaminated

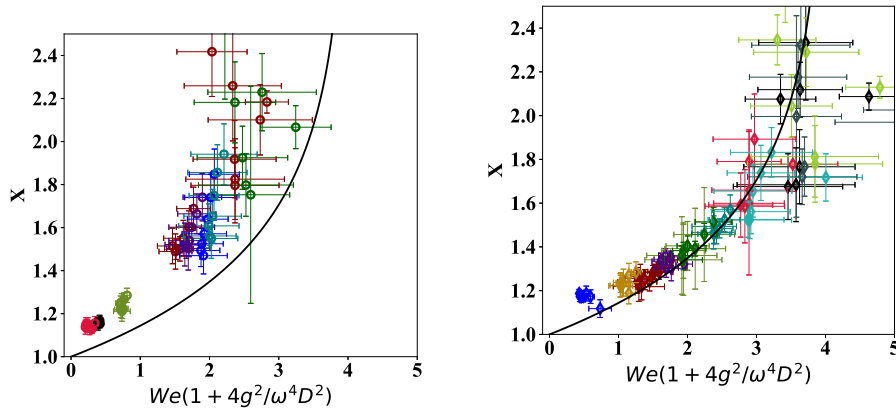


Figure 5.12: Bubble aspect ratio $X = L/D$ as a function of the corrected Weber number. **Left:** bubbles in C' solution; **right:** bubbles in C'' solution. The model works well for the C'' case.

interface. In respect of the chapter 2.1, it has been explained that there are constraints to maintain the water inside the tank perfectly clean. Moreover, in water we have impurities the nature and concentration of which is unknown and σ is about 71mN/m . Thus, if we zoom on the part of our experimental data in figure 5.14, b, we observe the prediction of the Rosenthal 1962 for fully saturated interface (2 CMC) fits better with experimental data compared with the partially contaminated interface (demineralised water).

As it has been discussed in chapter 3, the other dimensionless number representing the shape of the bubble is the *front view* aspect ratio X_F (aspect ratio in $(\hat{r}, \hat{\theta})$ plane). Figure 5.15 illustrates that for our two surfactant solutions the values of the *front view* aspect ratio are higher than that for demineralised water for the same volume range. The values of X_F reach up to 1.6 (except for smaller bubbles that do not straddle the axis of the rotation) for C' and C'' , while for water the maximum value of X_F (for the largest bubble of $V \approx 0.12\text{cm}^3$) is around 1.4. Indeed, the deformation of the bubble in the cross section depends on Ro . More precisely, for the bubbles with $Ro > 0.5$ (those which do not straddle the axis of the rotation), the deformation in the cross section is controlled by the mean velocity seen by the bubble (ωr_e). Therefore, as already discussed in chapter 4, the relevant dimensionless number controlling this deformation should be the Weber number built with the mean velocity seen by the bubble

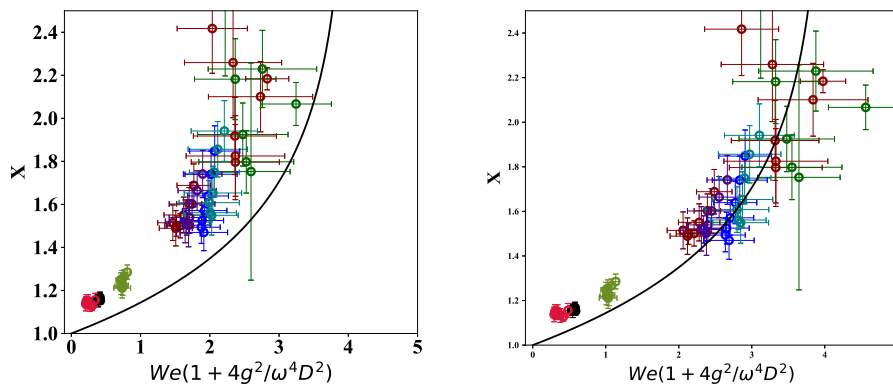


Figure 5.13: Bubble aspect ratio $X = L/D$ as a function of the corrected Weber number for the case of the C' solution. **Left:** Weber number computed with a surface tension $\sigma = 52\text{mN/m}$; **right:** Weber number computed with effective surface tension $\sigma = 37\text{mN/m}$.

$We_{re} = \rho(r_e\omega)^2 R/\sigma = 4WeRo^2$. Figure 5.16 shows the variations of X_F as a function We_{re} for C' , C'' and demineralised water data. The figure illustrates that the *front view* aspect ratio for the smaller bubbles depends on this Weber number seen by the bubble. However, for the larger ones the data are scattered and do not have the same behavior. Therefore, we divide our data (for water and both *TTAB* surfactant solutions) into two series of bubbles. First series, those which straddle the axis of rotation ($Ro < 0.5$) and the second series having $Ro > 0.5$. Figure 5.17, left, justifies that for both surfactant solutions (C' and C'') and demineralised water, the values of X_F follow the same trend as a function of We_{re} . However, the *front view* aspect ratio of the bubbles with $Ro < 0.5$, i.e. bubbles sitting on the axis of rotation, appear rather controlled by the Rossby number Ro itself (see figure 5.17, right).

5.3 Forces

5.3.1 Drag

In order to deduce the drag coefficient, we use equation 4.6b. We plot the standard drag coefficient C_D as a function of Re to investigate the value of the drag coefficient when surfactant *TTAB* is dissolved in the tank. It is apparent from figure 5.18 that the value of C_D as a function of Re reaches up to 9 for

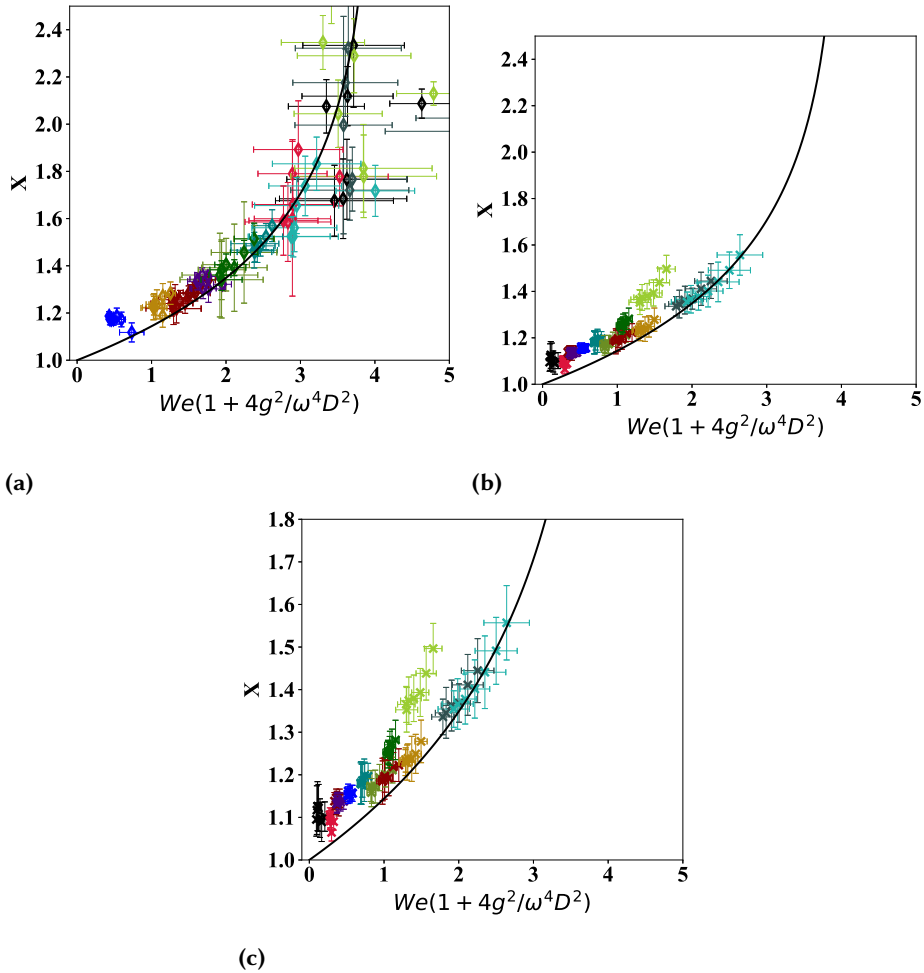


Figure 5.14: Bubble aspect ratio $X = L/D$ as a function of the corrected Weber number. **a):** bubbles in C'' solution; **b):** bubbles in demineralised water; **c):** zoomed on the data points of **b** for demineralised water.

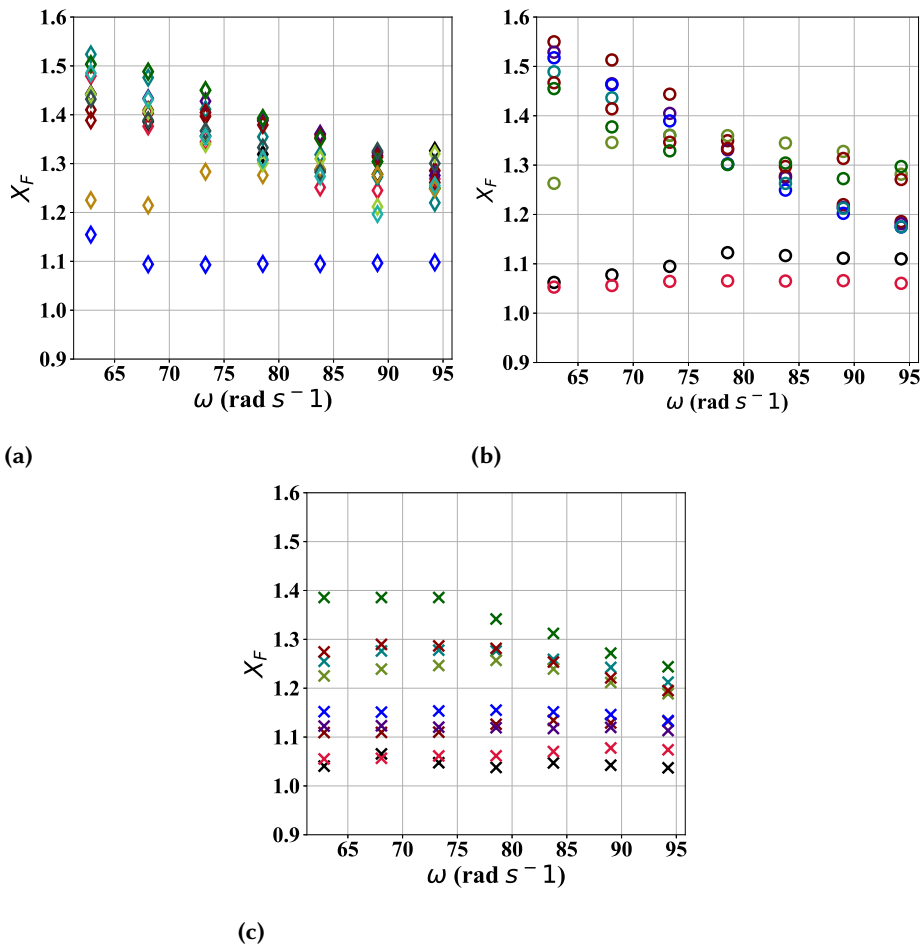


Figure 5.15: Variations of the aspect ratio X_F (aspect ratio of *front view*) as a function of the rotation speed ω . **a)** bubbles in C'' solution (\diamond); **b)** bubbles in C' solution (\circ); **c)** bubbles in demineralised water (\times).

both surfactant solutions. Note that similar to the demineralised water case, the contribution of the non-diagonal added mass term ($C_{Ar\theta}$) is small for all the series in C' and C'' solutions (figures 5.19 and 5.20). Figure 5.18, left related to the C' (0.33 CMC) case shows the values of C_D are still large. We introduce the drag coefficient CD_Δ clarified in chapter 4, and plot its variations as a function

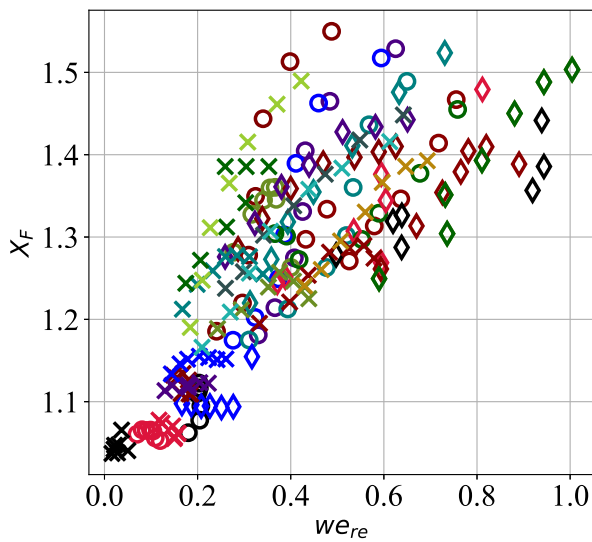


Figure 5.16: Aspect ratio of front view X_F as a function of We_{re} . \circ : C' solution; \diamond : C'' solution; \times : demineralised water.

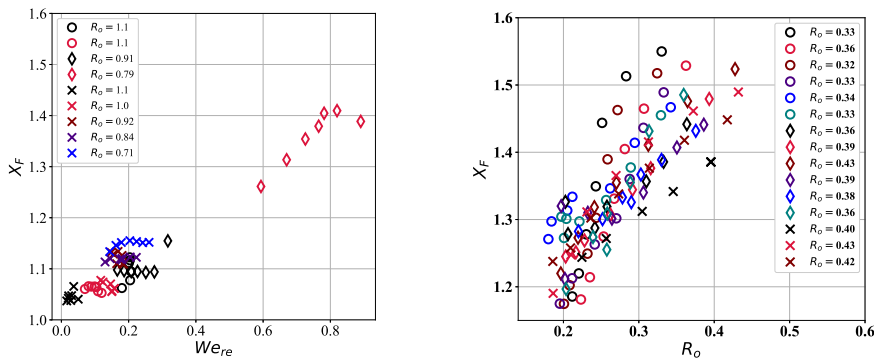


Figure 5.17: Aspect ratio of front view X_F as a function of Ro and We_{re} . **Left:** Bubbles with $Ro > 0.5$. **Right:** Bubbles with $Ro < 0.5$. Bubbles in C'' solution (\diamond); bubbles in C' solution (\circ); bubbles in demineralised water (\times).

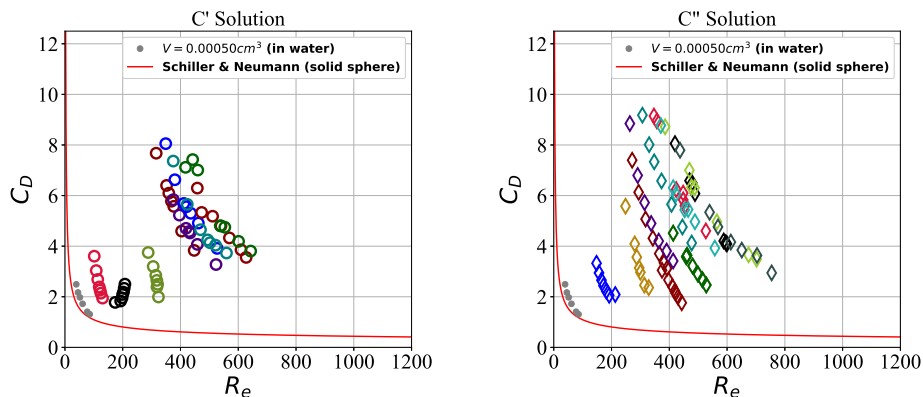


Figure 5.18: Standard drag coefficient C_D as a function of the Reynolds number. **Left:** bubbles in C' (0.33 CMC) solution; **Right:** bubbles in C'' (2 CMC).

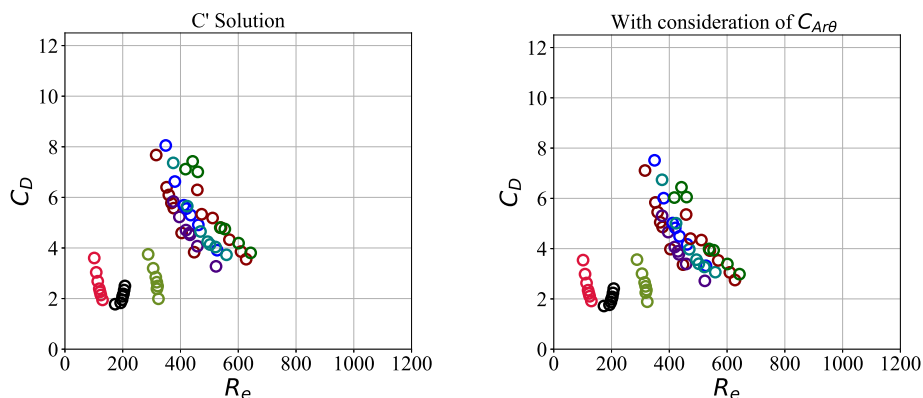


Figure 5.19: Standard drag coefficient C_D as a function of the Reynolds number for C' (0.33 CMC) solution. **Left:** without consideration of non-diagonal added mass term $C_{Ar\theta}$; **Right:** with consideration of non-diagonal added mass term $C_{Ar\theta}$.

of $Re_{shear} = Re/Ro$ to correctly capture the effects of low Ro . Therefore, we use equation 4.5 as well as 4.8 (see figure 5.21).

Figure 5.21 shows that the values of $C_{D\Delta}$ in the C' and C'' (2 CMC) solutions are close to the values in water and can be approximated as $C_{D\Delta} \approx 0.75$

In order to inspect more closely the impact of surfactants on bubble shape, we

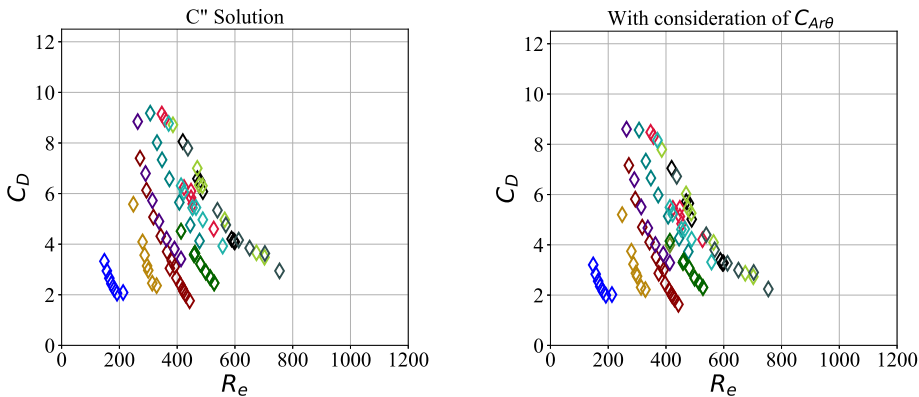


Figure 5.20: Standard drag coefficient C_D as a function of the Reynolds number for C'' (2 CMC) solution. **Left:** without consideration of non-diagonal added mass term $C_{Ar\theta}$; **Right:** with consideration of non-diagonal added mass term $C_{Ar\theta}$.

now look at the variation of the angle γ of the bubble. In the case of the bubble in demineralized water, the angle γ varies between -20 and 20 degrees, whereas in the case of C' and C'' solutions, this angle is in the range of 10 to 60 degrees (see figure 5.23). This corresponds to a different inclination of the bubble, as illustrated in figure 5.22.

This figure shows the superposed boundaries of two bubbles with a same volume of $V = 0.12 \text{ cm}^3$, at $\omega = 94 \text{ rad s}^{-1}$. The points represent the pixels pertaining to the contour of the bubbles in 10 consecutive recorded images. We can clearly visualize the shape of the interface for the water (black symbols) and C' (0.33 CMC) solution (blue symbols), for these two bubbles of identical volume. A change in shape can be observed. It points to the bubble being more streamlined in the case of the C' (0.33 CMC) solution for a solid body rotation flow around the cell center (red cross).

The variations of γ coupled to the variations in the position of the bubble (variations in R_0 and θ) may have an impact on the chord (see figure 5.24) of the cross section. The chord corresponds here to the length cut across the bubble in the (r, θ) plane, normal to the solid body rotation flow. This length will directly affect the projected area of the bubble. For water, we have supposed that γ is zero, as observed experimentally (5.23, c) for most of the series. Therefore, the

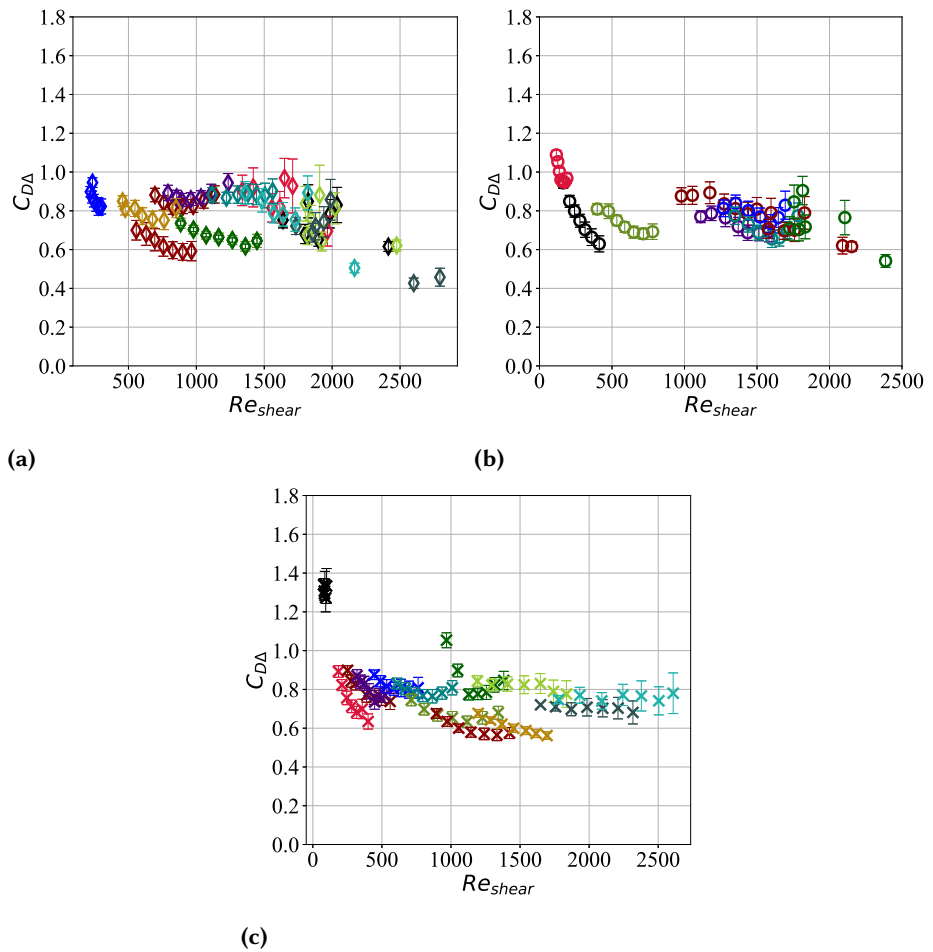


Figure 5.21: Drag coefficient $C_{D\Delta}$ as a function of Re_{shear} . **a)** bubbles in C'' solution (\diamond); **b)** bubbles in C' solution (\circ); **c)** bubbles in demineralised water (\times).

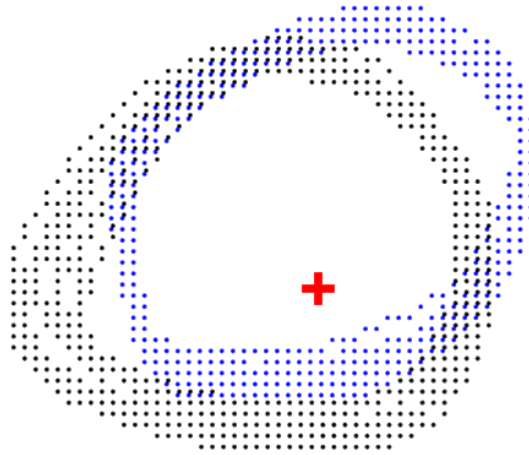


Figure 5.22: Average shape of a bubble of volume $V = 0.12 \text{ cm}^3$, obtained by superimposing 10 consecutive images. Black is for water, blue is for C' (0.33 CMC) solution. Red plus is the center of the cell.

chord of the cross section is defined as $Chord = 2a$ in figure 4.8, while in the case of C' and C'' solutions the chord is modified as:

$$Chord = 2\sqrt{a^2 \cos^2 \gamma + b^2 \sin^2 \gamma}$$

Figure 5.25 displays the ratio of the $Chord/D$ for the three solutions investigated here. The dimensionless number $Chord/D$ for the C' (0.33 CMC) solution is in average slightly lower than that for C'' (2 CMC) and especially demineralised water. Therefore, this confirms that the bubble is slightly more streamlined for this case, as illustrated in figure 5.22.

5.3.2 Lift

For computing the lift coefficient, we use equation 4.6a. As discussed in chapter 4, the measurement of the lift coefficient is made through the computation of the

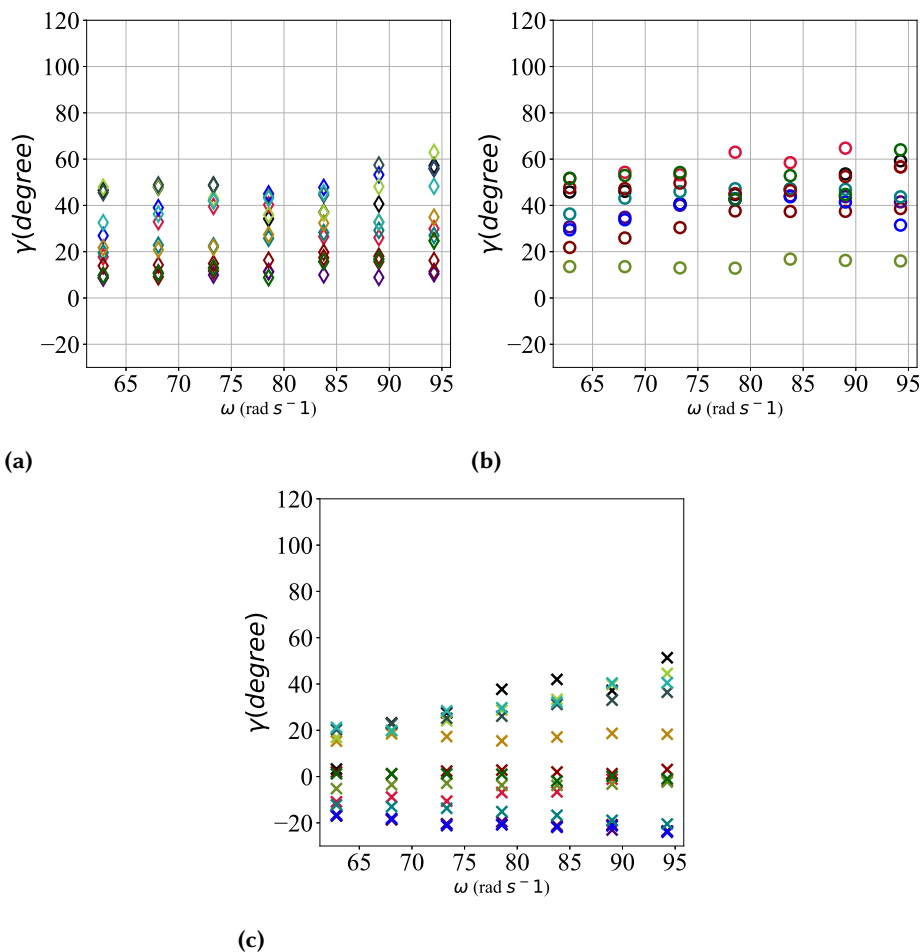


Figure 5.23: The angle γ (in figure 4.8) as a function of the rotation speed. **a)** bubbles in C'' solution (\diamond); **b)** bubbles in C' solution (\circ); **c)** bubbles in demineralised water (\times).

added mass coefficient. The simplified form of equation 4.6a can be written as:

$$2C_L - C_{Ar} = 1 - \frac{g}{r_e \omega^2} \cos \theta$$

$$C_L = \frac{1}{2} - \frac{g}{2r_e \omega^2} \cos \theta + \frac{C_{Ar}}{2} \quad (5.1)$$

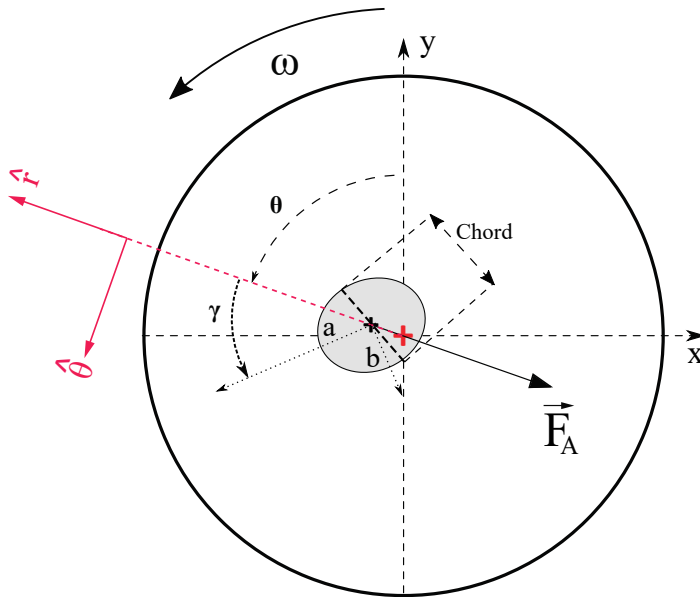


Figure 5.24: Schematic of the bubble configuration in C' (0.33 CMC) solution when the value of the angle γ increases and consequently the chord becomes close to the minor axis of the *front view*.

where concerning the method clarified in subsection 4.3.1, the added mass coefficient along r (namely C_{Ar}) can be computed knowing the shape of the bubble and its orientation. In chapter 4, we discussed the relation between C_{Ar} and the deformation of the bubble where the value of the added mass is controlled by the Weber number. This indicates that when the bubble stretches along the horizontal axis the value of C_{Ar} increases. We show in figure 5.26 the variation of C_{Ar} as a function of the Weber number for all the experimental data for the three solutions. The figure displays that the value of C_{Ar} for solution C' (0.33 CMC) is a little higher than that for C'' (2 CMC) and demineralised water. The value of C_{Ar} for water is in a range between 0.45 and 0.6, but in the case of the surfactant solution it rises up to 0.85 in C'' (2 CMC) and close to 1 for the case of C' (0.33 CMC). The reason for the mentioned difference in value of C_{Ar} is due to fact that the bubble in C' (0.33 CMC) is more deformed along z (comparison of figures 5.9, 5.10, and 5.11) compared to the C'' (2 CMC) and demineralised water.

Using equation 5.1 and by computing the value of C_{Ar} , we can now compute

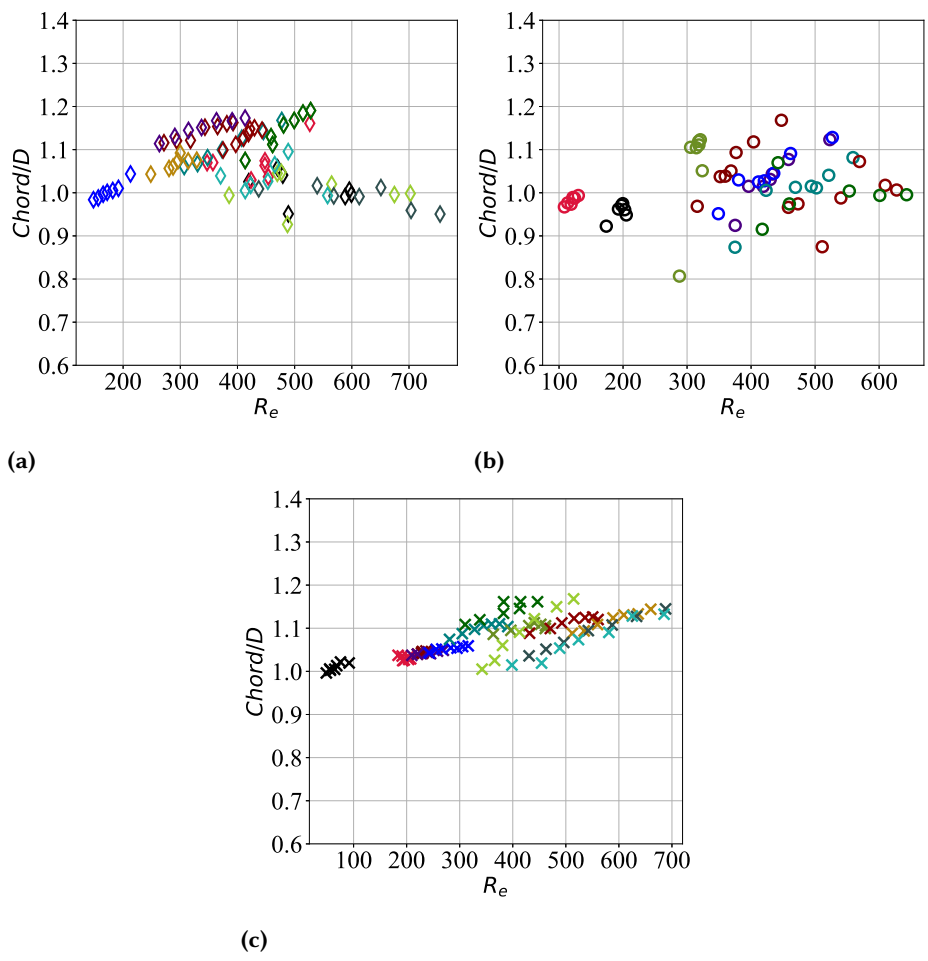


Figure 5.25: Dimensionless parameter $Chord/D$ (in figure 4.8) as a function of Re_{shear} . **a)** bubbles in C'' solution (\diamond); **b)** bubbles in C' solution (\circ); **c)** bubbles in demineralised water (\times).

the lift coefficient C_L . Figure 5.27 shows the variations of the lift coefficient as a function of Re . The results obtained in the presence of surfactant are similar to those obtained with demineralised water. As it has been discussed in chapter 4, section 4.3, since we are at low Ro and the bubble straddles the axis of rotation, the flow configuration changes. Thus, we plot the value of C_L as a function of

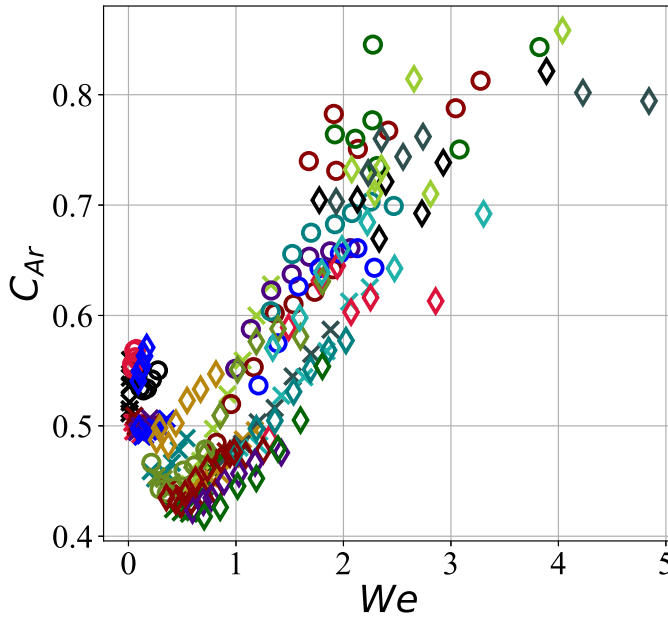


Figure 5.26: Added mass coefficient along r (C_{Ar}) as a function of $Re_{shear} = Re/Ro$ for three solutions. \diamond : C'' 52 CMC) solution; \circ C' (0.33 CMC) solution; \times demineralised water.

$Re_{shear} = Re/Ro$ (figure 5.28). Results obtained with surfactant are similar to those obtained with water.

5.4 Break-up

We now study how break-up of the bubble is impacted by the addition of surfactant to the solution. Figure 5.29 shows the bubble volume as a function of ω , and as in chapter 3, section 3.3 a circle indicates the conditions for which break-up occurs. This figure shows that bubble break-up occurs for smaller bubble volume ($V < 0.2 \text{ cm}^3$) in the TTAB solution than in the solution without surfactant. The figure shows that the bubbles for which break-up was observed are in the volume range of $[0.1, 0.17] \text{ cm}^3$. This has been expected that with adding surfactants to the tank and decreasing the value of the liquid surface

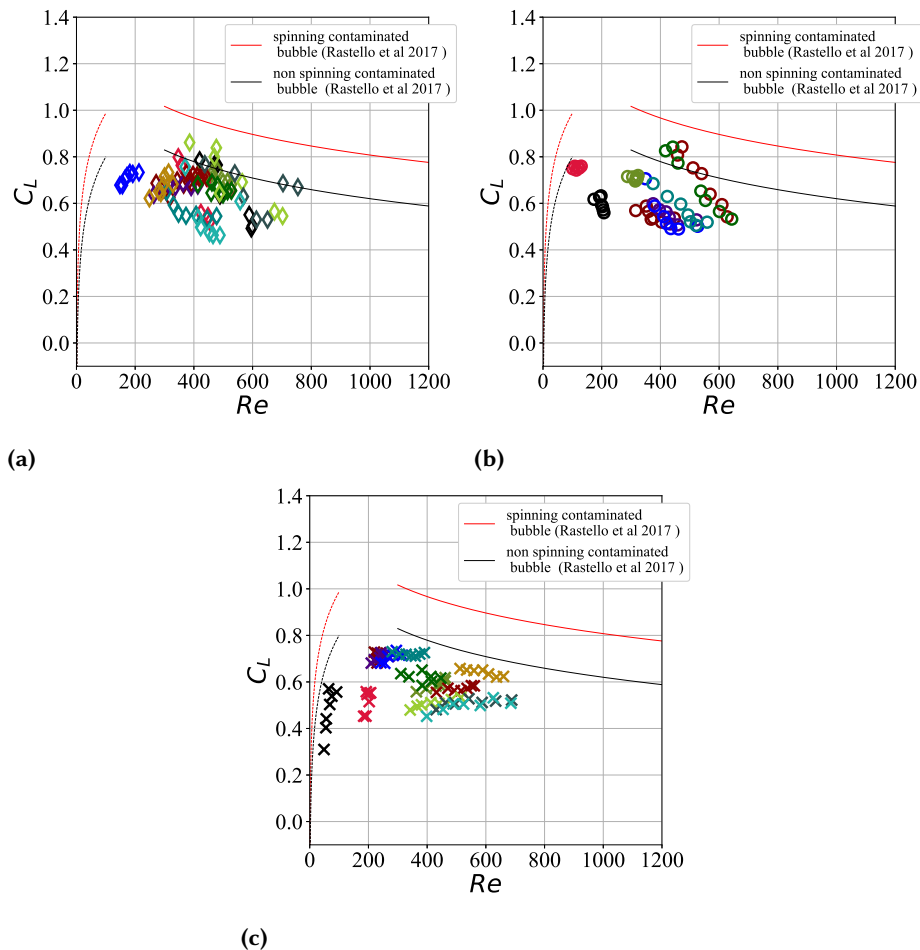


Figure 5.27: Lift coefficient C_L as a function of Re . **a)** bubbles in C'' solution (\diamond); **b)** bubbles in C' solution (\circ); **c)** bubbles in demineralised water (\times).

tension, the bubble experiences larger longitudinal stretching, and therefore breaks at smaller volume for a constant ω range.

Indeed, we have observed the same configurations of break-up as for water, namely *middle break-up*, and also breaking in two unequal size bubbles in presence of surfactants.

In chapter 3, section 3.3, we showed that the break-up of the bubble occurs

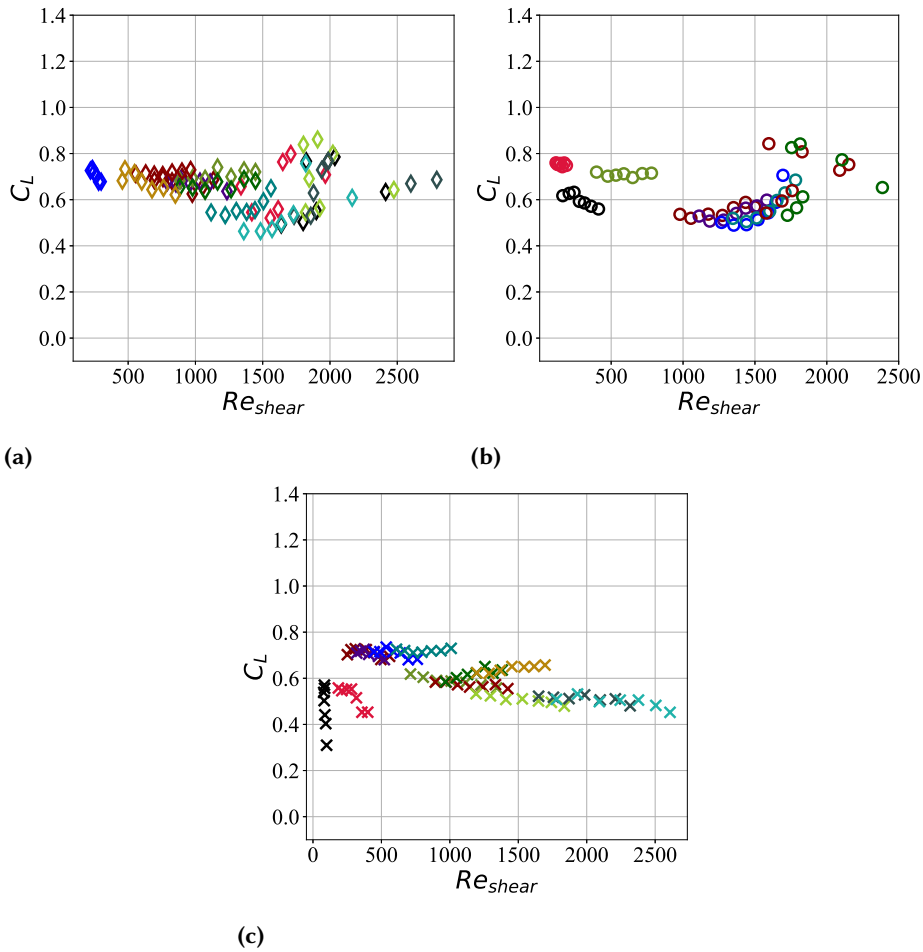


Figure 5.28: Lift coefficient C_L as a function of $Re_{shear} = Re/Ro$. **a)** bubbles in C'' solution (\diamond); **b)** bubbles in C' solution (\circ); **c)** bubbles in demineralised water (\times).

through a resonance mechanism between the eigenfrequency of the stretched oscillated bubble ω and the tank rotation frequency ω_0 . In addition, the shape mode of the bubble seems to be in configuration of $n=2$ in the moment of break-up. Figure 5.30 shows that the range of ω/ω_0 is independent of the size and the rotation velocity of the break-up in a range between 1.5 and 2.2 for the bubble

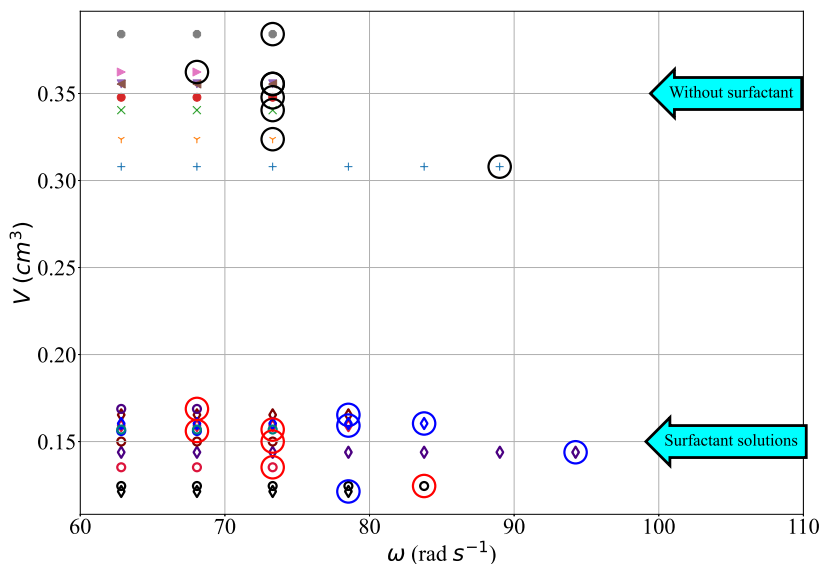


Figure 5.29: Color circles represent for each series of data the conditions for which the break-up happens (red circles → C' solution; blue circles → C'' ; black circles → water). Data with surfactant: the break-up occurs for bubbles with a volume V lower than 0.2 cm^3 . Data without surfactant (demineralised water): the break-up occurs for bubbles with a volume V higher than $V = 0.31 \text{ cm}^3$. \circ : C' solution; \diamond : C'' solution; the other symbols are the data of the demineralised water same as figure 3.17

frequency $\omega_0 = \sqrt{\frac{96}{\rho} \frac{\sigma}{L^3}}$ (left). It is also similar to the results in water when the eigenfrequency is estimated as $\omega_{0R} = \sqrt{\frac{12}{\rho} \frac{\sigma}{R_{eq}^3}}$ (right), with ω/ω_{0R} in a range between 0.62 and 0.83. This is consistent with the idea that break-up is driven by a resonance mechanism.

In order to strengthen the theory of the resonance, we carried out some other experiments in which the starting rotation speed is 94 rad s^{-1} and is decreased down to $\omega = 62 \text{ rad s}^{-1}$. This *reverse* ω experiment has been performed for the C'' (2 CMC) solution in a range of volumes $V=[0.14, 0.21] \text{ cm}^3$ (the same range

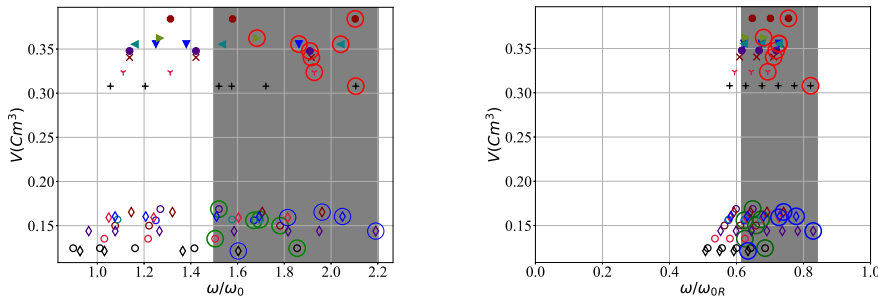


Figure 5.30: Volume of the broken bubble as a function of ratio ω/ω_0 (ratio between tank rotation frequency and eigenfrequency of the stretched bubble ω_0) for all experimental series experiencing break-up. Circles identify the rotation speed ω for which rupturing occurred. Same legend as figure 3.17. **Left:** eigenfrequency ω_0 estimated with length L . **Right:** eigenfrequency ω_{0R} estimated with length R_{eq} . \circ : C' solution; \diamond : C'' solution; the other symbols are the data of the demineralised water same as figure 5.29

of volume for which the break-up occurred by increasing ω in the previous experiments). Figure 5.31 represents the bubble break-up when we reversely vary the rotational velocity of the tank (circles are the conditions for which break-up occurred). We see the break-up of the bubbles with similar volume sizes as the bubbles in previous experiments when we performed experiment in a condition of increasing ω , but this time happening *below* the given rotational velocities.

The interesting point validating the hypothesis of the resonance is that in the case of *reverse break-up* the value of ω/ω_0 is approximately in the same range [1.6, 2.5], which a bit larger (see figure 5.32, left) in comparison with the increasing ω break-up shown in figure 5.30, left. Note that the ratio ω/ω_0 increases even in this reverse break-up experiment: the reason is that the bubble stretches when approaching the resonance, and as a result its eigenfrequency ω_0 decreases faster than ω when ω is reduced.

However, the value of the ratio ω/ω_{0R} when we choose the length of the bubble as R_{eq} , is still between 0.62 and 0.83 (see figure 5.32) which is consistent with our previous experiments. This is another indicator that resonance is the probable reason of bubble break-up in this flow situation.

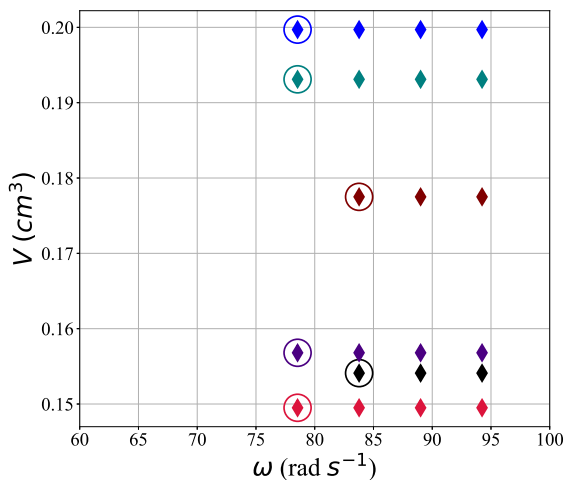


Figure 5.31: Volume of the bubble as a function of rotation speed for which *reverse break-up* is observed in C” (2 CMC) solution.

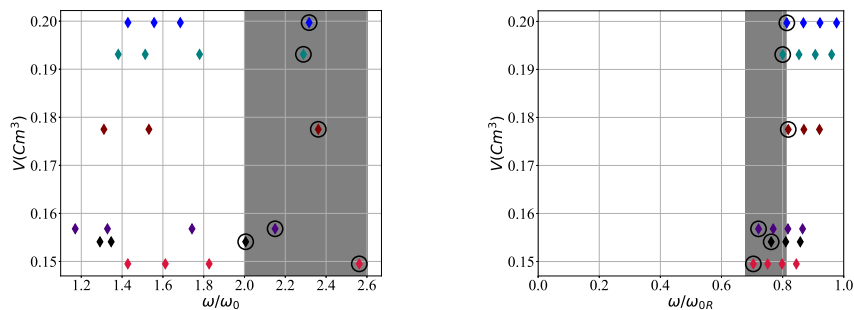


Figure 5.32: Volume of the broken bubble as a function of ratio ω/ω_0 (ratio between tank rotation frequency and eigenfrequency of the stretched bubble ω_0) for all experimental series experiencing break-up. Circles identify the rotation speed ω for which rupturing occurred for the *reverse break-up*. **Left:** eigenfrequency ω_0 estimated with length L . **Right:** eigenfrequency ω_{0R} estimated with length R_{eq} . Same legend as figure 5.31.

We have discussed in chapter 3 that the Weber number is a dimensionless parameter which controls the deformation of a deformable droplet or bubble in a high Reynolds number flows. Regarding the deformation of the bubble when break-up occurs (figures 3.13 and 3.16), the types of observed break-up, and the huge distortion of the bubble when it breaks (high amplitude of the *front view* and *side view* aspect ratio), we can expect that the Weber number becomes large at break-up. As our bubble is close to the axis of rotation and regarding chapter 3 where a corrected Weber number with effect of low Ro introduced, we plot the data of break-up as a function of this corrected Weber number $We' = We(1 + 4g^2/(D^2\omega^4))$. Figures 5.33, 5.34 and 5.35 left, illustrate the corrected Weber number as a function of volume for the three considered solutions. To expand, for instance, for water (figure 5.33, left) the break-up moment does not happen in highest Weber number. To modify the Weber number which controls the deformation of the bubble in this situation (distorted bubble before break-up), we write definition of the Weber number for the bubble stretched along the horizontal axis as:

$$We_L = \frac{\rho \omega^2 L^3}{\sigma}$$

Moreover, we know that $\omega_0 = \sqrt{\frac{96}{\rho} \frac{\sigma}{L^3}}$. Then, we can express this new Weber number as a function of ω/ω_0 as:

$$We_L = 96 (\omega/\omega_0)^2$$

If we now plot We_L as a function of bubble volume, we see that the break-up occurs in the highest Weber for each series of the data in different solutions (demineralised water, C' (0.33 CMC) and C'' (2 CMC)) (see the right figure of each solution in figures 5.33, 5.34 and 5.35).

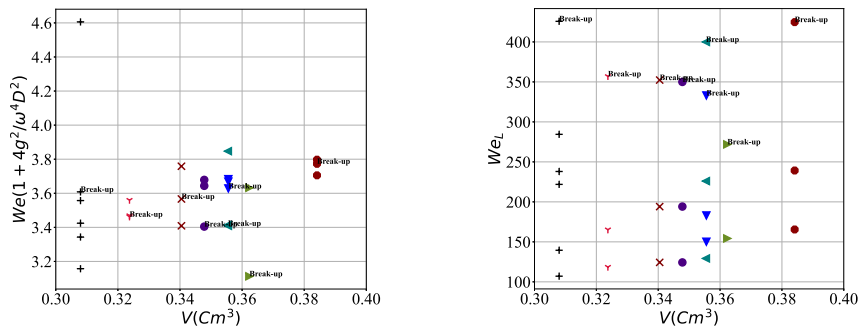


Figure 5.33: Left: Corrected Weber number presented in chapter 3 in a function of volume for the bubbles experiencing break-up in demineralised water. Right: We_L as a function of volume in demineralised water.

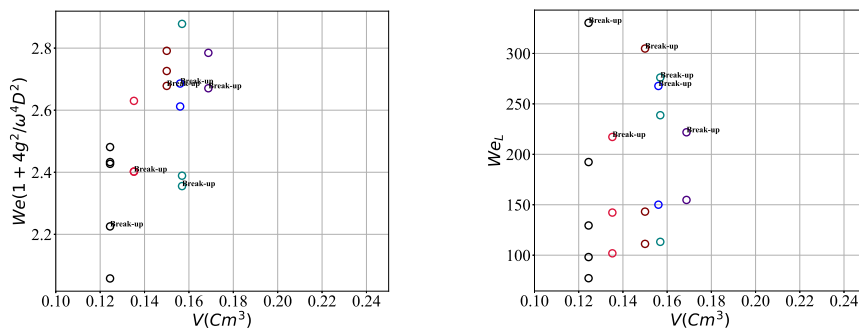


Figure 5.34: Left: Corrected Weber number presented in chapter 3 as a function of volume for the bubbles experiencing break-up in C' (0.33 CMC) solution. Right: We_L as a function of volume in the same solution (C').

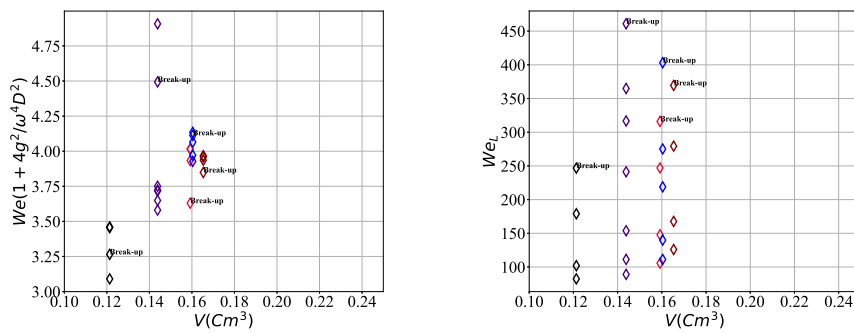


Figure 5.35: Left: Corrected Weber number presented in chapter 3 as a function of volume for the bubbles experiencing break-up in C'' (2 CMC) solution. **Right:** We_L as a function of volume in the same solution (C'').

6

Conclusion and perspectives

6.1 Conclusion

This chapter will wrap up the results presented in this manuscript by summarizing the major findings in connection to the research objectives and questions, as well as discussing their contribution. It will also go through the limitations of this study and make recommendations for further research.

This study aimed to investigate the behavior of a bubble in a horizontal high-speed solid body rotating flow. In chapter 2, the experimental apparatus and conditions for extracting information about the bubble in this type of flow were discussed. The experimental set-up is a cylindrical Plexiglass tank rotating around its horizontal axis. Two cameras have been used to extract bubble shape, position and interface movements along two directions. The bubble stretches along the axis of rotation in the recorded images, and its shape is similar to an ellipse. Then, using image analysis techniques, we were able to determine some key characteristics of the deformed bubble, such as its length (along vertical and horizontal axes), position, boundary contour, orientation, etc. We then used image processing and implemented image analysis techniques to determine the bubble volume, assuming the bubble has an ellipsoidal shape. According to the findings, increasing the rotation speed of the tank causes the bubble to stretch further and the volume to increase by up to 15% for most series. The elastic deformation of the Plexiglass tank has been proven to be the cause of this increase.

Finally, we discussed why we chose a rotation speed range of 63 to 94 $rad\ s^{-1}$ for our experiments. We demonstrated that in this range of tank rotation speed, the amplitude of the bubble oscillation remains moderate in comparison to the bubble dimension.

We discussed the bubble shape, position, and its rupture in Chapter 3 using the tools and methods from Chapter 2. Except for the smallest bubbles investi-

gated, we showed that the Rossby number $Ro = r_e/D$, where r_e is the distance to the axis of rotation and D the bubble diameter, is less than one for most of our experimental conditions. In other words, the bubble center of mass is not perfectly centered with the axis of rotation, but it is close to it and gets closer as the rotation speed increases.

Our experimental results showed that as the rotational velocity ω of the tank increases, the longitudinal aspect ratio X of the bubble increases up to 2.

We used the model proposed by Rosenthal 1962 for our experimental data since this model predicts the shape of the bubble in a solid body rotating flow. The model is inviscid, and assumes that the bubble is perfectly centered on the axis of rotation. We have shown that this model adequately captures the stretching of the bubble when its Weber number is increased, provided a correction accounting for the finite distance to the cell axis and the impact this has on the mean pressure field around the bubble is included. This model relies on the assumption that the bubble is axisymmetric: this is not the case when buoyancy breaks the symmetry. The correction we have proposed for the Weber number is nonetheless sufficient to capture the aspect ratio X of the bubble in a wide range of conditions.

Eventually, we concluded Chapter 3 by looking at how the stretched bubble breaks up along the axis of rotation for particular values of the tank rotation. We have shown that the bubble could break into two equal-sized bubbles or two unequal-sized bubbles as a result of a massive distortion in which the bubble experiences very large longitudinal aspect ratio before breaking.

We interpret this break-up as caused by a resonance mechanism between the driving frequency (ω) and the eigenfrequency of the bubble (ω_0). More precisely, the break-up phenomenon is caused by periodic forcing at the correct frequency through a resonance, where the eigenfrequency of the elongated bubble (ω_0) at mode $n = 2$ equals the tank frequency (ω). We have proposed two definitions for the bubble's eigenfrequency. One is based on the characteristic size of the undeformed bubble (ω_{0R}), and the other, ω_0 is based on the length of the stretched bubble (L). It is shown that independent of size and rotation speed the value of ω/ω_{0R} has been found to be between 0.66 to 0.83 for ω_{0R} and in a range between 1.7 and 2.1 for ω/ω_0 for all break-up events, which is a strong argument in favor of this resonance mechanism being responsible for the rupture.

We modeled the forces acting on the bubble near the axis of rotation in our

flow situation in Chapter 4. Then we calculated the drag and lift coefficients and compared them to previous research works focused on bubbles in a condition of $Ro \geq 6$ in Rastello et al. 2009, Rastello et al. 2017 and Bluemink et al. 2008.

We have shown in section 4.2 values for the drag coefficient of the bubble, deduced from measurements of the bubble position: these results show that, as Ro becomes smaller than 1, the drag coefficient increases and the impact of Ro becomes more pronounced. We have shown that for bubbles straddling the axis of the cell, the drag coefficient could be simply approximated by $C_D \sim 1.5/Ro$. If we further consider that, for the large bubbles considered here $r_e \sim g/\omega^2$, this is equivalent to predicting $C_D \sim 1.5D\omega^2/g$ for such bubbles in this regime, a simple expression which captures well the order of magnitude of C_D for almost all our experimental conditions.

Finally, we have proposed in section 4.3 an estimate of the lift coefficient for the low Ro limit. This lift coefficient seems to be controlled by the shear Reynolds number when $Re_{shear} = Re/Ro$ is in the range [500–3000], conditions for which one may expect an inertial wake to surround the bubble. In this range, C_L is of the order of 0.5, and decreases slightly when the Rossby number is reduced (i.e. Re_{shear} is increased). We observe a transition above $Re_{shear} = 3000$, above which the bubble exhibits strong oscillations in shape and position. This transition probably occurs when the bubble approaches the conditions of its resonance.

The impact of adding surfactant within the tank on bubble dynamics was the focus of Chapter 5. To change the surface tension of the bulk liquid, we used the chemical compound *TetradecylTrimethylAmmoniumBromide* (*TTAB*). The critical micelle concentration (CMC) of *TTAB* is 1.5gr/L . As a result, we investigated two *TTAB* solutions, one lower than CMC (0.33 CMC) introduced as C' , in which the interface is not completely saturated, and the other higher than CMC (2 CMC) introduced as C'' , in which the bubble interface is expected to be completely saturated with surfactants. Afterwards, we have compared the behavior of the bubble in these *TTAB* solutions with demineralised water (previously discussed in chapters 3 and 4).

Two different tensiometers were used to measure the surface tension of both solutions. We used the first, *Attension Theta Flex*, *Biolin Scientific AB*, and the second, *Tracker Standard drop tensiometer*, to improve the accuracy of our measurements. The surface tension of 0.33 CMC converges to $\sigma_{0.33CMC} = 52 \pm 1.0$ mN/m, while that of 2 CMC converges to $\sigma_{2CMC} = 37 \pm 1.0$ mN/m, according to the findings.

In the same range of volume sizes, we found that the longitudinal aspect ratio of the bubble in both solutions is higher (the bubble stretched more along the axis of rotation) than in the demineralised water case. Furthermore, we found that our experimental data fits well with Rosenthal 1962 prediction for the case of 2 CMC in terms of aspect ratio X (fully saturated interface). However, the experimental data are shifted above the Rosenthal 1962 prediction at 0.33 CMC (not entirely saturated interface) and in this case the experimental aspect ratio is underestimated by the model. In general, we have found that bubbles in presence of surfactant behave similarly to bubbles in demineralised water. The shape of the bubble interface is nonetheless slightly different when surfactant is present, and bubbles appear more streamlined in this case. In addition, the bubbles get slightly closer to the rotation axis as a result of this interface shape (lower Rossby numbers).

Finally, we saw in this chapter that the bubble breaks at a smaller volume size in surfactant solutions, but the ratio ω/ω_0 is still in the same range as for break-up in demineralised water. This is a further argument in favor of a resonance mechanism. Moreover, we reversely changed the rotation speeds of the tank (from 900 rpm to 600 rpm) and managed to break-up the bubble by *decreasing* the rotation frequency. The values of ω/ω_0 at break-up are in the same range as for the previous series (where ω was increased). This is another strong argument in favor of a resonance mechanism.

6.2 Perspectives

Until now, we have investigated the bubble dynamics close to the axis of rotation in a solid body rotating flow without, and with one type of soluble surfactant (*TTAB*). However, further experiments are needed to broaden the results about bubble behavior in this type of flow. Our findings suggest that we still have a long way to go in fully grasping all the aspects of the bubble dynamics in a rotating flow. In the following we have listed the future studies that can be aligned with the present work.

6.2.1 Investigating the behavior of bubbles over a wider range of rotation speeds

According to chapter 2, the maximum rotation speed of the tank provided by the motor is 900 rpm (94 rad s^{-1}). We showed in Chapter 3 how the bubble goes closer to the axis of rotation and becomes more stable as the rotational velocity of the tank increases. The interesting point for the future research work is to improve the capability of the motor to effectively increase the range of rotation speeds up to 1500 rpm (157 rad s^{-1}) in order to investigate deformation, drag and lift coefficient, instability, and break-up in another range of ω . For instance, doing experiments in a range of $[800-1500] \text{ rpm}$. Furthermore, examining the instability of the bubble and the surrounding flow that leads to break-up at a lower range of rotational velocity of the tank is a fascinating project. Figure 2.31, for example, demonstrates that in a lower range of rotation speeds, the amplitude of the bubble oscillation is tremendous, the velocity is perturbed and the unknown wakes behind the bubbles appeared which lead to encounter the unknown surrounding flow. Investigating this complex flow around the bubble will expand the results of the bubble dynamics and break-up in a solid body rotating flow.

6.2.2 Using another type of surfactant

The use of *TTAB* surfactants to modify the surface tension of the carrier flow has been discussed. Future research should focus on the effects of the other chemical compounds as surfactants with another molecular structure, and compare the behavior of the bubble in their solutions. To summarize, adopting different types of surfactants (with different adsorption and desorption characteristic times in comparison with *TTAB*), and comparing them to our current findings would broaden our understanding of bubble dynamics and break-up.

6.2.3 Numerical simulation

As we saw in Chapter 5, the shape of the bubble with surfactant slightly differs from demineralized water without surfactant. It might be worthwhile to explore surfactant dispersion along the contact, particularly in the situation of a partially saturated interface. A promising future project is to explore surfactant distribution on the interface in this type of flow using the code developed by the

late Peter Spelt a level set code where surfactant inhomogeneities can be taken into account Titta 2017.

6.2.4 Investigating the bubble dynamics in presence of other surrounding bubbles

All of the studies were carried out using a single bubble in the tank. Another perspective of this experimental work would be to conduct experiments in which multiple bubbles are positioned close to the axis of rotation and the deformation, break-up and forces of each bubble will be investigated in the presence of numerous other bubbles.

In addition, how will the balance between break-up and coalescence depend on the rotation rate? And how will it be impacted by surfactants? The results obtained in this manuscript for a single bubble should help clarify this situation, which is common in applications related to mixing in rotating flows.

Bibliography

- Auton, T.R. (1987). **The lift force on a spherical body in a rotational flow.** *Journal of fluid Mechanics* 183, 199–218 (see page 3).
- Bentley, B.J. and L.G. Leal (1986). **An experimental investigation of drop deformation and breakup in steady, two-dimensional linear flows.** *Journal of Fluid Mechanics* 167, 241–283 (see page 2).
- Bluemink, J. J, D. Lohse, A. Prosperetti, and L. Van Wijngaarden (2008). **A sphere in a uniformly rotating or shearing flow.** *Journal of fluid mechanics* 600, 201–233 (see pages 6, 7, 85, 123).
- Bluemink, J. J, D. Lohse, A. Prosperetti, and L. Van Wijngaarden (2010). **Drag and lift forces on particles in a rotating flow.** *Journal of fluid mechanics* 643, 1–31 (see pages 6, 7, 80, 82).
- Bush, J., H. Stone, and J. Bloxham (1995). **Axial drop motion in rotating fluids.** *Journal of Fluid Mechanics* 282, 247–278 (see page 2).
- Cabut, D., M. Michard, S. Simoens, L. Méès, V. Todoroff, C. Hermange, and Le Chenadec, Y. (2021). **Analysis of the water flow inside tire grooves of a rolling car using refraction particle image velocimetry.** *Physics of Fluids* 33:3, 032101 (see page 6).
- Chen, Li., S.V. Garimella, J.A. Reizes, and E. Leonardi (1999). **The development of a bubble rising in a viscous liquid.** *Journal of Fluid Mechanics* 387, 61–96 (see page 1).
- Choi, J. K. and G. L. Chahine (n.d.). **Characteristics of bubble splitting in a tip vortex flow.** In: *Fifth International Symposium on Cavitation (CAV2003)* (see page 6).
- Clift, R., J.R. Grace, and M.E. Weber (1978). **Bubbles, drops, and particles** (see pages 1, 3, 4).
- Duineveld, P.C. (1995). **The rise velocity and shape of bubbles in pure water at high Reynolds number.** *Journal of Fluid Mechanics* 292, 325–332 (see page 10).
- Ervin, E.A. and G. Tryggvason (1997). **The rise of bubbles in a vertical shear flow** (see page 3).
- Fukuta, M., S. Takagi, and Y. Matsumoto (2008). **Numerical study on the shear-induced lift force acting on a spherical bubble in aqueous surfactant solutions.** *Physics of Fluids* 20:4, 040704 (see page 5).
- Green, S. (2012). **Fluid vortices.** Vol. 30. Springer Science & Business Media (see pages 5, 6).
- Hayashi, K., D. Legendre, and A. Tomiyama (2020). **Lift coefficients of clean ellipsoidal bubbles in linear shear flows.** *International Journal of Multiphase Flow* 129, 103350 (see pages 6, 81).

- Jha, N. K. and R. N. Govardhan (2015). **Interaction of a vortex ring with a single bubble: bubble and vorticity dynamics**. *Journal of Fluid Mechanics* 773, 460–497 (see page 5).
- Johnson, T. A. and V. C. Patel (1999). **Flow past a sphere up to a Reynolds number of 300**. *Journal of Fluid Mechanics* 378, 19–70 (see page 7).
- Kariyasaki, A. (1987). **Behavior of a single gas bubble in a liquid flow with a linear velocity profile**. In: *Proceedings of the 1987 ASME-JSME Thermal Engineering Joint Conference, ASME New York* (see pages 3, 81).
- Lamb, H. (1993). **Hydrodynamics**. Cambridge university press (see pages 73, 74).
- Legendre, D. and J. Magnaudet (1998). **The lift force on a spherical bubble in a viscous linear shear flow**. *Journal of Fluid Mechanics* 368, 81–126 (see pages 2, 6).
- Leslie, F. (1985). **Measurements of rotating bubble shapes in a low-gravity environment**. *Journal of fluid Mechanics* 161, 269–279 (see page 3).
- Magnaudet, J. and I. Eames (2000). **The motion of high-Reynolds-number bubbles in inhomogeneous flows**. *Annual Review of Fluid Mechanics* 32:1, 659–708. DOI: 10.1146/annurev.fluid.32.1.659 (see pages 64, 81).
- Maneshian, B., K. Javadi, and M. T. Rahni (2018). **Bubble dynamics in rotating flow under an accelerating field**. *Physics of Fluids* 30:8, 082108 (see page 3).
- Marten, K., K. Shariff, S. Psarakos, and D. J. White (1996). **Ring bubbles of dolphins**. *Scientific American* 275:2, 82–87 (see page 6).
- Naciri, A. (1992). **Contribution à l'étude des forces exercées par un liquide sur une bulle de gaz: portance, masse ajoutée et interactions hydrodynamiques**. PhD thesis. Ecully, Ecole centrale de Lyon (see page 6).
- Perrard, S., A. Rivière, W. Mostert, and L. Deike (2021). **Bubble deformation by a turbulent flow**. *Journal of Fluid Mechanics* 920 (see page 2).
- Pesci, C., A. Weiner, H. Marschall, and D. Bothe (2018). **Computational analysis of single rising bubbles influenced by soluble surfactant**. *Journal of Fluid Mechanics* 856, 709–763 (see page 5).
- Rastello, M. and J.L. Marié (2020). **Wake behind contaminated bubbles in a solid-body rotating flow**. *J. Fluid Mech.* 884 (see pages 7, 85).
- Rastello, M., J.L. Marié, N. Grosjean, and M. Lance (2009). **Drag and lift forces on interface-contaminated bubbles spinning in a rotating flow**. *Journal of fluid mechanics* 624, 159–178 (see pages 6, 7, 10, 12, 63, 64, 67, 68, 83, 85, 123).
- Rastello, M., J.L. Marié, and M. Lance (2011). **Drag and lift forces on clean spherical and ellipsoidal bubbles in a solid-body rotating flow**. *J. Fluid Mech.* 682, 434–459 (see page 7).
- Rastello, M., J.L. Marié, and M. Lance (2017). **Clean versus contaminated bubbles in a solid-body rotating flow**. *J. Fluid Mech.* 831, 529–617 (see pages 7, 8, 68, 80–82, 85, 123).

- Risso, F. (2000). **The mechanisms of deformation and breakup of drops and bubbles**. *Multiphase Science and technology* 12:1. DOI: 10.1615/MultScienTechn.v12.i1.10 (see pages 3, 56, 81).
- Rodgar, M., H. Scolan, J.-L. Marié, D. Doppler, and J.-P. Matas (2021). **Bubble behaviour in a horizontal high-speed solid-body rotating flow**. *Journal of Fluid Mechanics* 925 (see page 131).
- Rosenthal, D. K. (1962). **The shape and stability of a bubble at the axis of a rotating liquid**. *Journal of Fluid Mechanics* 12:3, 358–366. DOI: 10.1017/S0022112062000269 (see pages v–viii, 7, 8, 39, 45–47, 49, 51, 53, 55, 56, 60, 72, 96, 97, 99, 122, 124).
- Saffman, P.G.T. (1965). **The lift on a small sphere in a slow shear flow**. *Journal of fluid mechanics* 22:2, 385–400 (see page 3).
- Sauma-Pérez, T., C.G. Johnson, Y. Yang, and T. Mullin (2018). **An experimental study of the motion of a light sphere in a rotating viscous fluid**. *J. Fluid Mech.* 847, 119–133 (see page 36).
- Schiller, L. and A. Naumann (1933). **Drag coefficient for spherical shape**. *VDI Zeits.* 13, 318 (see page 67).
- Serizawa, A., I. Kataoka, and I. Michiyoshi (1975). **Turbulence structure of air-water bubbly flow—II. Local properties**. *International Journal of Multiphase Flow* 2:3, 235–246 (see page 2).
- Sridhar, G. and J. Katz (1995). **Drag and lift forces on microscopic bubbles entrained by a vortex**. *Physics of Fluids* 7:2, 389–399 (see page 5).
- Tagawa, Y., T. Ogasawara, S. Takagi, and Y. Matsumoto (2010). **Surfactant effects on single bubble motion and bubbly flow structure**. In: *AIP Conference Proceedings*. Vol. 1207. 1. American Institute of Physics, 43–48 (see page 4).
- Takagi, S. and Y. Matsumoto (2011). **Surfactant effects on bubble motion and bubbly flows**. *Annual Review of Fluid Mechanics* 43, 615–636 (see pages 3, 4).
- Takagi, S., T. Ogasawara, and Y. Matsumoto (2008). **The effects of surfactant on the multiscale structure of bubbly flows**. *Philosophical Transactions of the Royal Society A: Mathematical, Physical and Engineering Sciences* 366:1873, 2117–2129 (see page 4).
- Takemura, F., S. Takagi, J. Magnaudet, and Y. Matsumoto (2002). **Drag and lift forces on a bubble rising near a vertical wall in a viscous liquid**. *Journal of Fluid Mechanics* 461, 277–300 (see pages 2, 6).
- Titta, A. (2017). **Simulations level-set d'un amas de bulles cisailées: écoulement et dynamique des tensioactifs**. PhD thesis. Université Claude Bernard Lyon 1 (see page 126).
- Tomiya, A., H. Tamai, I. Zun, and S. Hosokawa (2002). **Transverse migration of single bubbles in simple shear flows**. *Chemical Engineering Science* 57:11, 1849–1858 (see page 6).

- Van Nierop, E. A., S. Luther, J. J. Bluemink, J. Magnaudet, A. Prosperetti, and D. Lohse (2007). **Drag and lift forces on bubbles in a rotating flow**. *Journal of Fluid Mechanics* 571, 439–454 (see pages 6, 63, 67).
- Wang, X., B. Klaasen, J. Degrève, A. Mahulkar, G. Heynderickx, M.-F. Reyniers, B. Blanpain, and F. Verhaeghe (2016). **Volume-of-fluid simulations of bubble dynamics in a vertical Hele-Shaw cell**. *Physics of Fluids* 28:5, 053304. DOI: [10.1063/1.4948931](https://doi.org/10.1063/1.4948931) (see page 1).

Publications

1. Rodgar et al. [2021](#), **J. Fluid Mechanics**, Cambridge University Press